



# UNIVERSITÀ DEGLI STUDI DI PADOVA

*Dipartimento di Ingegneria Industriale - DII*

SCUOLA DI DOTTORATO DI RICERCA IN INGEGNERIA INDUSTRIALE

CURRICULUM: INGEGNERIA MECCANICA

CICLO XXXII

## MODELLING THE INFLUENCE OF PHASE TRANSFORMATION KINETICS IN 22MNB5 HOT STAMPING

**Direttore della Scuola:** Ch.mo Prof. Paolo Colombo

**Coordinatore d'indirizzo:** Ch.mo Prof. Giovanni Meneghetti

**Supervisore:** Ch.mo Prof. Andrea Ghiotti

**Dottorando:** Giulia Venturato



*A goal is just a dream  
that rolled up its sleeves  
and got to work*



## **ACKNOWLEDGMENTS**

First, I would like to thank Prof. Andrea Ghiotti and Prof. Stefania Bruschi who gave me the possibility to perform my Ph.D. and for their valuable advice, suggestions and teaching.

A warm thanks to my colleagues for their precious support and friendship during these years and to my students who always gave me interesting challenges to solve.

My gratitude goes to my family, for their wonderful support over the years. This goal could not have been reached without them.

Last, but not absolutely least, a special thanks to my beloved husband, who always has a sweet word to encourage me and do my best and believes in me more than I do myself.



# TABLE OF CONTENTS

<b>TABLE OF CONTENTS</b>	<b>I</b>
<b>LIST OF FIGURES</b>	<b>V</b>
<b>LIST OF TABLES</b>	<b>XI</b>
<b>ABSTRACT</b>	<b>XIII</b>
<b>SOMMARIO</b>	<b>XV</b>
<b>CHAPTER 1: Introduction</b>	<b>1</b>
<b>1.1 Industrial and scientific problem</b>	<b>3</b>
<b>1.2 Objectives and work organisation</b>	<b>6</b>
<b>CHAPTER 2: Literature review</b>	<b>7</b>
<b>2.1 Hot stamping process: description and technology</b>	<b>8</b>
<b>2.2 Materials and coatings</b>	<b>10</b>
<b>2.3 Phase transformation kinetic</b>	<b>12</b>
<b>2.4 Thermo-mechanical properties</b>	<b>14</b>
<b>2.5 Formability</b>	<b>16</b>
<b>2.6 Numerical Simulations</b>	<b>19</b>
<b>2.7 Damage modelling</b>	<b>21</b>
<b>2.8 Aim of the work</b>	<b>22</b>
<b>CHAPTER 3: Experimental equipment and procedures</b>	<b>25</b>
<b>3.1 Material 22MnB5</b>	<b>27</b>
<b>3.2 Study of the phase transformation kinetic</b>	<b>28</b>

<b>3.3</b>	<b>Equipment and procedures for tensile tests</b>	<b>32</b>
	<u>3.3.1 Preliminary studies on Austenite phase</u>	33
	<u>3.3.2 Ferrite + Pearlite mixture and Austenite phases' rheology</u>	35
	<u>3.3.3 Bainite and Martensite phases' rheology</u>	35
<b>3.4</b>	<b>Equipment and procedures for Nakajima tests</b>	<b>38</b>
	<u>3.4.1 Influence of the temperature on the formability</u>	41
	<u>3.4.2 Influence of the microstructure on the formability</u>	42
<b>3.5</b>	<b>GISSMO damage criterion</b>	<b>44</b>
<b>CHAPTER 4: Numerical modelling</b>		<b>47</b>
<b>4.1</b>	<b>Material model</b>	<b>49</b>
<b>4.2</b>	<b>CCT left-shift simulations</b>	<b>55</b>
<b>4.3</b>	<b>Nakajima tests simulations</b>	<b>57</b>
<b>4.4</b>	<b>GISSMO damage criterion simulations</b>	<b>59</b>
<b>4.5</b>	<b>Explicit simulations settings</b>	<b>61</b>
<b>CHAPTER 5: Results and discussion</b>		<b>63</b>
<b>5.1</b>	<b>Phase transformation kinetics</b>	<b>65</b>
<b>5.2</b>	<b>Study of 22MnB5 rheology</b>	<b>69</b>
	<u>5.2.1 Preliminary studies on the Austenite phase</u>	69
	<u>5.2.2 Rheology of the Ferrite + Pearlite mixture of phases</u>	74
	<u>5.2.3 Rheology of the Austenite phase</u>	76
	<u>5.2.4 Rheology of the Bainite phase</u>	78
	<u>5.2.5 Rheology of the Martensite phase</u>	81

<u>5.2.6 Analysis of the temperature</u>	83
<b>5.3 Modified Johnson-Cook fitting model</b>	<b>84</b>
<u>5.3.1 Calibration of the model</u>	84
<u>5.3.2 Ferrite + Pearlite curves fitting</u>	88
<u>5.3.3 Austenite curves fitting</u>	90
<u>5.3.4 Bainite curves fitting</u>	92
<u>5.3.5 Martensite curves fitting</u>	95
<b>5.4 Study of the formability of 22MnB5</b>	<b>96</b>
<u>5.4.1 Influence of the temperature</u>	96
<u>5.4.2 Influence of the microstructure</u>	97
<b>5.5 Numerical simulations results</b>	<b>98</b>
<u>5.5.1 CCT left-shift simulations</u>	98
<u>5.5.2 Hot Nakajima tests simulations</u>	99
<b>5.6 GISSMO damage criterion</b>	<b>103</b>
<u>5.6.1 Determination of the stress triaxiality</u>	103
<u>5.6.2 Damage model calibration</u>	105
<u>5.6.3 Damage model validation</u>	109
<b>CHAPTER 6: Conclusions</b>	<b>111</b>
<b>REFERENCES</b>	



# LIST OF FIGURES

<u>Figure 1.1</u> : CO <sub>2</sub> emission target fixed with Kyoto protocol	3
<u>Figure 1.2</u> : Hot-stamped steel door ring structure and front header, which comprise about a third of the upper body	4
<u>Figure 2.1</u> : Hot stamped parts in a typical middle class	9
<u>Figure 2.2</u> : Basic hot stamping process chains: (a) direct hot stamping, (b) indirect hot stamping	10
<u>Figure 2.3</u> : CCT diagram of Usibor 1500P® according to ArcelorMittal™	13
<u>Figure 2.4</u> : a) Experimental apparatus used by Merklein et al., b) example of temperature dependency of the flow curves	15
<u>Figure 2.5</u> : a) Nakajima test setup, b) Marciniak test setup according to ISO standard	17
<u>Figure 2.6</u> : Fully coupled thermo-mechanical-metallurgical model scheme	19
<u>Figure 2.7</u> : a) Necking prediction, b) Thickness comparison	20
<u>Figure 2.8</u> : Flow chart of the activities performed for the thesis work	24
<u>Figure 3.1</u> : Microstructure of 22MnB5 in a) cross-section b) as-delivered condition c) after thermal treatment	28
<u>Figure 3.2</u> : Gleeble 3800® equipped for the phase transformation kinetic tests	29
<u>Figure 3.3</u> : Specimen used for the phase transformation kinetic tests	29
<u>Figure 3.4</u> : thermal cycle applied for the a) CCT diagram drawing and b) CCT curves left-shift	31
<u>Figure 3.5</u> : Thermal cycle applied for the study of the phase transformation kinetics at constant temperature	31
<u>Figure 3.6</u> : MTS 322 equipped for the hot tensile tests	32
<u>Figure 3.7</u> : Aramis™ elaboration and resultant strain plot	33

<u>Figure 3.8</u> : Specimen used for the hot tensile tests	33
<u>Figure 3.9</u> : Thermal cycle applied for the study of a) the influence of $T_{test}$ and b) the influence of strain rate	34
<u>Figure 3.10</u> : Thermal cycle applied for the hot tensile test of a) ferrite + pearlite mixture and b) austenite phase	35
<u>Figure 3.11</u> : Microstructure distribution on the tensile specimen due to the Joule effect	36
<u>Figure 3.12</u> : a) Equipment for the thermal treatment of the steel stripes and final dog-bone specimens; b) thermal cycle applied for the study of the bainite, and c) the martensite phase	37
<u>Figure 3.13</u> : a) Curve of the transformation of austenite into bainite; b), thermal cycle registered by the pyrometers and c) Rockwell hardness C of the heat-treated stripes	38
<u>Figure 3.14</u> : a) Specimens used for the hot Nakajima tests, b) Nakajima testing equipment, c) inductor heads used to heat the specimen during the test	40
<u>Figure 3.15</u> : Aramis <sup>TM</sup> elaboration and resultant strain plot	41
<u>Figure 3.16</u> : a) Thermal cycle applied, b) thermo-camera data	42
<u>Figure 3.17</u> : Thermal cycles applied for the a) 100% austenite tests, b) 50% austenite- 50% bainite tests, c) 100% bainite tests, d) saturation curve at 600°C	44
<u>Figure 3.18</u> : a) Specimens used for GISSMO calibration, b) thermal cycle	45
<u>Figure 4.1</u> : MAT_244_UHS_STEEL card in LS_DYNA code	55
<u>Figure 4.2</u> : Implemented temperature profile compared with the experimental data	56
<u>Figure 4.3</u> : Implemented specimens' geometries and temperature profiles comparison	57
<u>Figure 4.4</u> : Nakajima simulation tools and geometries setting	58
<u>Figure 4.5</u> : MAT_ADD_EROSION card	60

<u>Figure 4.6</u> : Flow chart of the LS_OPT calculations	60
<u>Figure 5.1</u> : a) Experimental CCT diagram of 22MnB5 steel, b) dilatometric curve to detect the CCT points	65
<u>Figure 5.2</u> : CCT left-shift, 5% pre-strain applied at 800°C and 700°C, with strain rate 0.1 s <sup>-1</sup> .	67
<u>Figure 5.3</u> : CCT left-shift, 5% pre-strain applied at 800°C and 700°C, with strain rate 1 s <sup>-1</sup>	67
<u>Figure 5.4</u> : CCT left-shift, 10% pre-strain applied at 800°C and 700°C, with strain rate 0.1 s <sup>-1</sup>	68
<u>Figure 5.5</u> : CCT left-shift, 10% pre-strain applied at 800°C and 700°C, with strain rate 1 s <sup>-1</sup>	68
<u>Figure 5.6</u> : CCT left-shift, 15% pre-strain applied at 800°C and 700°C, with strain rate 0.1 s <sup>-1</sup>	69
<u>Figure 5.7</u> : CCT left-shift, 20% pre-strain applied at 800°C, with strain rate 0.1 s <sup>-1</sup>	69
<u>Figure 5.8</u> : Flow curves sensitivity to the temperature at constant strain rate	70
<u>Figure 5.9</u> : Flow curves sensitivity to the strain rate at constant testing temperature	71
<u>Figure 5.10</u> : Times of the experimental tests compared with CCT curve	72
<u>Figure 5.11</u> : Saturation curve of the transformation austenite – bainite at a) 500°C, b) 550°C and c) 600°C	73
<u>Figure 5.12</u> : Optical microscope pictures of the specimens tested a) at constant T <sub>test</sub> = 550°C, b) at constant strain rate = 0.01 s <sup>-1</sup>	74
<u>Figure 5.13</u> : Ferrite + pearlite mixture tensile tests results for 0.1 s <sup>-1</sup> .	75
<u>Figure 5.14</u> : Ferrite + pearlite mixture tensile tests results for 1 s <sup>-1</sup>	75
<u>Figure 5.15</u> : Ferrite + pearlite mixture tensile tests results for 10 s <sup>-1</sup>	76
<u>Figure 5.16</u> : Austenite phase tensile tests results for 0.1 s <sup>-1</sup>	77

<u>Figure 5.17</u> : Austenite phase tensile tests results for $0.1 \text{ s}^{-1}$	77
<u>Figure 5.18</u> : Austenite phase tensile tests results for $10 \text{ s}^{-1}$	78
<u>Figure 5.19</u> : Temperature and strain rate sensitivity of bainite phase	79
<u>Figure 5.20</u> : Bainite phase tensile tests results for low temperatures, $1 \text{ s}^{-1}$	80
<u>Figure 5.21</u> : Bainite phase tensile tests results for $400^\circ\text{C}$	80
<u>Figure 5.22</u> : Bainite phase tensile tests results for $500^\circ\text{C}$	81
<u>Figure 5.23</u> : Bainite phase tensile tests results for $600^\circ\text{C}$	81
<u>Figure 5.24</u> : Temperature and strain rate sensitivity of the martensite phase	82
<u>Figure 5.25</u> : Martensite phase tensile tests results	83
<u>Figure 5.26</u> : Temperature variation for the different testing temperatures involved in the paper, a) $800\text{-}700^\circ\text{C}$ , b) $600\text{-}500^\circ\text{C}$ , c) $400\text{-}300^\circ\text{C}$ , d) $200\text{-}100^\circ\text{C}$	84
<u>Figure 5.27</u> : Experimental results for pure austenite phase tested at $850^\circ\text{C}$ , at $0.1 \text{ s}^{-1}$ , $1 \text{ s}^{-1}$ and $10 \text{ s}^{-1}$ fit with original Johnson-Cook model, a) flow curves, b) $\Delta\sigma$	86
<u>Figure 5.28</u> : Delta between experimental and calculated stress a) first term modified, b) second term modified, c) third term modified.	87
<u>Figure 5.29</u> : a) Delta between experimental and calculated stress, fourth term added, b) flow curves pure of austenite phase tested at $850^\circ\text{C}$ , at $0.1 \text{ s}^{-1}$ , $1 \text{ s}^{-1}$ and $10 \text{ s}^{-1}$ fit with modified Johnson-Cook model	88
<u>Figure 5.30</u> : Fitted flow curves of the mixture ferrite+ pearlite tested at $0.1 \text{ s}^{-1}$	89
<u>Figure 5.31</u> : Fitted flow curves of the mixture ferrite+ pearlite tested at $1 \text{ s}^{-1}$	89
<u>Figure 5.32</u> : Fitted flow curves of the mixture ferrite+ pearlite tested at $10 \text{ s}^{-1}$	90
<u>Figure 5.33</u> : Fitted flow curves of the austenite phase tested at $0.1 \text{ s}^{-1}$	91

<u>Figure 5.34</u> : Fitted flow curves of the austenite phase tested at $1 \text{ s}^{-1}$	91
<u>Figure 5.35</u> : Fitted flow curves of the austenite phase tested at $10 \text{ s}^{-1}$	92
<u>Figure 5.36</u> : Tensile tests results for the pure bainite phase: low temperatures, $1 \text{ s}^{-1}$	93
<u>Figure 5.37</u> : Tensile tests results for the pure bainite phase: $400^\circ\text{C}$	93
<u>Figure 5.38</u> : Tensile tests results for the pure bainite phase: $500^\circ\text{C}$	94
<u>Figure 5.39</u> : Tensile tests results for the pure bainite phase: $600^\circ\text{C}$	94
<u>Figure 5.40</u> : Tensile tests results for the pure martensite phase tested at $1 \text{ s}^{-1}$	95
<u>Figure 5.41</u> : FLCs at a) $600^\circ\text{C}$ and b) $500^\circ\text{C}$	96
<u>Figure 5.42</u> : Comparison between FLCs at $600^\circ\text{C}$ and $500^\circ\text{C}$	97
<u>Figure 5.43</u> : FLCs obtained at $600^\circ\text{C}$ for different microstructure	97
<u>Figure 5.44</u> : Comparison between experimental and numerical results CCT left-shift, 20% pre-strain applied at $800^\circ\text{C}$ , with a strain rate of $0.1 \text{ s}^{-1}$	99
<u>Figure 5.45</u> : FLCs obtained at $600^\circ\text{C}$ for different microstructure compared with the numerical simulations results	100
<u>Figure 5.46</u> : Experimental and numerical thickness reduction: a) 100% A; b) 50%A-50%B, c) 100% B	101
<u>Figure 5.47</u> : Experimental and numerical normalized major strain, 100% bainite case	102
<u>Figure 5.48</u> : Comparison between simulations with MAT_244 and MAT_106	103
<u>Figure 5.49</u> : Stress triaxiality results from the numerical simulations	104
<u>Figure 5.50</u> : Curves fracture and instability strain vs triaxiality for the tests performed at (a) $700^\circ\text{C}$ , (b) $800^\circ\text{C}$	105

<u>Figure 5.51</u> : Comparison between effective strain of real specimens and simulation; temperature = 700°C, a) smooth, b) notch 2 mm, c) notch 5 mm, d) notch 10 mm, e) shear, f) Nakajima 200mm	106
<u>Figure 5.52</u> : Comparison between effective strain of real specimens and simulation; temperature = 800°C, a) smooth, b) notch 2 mm, c) notch 5 mm, d) notch 10 mm, e) shear, f) Nakajima 200mm	107
<u>Figure 5.53</u> : Comparison between experimental and calculated flow curve, T=700°C	108
<u>Figure 5.54</u> : Comparison between experimental and calculated flow curve, T=800°C	109
<u>Figure 5.55</u> : Comparison between major strain of real Nakajima 100 mm specimen and simulation; a) temperature = 700°C, b) temperature = 800°C	110

## LIST OF TABLES

<u>Table 3.1</u> : Nominal composition of 22MnB5 [C]	27
<u>Table 3.2</u> : Experimental plan for the phase transformation kinetics study	30
<u>Table 3.3</u> : Experimental plan for the preliminary studies	34
<u>Table 3.4</u> : Experimental plan for the hot tensile tests of Ferrite+Pearlite and austenite	35
<u>Table 3.5</u> : Experimental plan for the hot tensile tests of bainite and martensite	37
<u>Table 3.6</u> : Experimental plan for the hot Nakajima tests- influence of temperature	42
<u>Table 3.7</u> : Experimental plan for the hot tensile tests for the calibration of GISSMO	45
<u>Table 4.1</u> : Nominal composition of 22MnB5 by Akerstrom	53
<u>Table 5.1</u> : new experimental plan for the study of the CCT left-shift	66
<u>Table 5.2</u> : data of strain, time and estimated % of bainite	72
<u>Table 5.3</u> : New experimental plan for the bainite phase	79
<u>Table 5.4</u> : New experimental plan for the martensite phase	82
<u>Table 5.5</u> : Temperature variations during the hot tensile test	83
<u>Table 5.6</u> : Parameters of the Johnson-Cook original model	85
<u>Table 5.7</u> : Average percentage errors between the $\sigma_{exp}$ and $\sigma_{JC}$	85
<u>Table 5.8</u> : Average percentage errors between the $\sigma_{exp}$ and $\sigma_{JCM}$	88
<u>Table 5.9</u> : Parameters of the modified Johnson-Cook model used to fit the ferrite + pearlite flow curves	90
<u>Table 5.10</u> : Parameters of the modified Johnson-Cook model used to fit the austenite flow curves	92

<u>Table 5.11</u> : Parameters of the modified Johnson-Cook model used to fit the austenite flow curves	94
<u>Table 5.12</u> : Parameters of the modified Johnson-Cook model used to fit the austenite flow curves	95
<u>Table 5.13</u> : LCEPSi values implemented in the numerical simulations.	99
<u>Table 5.14</u> : Flags AUST and BAIN settings	100
<u>Table 5.15</u> : Mean values of stress triaxiality	104
<u>Table 5.16</u> : Experimental fracture and instability strain values, tests at 700°C	105
<u>Table 5.17</u> : Experimental fracture and instability strain values, tests at 800°C	105
<u>Table 5.18</u> : Comparison between experimental and calculated strain at fracture T = 700°C	107
<u>Table 5.19</u> : Comparison between experimental and calculated strain at fracture T = 800°C	108
<u>Table 5.20</u> : Comparison between experimental and calculated major strain at fracture, Nakajima 100 mm	109



## ABSTRACT

Sheet metal forming has gained, over the last years, more and more importance since the automotive industry is demanding very specific characteristic for the new generation of components of the car body-in-white. The requirements of more lightness for enhancing the fuel saving is becoming a key factor for the design of new components, but the lightness must be coupled with a high mechanical resistance to grant the passengers' safety. One of the most effective ways to meet these requirements has been the use of new generations of High Strength Steels (HSS), whose mechanical properties can be enhanced by thermal treatments. Direct hot stamping has represented an effective solution to do that, due to the possibility to shorten the process chain of many sheet metal parts typical of the car body-in-white. Thinner sheets have been used for the manufacturing of many automotive parts, granting the desired lightness and high resistance, to obtain the crashworthiness necessary to protect the passengers of the vehicle. Hot stamping is, nowadays, widely applied in the automotive industry, but the research in this field is still of high interest between the academic environment. This is because the process involves a large series of parameters that have to be accurately understood to enhance the performances and the complexity of the stamped parts. Since the initial heating to the last quenching step, the material undergoes a series of microstructural and mechanical transformations, whose optimization and right timing govern the final characteristic of the final component. In parallel to the industrial development work, a large branch of academic and scientific research is focused on the numerical modelling of the process which reveals of fundamental importance for the process design and optimization.

The present work stands in the framework of the researches in the field of the hot stamping process. The material investigated in this work is the AluSi® pre-coated quenchable steel 22MnB5, well known with the commercial name of Usibor 1500P®. The complete characterization of this material aims to fill the lack in literature about testing in hot condition the material flow stress of all the microstructural phases, proposing a fitting model capable to describe the mechanical behaviour in the FE models. The formability in hot conditions is studied as well, analysing the effect of the temperature and microstructure on the resultant Forming Limit Curve (FLC). The phase transformation kinetics was studied, confirming the literature and giving the motivation for this work. Finally,

the damage criterion Generalized Incremental Stress-State dependent damage MOdel (GISSMO) was calibrated. The whole experimental activity was coupled with numerical simulations, for the necessary data analysis and calibration.

The work presented in this thesis has been carried out at the DII laboratories of the University of Padova, from October 2016 to September 2019 under the supervision of Prof. Andrea Ghiotti. This work was carried out within the framework of the University Research Project “Advanced CAE method to predict failure and material properties in hot forming” ref. 2014-4050 URP Award developed in cooperation with Ford Motor Company GMBH.



## SOMMARIO

La deformazione di lamiere sta guadagnando, negli ultimi anni, sempre più importanza dal momento che l'industria automobilistica sta richiedendo caratteristiche molto specifiche per la nuova generazione di componenti per la scocca. Le richieste di leggerezza per aumentare il risparmio di carburante sta diventando un fattore chiave per il design di nuovi componenti, ma la leggerezza deve necessariamente essere accoppiata con l'alta resistenza meccanica per garantire la sicurezza dei passeggeri. Uno dei metodi più efficaci per incontrare tali richieste è stato l'utilizzo della nuova generazione di acciai alto resistenziali (HSS), le cui proprietà meccaniche possono essere migliorate grazie ai trattamenti termici. Lo stampaggio a caldo diretto rappresenta una soluzione efficace per questo scopo, grazie alla possibilità di accorciare la catena di processo di molti componenti metallici della scocca dell'auto. Lamiere più sottili vengono impiegate per la produzione di molte parti dell'auto, garantendo le desiderate leggerezza e alta resistenza, per ottenere la resistenza agli urti necessaria a proteggere i passeggeri del veicolo. Lo stampaggio a caldo è, oggi, ampiamente applicato nell'industria automobilistica, ma la ricerca in questo campo è ancora di alto interesse nell'ambiente accademico. Questo è dovuto al fatto che lo stampaggio a caldo coinvolge un'ampia serie di parametri che devono essere accuratamente compresi per migliorare il potenziale del processo e la complessità delle parti stampate. A partire dal primo stage di riscaldamento all'ultima fase di tempra, il materiale subisce una serie di trasformazioni microstrutturali e meccaniche, la cui ottimizzazione e il loro corretto timing controlla le caratteristiche finali del componente. Parallelamente al lavoro di ricerca sperimentale, una grande branca della ricerca è volta allo studio delle simulazioni numeriche che sono di fondamentale importanza per simulare il processo e ottimizzarne ogni step.

Il presente lavoro si inquadra nella ricerca nell'ambito dello stampaggio a caldo. Il materiale studiato in questo lavoro è l'acciaio temprabile 22MnB5 rivestito da AluSi®, conosciuto commercialmente con il nome di Usibor 1500 P®. La completa caratterizzazione del materiale ha come scopo di coprire le mancanze nella letteratura nell'ambito dei test ad alta temperatura sulla reologia di tutte le microstrutture, proponendo un modello di fitting per rappresentare i dati nei modelli FE. La formabilità ad alta temperatura è altresì soggetto di studio, analizzando gli effetti della temperatura e della microstruttura nella risultante

curva limite di formabilità (FLC). La cinetica di trasformazione di fase è stata oggetto di studio, confermando i dati presentati in letteratura e fornendo le basi per questo lavoro. Infine, il nuovo modello di danneggiamento Generalized Incremental Stress-State dependent damage MOdel (GISSMO) è stato calibrato. L'intera attività sperimentale è stata affiancata alle simulazioni numeriche, per la necessità dell'analisi e calibrazione dei dati.

Il lavoro presentato in questa tesi è stato portato avanti nei laboratori del Dipartimento di Ingegneria Industriale, DII, dell'università di Padova, da ottobre 2016 a settembre 2019 sotto la supervisione del prof. Andrea Ghiotti. Questo lavoro è parte del progetto di ricerca dell'Università chiamato "Advanced CAE method to predict failure and material properties in hot forming" ref. 2014-4050 URP Award, sviluppato in collaborazione con Ford Motor Company GMBH.

# **CHAPTER 1**

## **Introduction**



The aim of this Chapter is to present the industrial and scientific problem which lead the experimental campaign and the researches that were carried out for the completion of this work.

## 1.1 Industrial and scientific problem

The development of the vehicle in the last years, in terms of fuel efficiency along with lightness and crashworthiness, requires a new approach in the production of the car body-in-white components. Saab, in 1984, introduced the hot stamping process, which, in the last decades, is becoming more and more a key process in the automotive field. This process allows the production of car body-in-white components with increased crashworthiness but decreased weight, thanks to the thinner metal sheets that can be used. The reduction of weight is strictly connected with the reduction of fuel consumption or the efficiency of hybrid and electric engines, which is the focus of all car manufacturers in the last years. Figure 1.1 shows the fuel emission reduction established by EU and US commissions after the Kyoto protocol which came into force in 2005 [1], with challenging targets in term of the control of fuel emissions. Specifically, a target of 95 g/km by the 2020s was set.

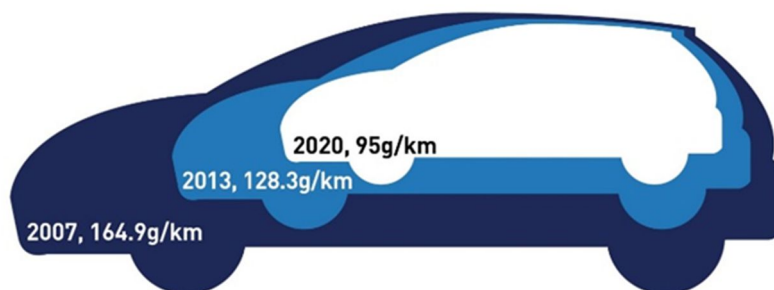
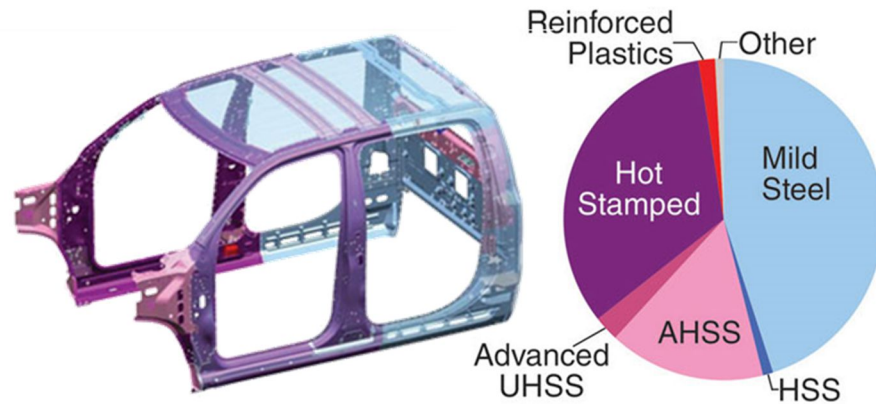


Figure 1.1: CO<sub>2</sub> emission target fixed with Kyoto protocol [2].

The development of the process has gone together with the development of the materials that are more suitable to be applied, consequently, in the last two decades, High and Ultra-High Strength Steels (HSSs and UHSSs) have gradually substituted mild steels in the car manufacturing, with a larger use for the body-in-white parts, thanks to the potential weight reduction they offer. Figure 1.2

shows the components of the car body-in-white that were produced in 2018 and it can be seen that the hot-stamped parts are a great part of the total.



*Figure 1.2: Hot-stamped steel door ring structure and front header, which comprise about a third of the upper body [3].*

The hot stamping process has its focus on the phase transformations that occur during the heating and the cooling of the blank. The first microstructural modification is the shifting of the initial ferrite + pearlite to austenite and the second is the shifting of the austenite into final martensite, bainite or a mixture of them. There is also the possibility to mask specific areas of the blank in order to prevent the initial transformation from ferrite + pearlite to austenite and, therefore, to prevent the final microstructure to become martensite and/or bainite. This allows the production of components with tailored properties, namely enhancing mechanical resistance in some areas (martensite/ bainite microstructure) and enhancing ductility in others (ferrite + pearlite microstructure). Depending on the process' cycle, the hot stamping can be defined as direct or indirect: if the forming of the blank is prior to the heating, the process is named indirect, and, if the forming of the blank follows the heating, the process is named direct. This means that the deformation in the indirect hot stamping process occurs when the material's microstructure is ferrite + pearlite, while in the direct hot stamping process the deformation occurs when the material's microstructure is austenite. In this work, the reference is represented by the direct hot stamping process.

One of the most used material for the hot stamping process is 22MnB5 (commercial name Usibor 1500P). In its delivered conditions, it has a microstructure composed by a mixture of about 60% ferrite and 40% pearlite,

and a mechanical resistance of about 600 MPa and an elongation of about 30%, but, after the microstructural evolution, it can reach mechanical resistance up to 1500 MPa, but elongation of about 5%.

The hot stamping process involves a large number of parameters that has to be carefully analysed and understood in order to correctly calibrate the process' cycle and obtain the final components with the wanted properties.

The first stage of the direct hot stamping process is represented by the heating of the blank. In this phase the first microstructural evolution occurs and it is of fundamental importance that the austenite is correctly reached: time and temperature play a fundamental role in this phase, since high austenitization temperature, i.e. 1000°C, can be coupled with low permanence time in the heating system, while low austenitization temperatures, i.e. 850°C, has to be coupled with high permanence time in the heating system. If these two parameters are not perfectly coupled, a number of problems can arise: too long times at high temperature can lead to an excessive enlargement of the grains, with a lowering of the mechanical properties (Hall-Petch law); on the other hand, too short time at low temperature can lead to partial transformation of ferrite+pearlite into austenite, and this means that after quenching, just part of the microstructure can shift into martensite/bainite, resulting in a piece with unexpected weak areas that can lead to failure.

The second stage is the transfer of the blank from the heating system to the dies. The time of the transfer is again fundamental: the thermal exchange with air is not negligible and the blank cools down before reaching the dies. The blank should reach the forming-quenching step at a temperature between 800°C and 700°C, when it is more formable and, according to the CCT diagram, the phase transformation from austenite in martensite or bainite is prevented, and the forming step is conducted in pure austenite phase. If the temperature of the blank is too low when it reaches the dies, the phase transformation of austenite into martensite or bainite is possible and can occur during the forming stage, with consequent ruptures. Moreover, it has been demonstrated that applied strain during the cooling of the blank can anticipate the phase transformation of both bainite and martensite. This means that, if the blank starts the deformation at the wrong temperature, along with the lower formability, the CCT shift anticipates the phase transformation and lowers the formability even more.

The third stage of the hot stamping process is the forming-quenching using cooled dies. As said, the CCT curves represent the phase transformation during continuous cooling, and the design of the dies and their cooling system is based on the cooling paths described on the CCT.

Every step of the process presents a number of potential critical situations that requires a deep understanding of the material behaviour, which is the key to the good calibration of the whole process. FE simulations are very important in the optimization of the hot stamping process and the precise calibration of the numerical models is a strong requirement to obtain reliable results.

## 1.2 Objectives and work organisation

The aim of the work is to study the behaviour of 22MnB5 steel, provided by ArcelorMittal™ with the name of Usibor 1500P®, with AluSi® coating. The collected data regarded different aspects of the material behaviour, the kinetics of the phase transformation, the rheology, the formability and, finally the accumulation of damage and fracture.

This work is divided into six Chapters which are here summarized:

- Chapter 1: introduction and work organization;
- Chapter 2: review of the state of art, highlighting the results of the scientific literature and their lacks;
- Chapter 3: presentation of the experimental equipment used for this work and the procedures followed during the different experimental campaigns;
- Chapter 4: description of the numerical simulations setup, highlighting the main features used, in particular, the material model and the damage model;
- Chapter 5: presentation of all the results obtained during the three-year work, discussing every aspect and highlighting the most important findings;
- Chapter 6: conclusions and possible future development of this work.

## **CHAPTER 2**

### **Literature review**



In this chapter, the analysis of the scientific literature about hot stamping is presented. First, the hot stamping is presented in detail in all its aspects, pros, cons and critical aspects that need to be highlight. Then a brief analysis of the materials used in the hot stamping process is presented. The literature review, then, moves in detail to the critical aspects of the hot stamping process: first the phase transformation kinetics, then the thermo-mechanical properties of the materials, thirdly the formability and, finally, the damage models. This chapter is concluded with the aim of the present thesis and its place among the literature regarding the hot stamping process.

## 2.1 Hot stamping process: description and technology

Hot stamping was developed and patented (GB1490535, 1977) [4] by a Swedish company named Plannja that used the process for saw blades and lawnmower blades. In 1984, Saab Automobile AB was the first vehicle manufacturer who adopted a hardened boron steel component for the Saab 9000 [5]. The number of produced parts increased from 3 million parts/year in 1987 to approximately 107 million parts/year in 2007 [6]. The applied hot stamped parts in the automotive industry are chassis components, like A-pillars, B-pillars, bumpers, roof rails, rocker rails and tunnels, as shown in Figure 2.1 [7].

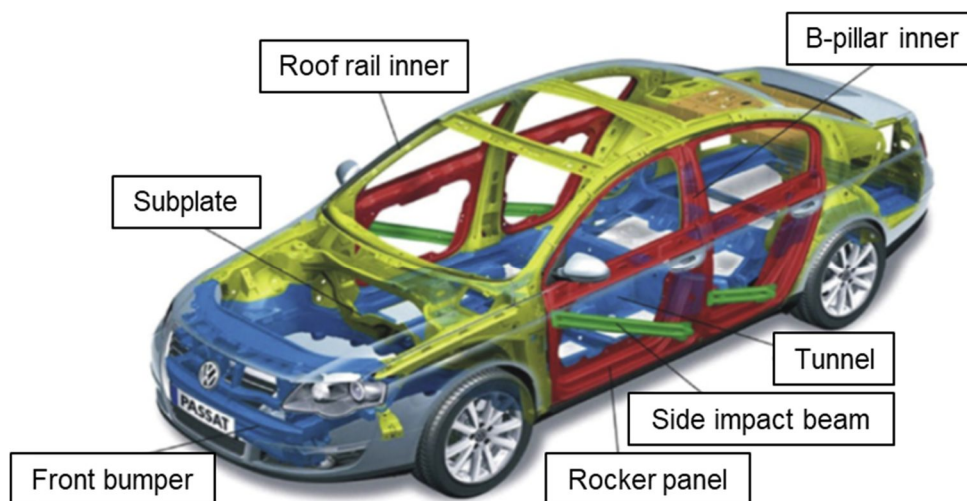


Figure 2.1: Hot stamped parts in a typical middle-class car [8].

The hot stamping process currently exists in two different main variants: the direct and the indirect hot stamping method. In the direct hot stamping process

the austenitization of the blank is prior to the forming stage, see Figure 2.2(a), while in the indirect hot stamping process, the austenitization stage is between the Forming and the quenching of the blank, see Figure 2.2(b) [9]. The reference for this work is the direct hot stamping process.

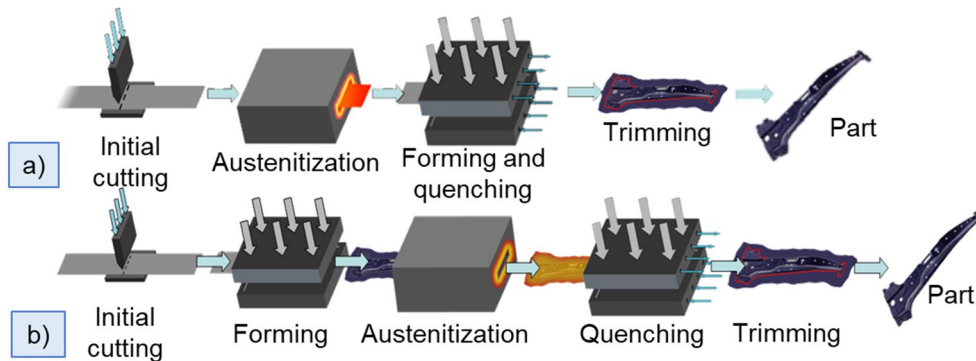


Figure 2.2: Basic hot stamping process chains: (a) direct hot stamping, (b) indirect hot stamping.

The blank, in its as-delivered conditions, presents a ferritic/pearlitic microstructure, with limited mechanical properties and a tensile strength between 400MPa and 600MPa. In the industrial process, the blank is heated in furnace up to the austenitization temperature, which ranges from 850°C to 1000°C, for several minutes in order to obtain a homogeneous austenitic microstructure of the sheet metal, then it is rapidly transferred to the water-cooled dies. There, the blank is deformed and quenched at the same time, following specific cooling paths in order to obtain a fully martensitic microstructure at room temperature, which guarantees strength levels above 1500MPa [10-12]. The total cycle time (transfer + forming + cooling into the die) requires approximately 15-25s and the formed component is then removed from the dies at about 150°C. If the part leaves the stamping line too early, particular attention should be paid to avoid thermal distortion or uncompleted martensitic transformation [13, 14]. Later on, the parts are usually drilled and trimmed through laser-cutting as well as conventional die-trimming.

## 2.2 Materials and coatings

The investigations on ultra-high-strength steels have shown that boron alloys of 22MnB5, 27MnCrB5, and 37MnB4 steel grades are the only steel grades that

produce a fully martensitic microstructure after hot stamping when a water-cooled tool is used [15]. The alloying elements change the characteristics of the steel [16].

- C, carbon: This is the most important and influential alloying element in steel. With increasing carbon content, the strength and hardenability of the steel increase, but its ductility, formability, weldability, and machinability are decreased;
- Mn, manganese: it is used as a deoxidizer. It contributes to strength and hardness, but to a lesser extent than carbon. Manganese has a strong effect on increasing the hardenability of steel by reducing the critical cooling rate;
- Cr, chromium: it is generally added to steel to increase resistance to corrosion and oxidation, to increase hardenability, and to improve high-temperature strength. Chromium is a carbide former, which increases edge retention and wear resistance;
- B, boron: it is the element that influences the hardenability the most, whereas boron slows down the conversion into softer microstructures and leads to a martensitic microstructure over the cross-section of the part.

The heat treatment applied to the blank can lead to excessive oxidation and decarburization if uncoated steels are used. Due to these oxide scale layers, a surface finishing operation (e.g. shot-blasting or sand-blasting) has to be performed after the hot stamping, thus increasing process time and costs. In order to avoid these problems, ArcelorMittal™ [17] developed a series of coatings that protect the steel sheet. The most diffused coating, generally applied to 22MnB5, which is used as press hardening standard material in the automotive industry all over the world [18], is an aluminium-silicon (AluSi®) coating. This metallic coating is generated in a continuous hot-dip galvanizing process and consists of 10% silicon, 3% iron, and 87% aluminium. During the heating of the coated blank, the steel diffusion process from the coating–substrate interface area to the coating surface is thermally activated. The Al-Si coating has a melting point of approximately 600 °C. However, due to the presence of Fe in the substrate, an Al-Fe alloy with a higher melting point grows from the interface with the base

---

metal and quickly reaches the surface. The Al–Fe alloy, which migrates to the surface, has a higher melting point and thus prevents the coating layer from melting. Due to the lower forming limits of the Al-Si layer compared to the base material in the initial state at room temperature, the hot-dip aluminized sheets cannot be used for the indirect process and they are not suitable for cold forming [19, 20]. Other types of coatings have been developed as an alternative to AluSi®, depending on the application of the steel: zinc, Zn, and its alloys are the most diffused and can be used also in the indirect hot stamping process.

The reference material for this work is 22MnB5, commercialized by ArcelorMittal™ with the name of Usibor 1500P®, with AluSi® coating.

## **2.3 Phase transformation kinetic**

In hot stamping process, there are basically two very important phase transformations occurring: the austenitization from the initial ferrite+pearlite mixture and the transformation of austenite to the final martensite, or bainite or a mixture of the two phases.

It has been proven that the initial conditions of the material can influence the final properties of the hot-stamped piece. A correlation between parent austenite grain size (PAGS) and mechanical properties after press hardening was observed. The smallest PAGS obtained in this study were attained for the steels having relatively uniform distribution of pearlite or cementite in ferritic matrix. It was seen that the parent austenite grains of these materials do not significantly grow between 180s and 450s austenitization at 900 °C [21].

The heating stage is delicate since it is mandatory that the whole blank reaches homogeneous austenite phase. The time and temperature of the austenitization stage plays a fundamental role, since the kinetic of the phase transformation is dependant from both those parameters: the higher the austenitization temperature, the less time is required to reach the fully austenite state, and, on the other hand, more time is required if a lower austenitization temperature is chosen. The heating rate plays a fundamental role itself, as demonstrated [22]: a higher heating rate, less time and a higher temperature are required to attain a certain volume fraction of austenite. Both temperature and time follow linear relationships with heating rate in logarithmic coordinates. The

effects of heating rate are greater on temperature than time for a larger amount of austenite formation.

Forming and phase transformations are performed in a single step simultaneously. It is well known that the forming process has to be extended in the austenite phase region, then the phase transformations result in martensite and/or bainite [23-25]. Applying hot mechanical work, as well as heat treatment, affects the physical and mechanical properties [26]. There are a lot of works that describe the effect of hot deformation on the formation of ferrite and pearlite in isothermal and non-isothermal conditions [27–30], but just few studies were focused on martensite and bainite transformations [31]. The phase transformation in continuous cooling conditions, which is the one occurring during the hot stamping process, is described by the Continuous Cooling Transformation (CCT) diagram, where the conditions of existence of the various phases is described in respect with the different cooling paths, as shown in Figure 2.3. According to the CCT diagram, the minimum cooling rate to obtain the bainite microstructure is  $27^{\circ}\text{C}/\text{s}$  and the temperature to obtain the martensite phase is  $400^{\circ}\text{C}$ . The conditions at which phase transformations occur during the hot stamping process are not the same at which the traditional CCT diagrams are drawn: in the first case, a deformation is applied to the blank, in the latter just a thermal cycle is applied to the blank.

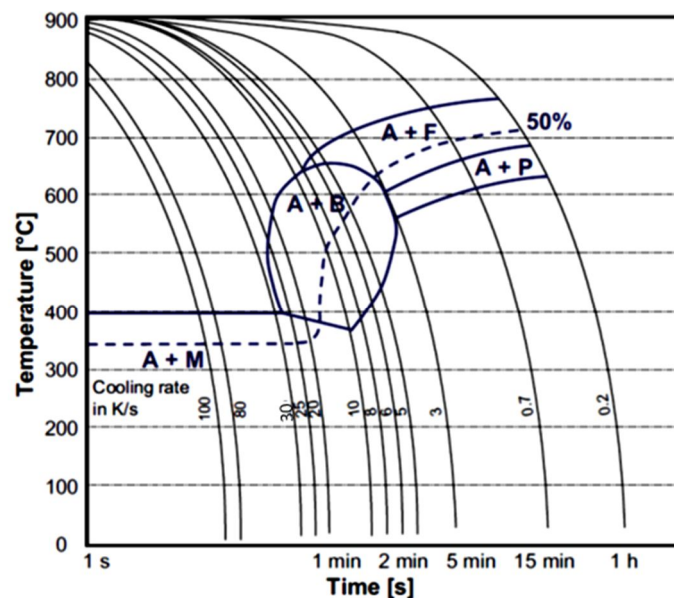


Figure 2.3: CCT diagram of Usibor 1500P® according to ArcelorMittal™ [17].

There are in fact some studies that state that the applied deformation can bring important modification to the final CCT diagram of steel. Barcellona and Nikravesht [32, 33] investigate the effect of applied strain on the resultant CCT. It was demonstrated by both research groups that the applied strain causes a shift to the left, so towards higher cooling rates, of the starting points of the bainite phase and a lowering of the martensite start points. In particular, Barcellona states that the increasing hot deformation values generate lower Vickers values at the same cooling rate which means that the increase of hot pre-strain shifts the CCT diagram toward lower times and, therefore, a lowering of the starting time for each transformation [32]. Nikravesht adds that the reduction of cooling rate always leads to reduction in  $M_s$  and  $M_f$  temperatures, if the final microstructure contained martensite only and that hot plastic deformation increases the mean value of  $B_s$  from 580 °C to 600 °C and its effect will be decreased by reduction of cooling rate [33]. This is of great importance when the cooling systems of the dies has to be studied: a left shift of the bainite start, means that a more severe heat removal is required to complete the deformation in austenite phase and avoid the bainite transformation, since it brings a severe rise in the flow curve of the material, as shown by Merklein et al. [34], and a consequent increase of the resistance of the material with possible crack formation.

## **2.4 Thermo-mechanical properties**

In hot stamping of HSS and UHSS sheets, the material thermo-mechanical and microstructural behaviours are strongly coupled and depend on many process parameters that affect the final part characteristics not only in terms of final shape and integrity, but also in terms of microstructural features and mechanical characteristics. Therefore, since the very first studies in this field, the accurate modelling of the material behaviour has been both an industrial and a scientific challenge, since it allows not only manufacturing high performing and defects-free parts, but also gives the chance of producing parts with tailored properties [35]. According to the description of the hot stamping process, it becomes evident that the study of the material microstructure must become the focus to calibrate the process and obtain the wanted characteristics, in particular in the transition areas, where only the correct mixture of phases can grant the goodness of the component. The use of numerical simulations to predict the final properties of

the stamped part is of great importance, but the requirement of data can represent a limit. The procedures for the flow stress determination presented in Turetta [18] and Merklein et al. [34, 36, 37] are still the basis of many other research works aimed at evaluating the flow stress behavior during the hot stamping process of UHSS (see for example the testing set-up developed in [37] in Figure 2.4a). Some advances were proposed to enhance the accuracy of the experimental data, as in the work by N. Li et al. [38] that developed a procedure to correct the flow stress curves from uniaxial tensile tests by taking into account both the temperature rise due to the plastic deformation and the actual strain values after necking. In the work of Abspoel et al. [39] a new specimen shape was designed in order to obtain constant current density all over the specimen length during the deformation when using a direct electrical heating system. However, this kind of solution proved to be effective only before the strain localization onset. It is worth to underline that most of the works dealing with the flow stress determination are focused on strain rate ranges that are in the lower part of the range usually involved in the industrial hot stamping processes. In fact, whereas the strain rate domain usually investigated is from  $0.01$  to  $1 \text{ s}^{-1}$ , it would be preferable to extend it till  $10\text{-}50 \text{ s}^{-1}$  to cover the actual industrial range.

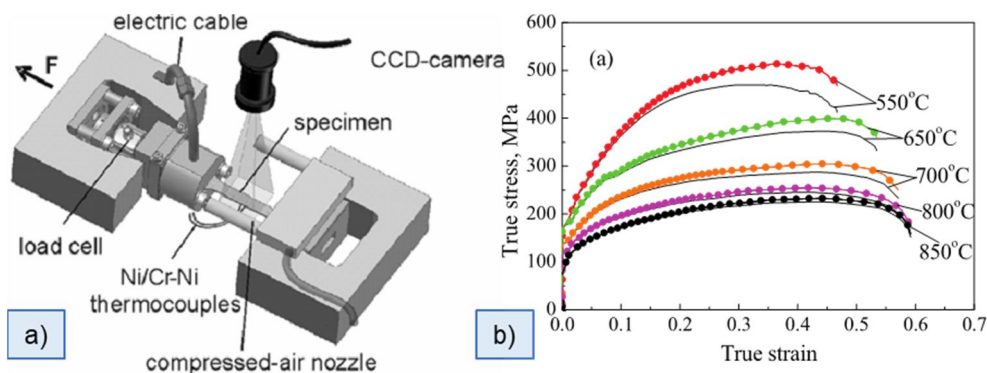


Figure 2.4: a) Experimental apparatus used by Merklein et al. [37], b) example of temperature dependency of the flow curves [38].

While the ferrite+pearlite and the austenite phases have been widely studied and analysed through tensile tests, when investigating both the flow curves in different conditions, namely varying temperature and strain rate [34, 37, 40], and the influence of the phase transformations on the flow curves [7, 41], the bainite and martensite phases have been studied only in very specific conditions [41] or through compression tests because of (i) their high strength and low plasticity

[40], and (ii) the easiness in controlling fracture onset, avoiding problems due to presence on different phases in the same specimen.

The flow stress of the phases is usually modelled through either empirical or physically-based equations taking into account the effect of the strain, strain rate and temperature, in order to implement the obtained flow curves in the numerical model. Zhou et al. [42] proposed a modified Arrhenius constitutive model including the influence of the strain in the material coefficients, which was proved to slightly enhance the prediction accuracy compared to the unified viscoplastic constitutive equations based on the dislocation density evolution. In the already cited work of Abspoel et al. [39], the Authors derived a Kocks–Mecking model from the tensile data, providing the material coefficients needed for the hardening description. By correlating these parameters with the strain rate and temperature, a parametric model was proposed to describe hardening curves within the hot stamping domain for austenitic forming conditions. The measurements and the calculated curves were found to be in good agreement and the material model was further validated proving to be capable of predicting the final thickness of a hot-stamped piece. H. Li et al. [40] used the modified Arrhenius model to describe the flow behaviour of samples with austenitic microstructure, and the modified Johnson-Cook model to describe the one of samples with ferritic-pearlitic, bainitic or martensitic microstructure (the first studied through tensile tests, the latter through compression tests). The derived models were proved to be suitable for the development of a more general model coupling the mechanical characteristics of each phase with the phase transformation kinetics.

## **2.5 Formability**

The determination of the metal sheet formability is a major issue for a proper design and optimization of the hot stamping process due to its dependence on a number of different parameters. In fact, the material mechanical, thermal and microstructural characteristics and process conditions all play a major role in its determination. Different methodologies have been proposed in order to evaluate formability through experimental testing. They offer various levels of completeness and accuracy, on the basis of the test complexity, and range from uniaxial tensile tests to determine just the material ductility, to simulative tests

reproducing the actual process features, such as cupping and bulging, to more complex procedures such as Nakajima and Marciniak tests able to give a comprehensive description of the material formability in terms of Forming Limit Curves (FLCs) [43]. The Marciniak test [44] makes use of a flat punch and an additional driving blank, which prevent the friction to occur and therefore assure the fracture location close to the apex of the punch. The use of blanks of various widths allows tracing a complete FLC. The Nakajima [45] method instead makes use of a hemispherical punch and a special lubrication system consisting of an elastic pad, lubrication oil and normally a Teflon or graphite foil.

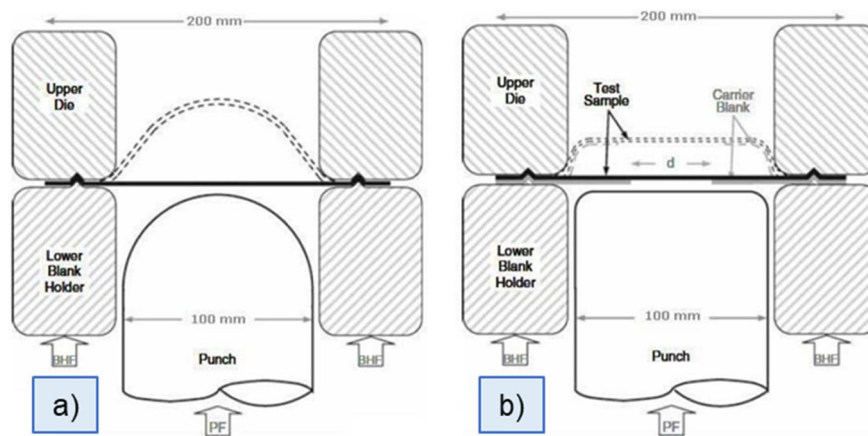


Figure 2.5: a) Nakajima test setup, b) Marciniak test setup according to ISO standard [46].

The relationship between the major and minor strains is set by the width of the strip specimen or the size of the notches, if circular blanks are chosen for tracing the FLC [47]. The test scheme and procedure are according to the ISO 12004-2-2008 standard about the determination of forming limit diagrams of sheet metals [46], which have been properly adapted for testing at elevated temperature. FLCs at high temperatures are mainly obtained through stretching tests that produce out-of-plane deformation of the specimen. The metal sheet specimen is firstly marked with a grid pattern (i.e. either inks capable to resist at temperature up to 950°C or photo-chemical etching), then fixed in the tools before being heated up. Once obtained the full austenitization of the specimen, the temperature is lowered down to the test temperature, and then stretched keeping constant the temperature during the overall testing duration. The major and minor strains of the grid pattern are measured in those regions where the fracture occurs, typically using DIC techniques [48]. To this regard, Merklein et

al. [49] developed a new time-dependent procedure to elaborate the DIC data for the FLD elaboration, proposing a modification of the 12004 standard for the elaboration of DIC data in Nakajima tests. The specimens can be heated either in external furnaces (i.e. electric furnaces [50]) and then moved to the dies, or directly in situ being the specimen already fixed in the dies (i.e. induction heating [51] as well as heating chambers [53]). The latter benefits of better control of the specimen temperature, while the former suffers from the loss of temperature during the handling and fixing operations between the dies. In the stretching tests, sheets of different widths are clamped between the die and the blank-holder and stretched by the action of a punch, providing adequate lubrication between the sheet and the punch. Graphite lubricants are commonly used to minimize the impact of friction during the testes. The most popular testing configuration is still the Nakajima set up [51, 53] which uses a hemispherical punch, a circular die, and simple rectangular sheet specimens, providing a fast way to cover the whole FLC domain. Common difficulties of such configuration lie in the influence of (i) the friction coefficient that moves the fracture away from the punch dome, (ii) non homogeneous thermal fields determined by local cooling in the contact areas with the tools, and (iii) local instabilities of the specimen due to thermal distortions at high temperatures.

The parameters that influence the FLCs are the thickness of the material and the temperature at which the test is performed. As well as the flow curves, the microstructural evolution that the material undergoes during the hot stamping process can affect the formability, enhancing or drastically reducing the capability of the material to deform under a certain load. The correlation between the formability and microstructural characteristics of the 22MnB5 over the process temperatures was investigated in the works of Cho's et al. [54, 55] and in those of Guler's et al. [56, 57]. The change of the different microstructural phases was always represented through the CCT diagrams that were strictly depending on the alloying elements' percentages [55], and in particular on the Boron content [54]. It was shown that also the impurity segregation to grain boundaries [56] and the Dynamic Recrystallization (DRX) at the highest temperatures [57] might have a relevant influence on the material formability, with non-linear behaviour, especially at high temperatures.

## 2.6 Numerical simulations

In the sheet metal forming industry, FE codes are widely used to predict and optimize manufacturing operations and to assess the forming feasibility of a part, reducing lead times and costs [58, 59]. The introduction of temperature as an additional variable strongly influences the constitution of the finite element models and enhance their complexity compared to traditional sheet metal forming at room temperature [60, 61]. The main targets to be optimized in press hardening simulations are the part geometry and the process parameters which guarantee a successful forming avoiding excessive wrinkling and thinning. In particular, the thickness distribution is used as input data in further crash simulations and the thermo-mechanical history of the material model is of great importance to reduce the residual stress state that is responsible for the distortion of the final component [62, 18]. The correct design of the forming and cooling phases requires the utilization of FE codes where the process has to be modelled through a fully coupled thermo-mechanical-metallurgical model (Figure 2.6). The accurate calibration of such a model represents a strong requirement to gain reliable results from the FE simulations of the hot stamping process, and besides the parameters that are necessary for the simulation of conventional stamping, several materials and process parameters and boundary conditions need to be additionally considered. In particular, data about the elastoplastic properties of the material as a function of temperature and strain rate, the sheet formability as well as the influence of applied stress and strain on the phase transformation kinetics have to be properly evaluated and implemented [37, 18].

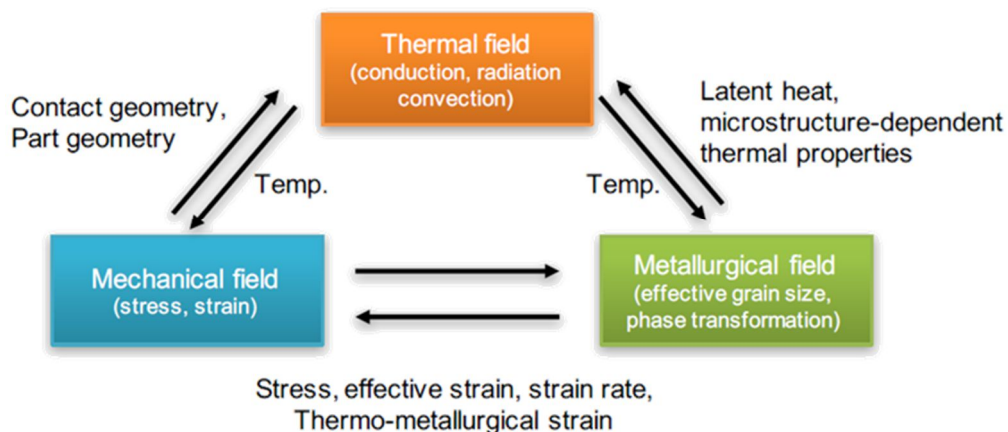


Figure 2.6: Fully coupled thermo-mechanical-metallurgical model scheme [64].

There is nowadays a huge offer of software and material models that are capable of coupling the phase transformation kinetics to the traditional stamping deformations. One of the most widely used software is LS-DYNA, which offers a huge freedom in the design and setup of the simulations, and offers a series of material models that can foresee the phase transformation, which is an aspect of fundamental importance in the hot stamping process.

In 2009, the material model number 244 was first introduced in LS-DYNA code. It is based on, but not restricted to the work of Akerstrom [65] and implemented by Olsson [66]. The material model was applied to the Numisheet 2008 benchmark 3 test to compare the experimental results with the results of the numerical simulations. The benchmark is based on continuous press hardening of a boron alloyed steel, in this case, a b-pillar. The material used in the simulation is a 22MnB5 allow with thickness equal to 1.95 mm. the material parameters are taken from the benchmark test and input data from the hardening phases were taken from Sjöström [67]. The validation shows a very fine agreement, the necking is clearly captured and the thickness corresponds very well to the experimental test. Figure 2.7 shows the results of the comparison between the simulation and the Numisheet 3 test.

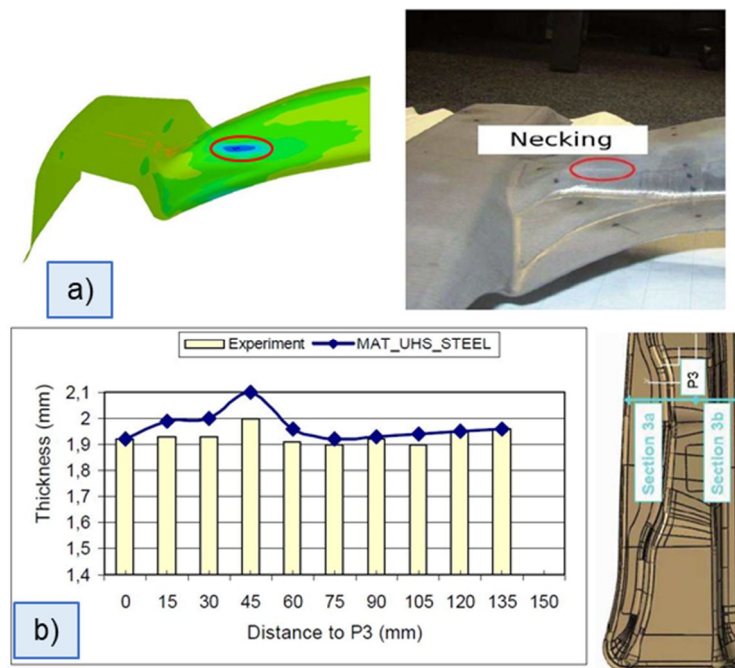


Figure 2.7: a) Necking prediction, b) Thickness comparison [66].

## 2.7 Damage modelling

As presented in section §2.5, the FLC can be used as a damage criterion, since it defines the characteristics of the deformation which lead to the rupture. According to the experimental studies of Müschenborn and Sonne [68], Kleemola et al. [69], Bergström and Ölund [70], Graf and Hosford [71] and others, the conventional FLCs are applicable only to forming processes with almost linear and unbroken strain paths. These proportional loading conditions are unlikely to occur in many forming processes with changing loading directions such as two-step forming operations. For this reason, many authors have proposed alternative criteria such as Yao and Cao [72], Stoughton and Zhu [73], Hora and Tong [74] and Volk [75], who proposed the Generalized Forming Limit Concept (GFLC). Andrade and Feucht [76] compared three models that can be implemented in the LS-DYNA code, namely Gurson-Tvergaard-Needleman (GTN) [77-79], Cockcroft-Latham (CL) [80] and the Generalized Incremental Stress State Model (GISSMO) [81-82]. The last one appeared to be particularly suitable when applied to many sheet forming analyses due to the easy calibration of the constitutive parameters and the possibility of coupling with different plasticity models. The latest upgrade in the damage criterion, presented by F. Andrade, T. Erhart, A. Haufe [83], allows the application of the damage criterion to both isotropic and anisotropic materials, which means that can predict the differences in the fractures that depends on the orientation of the metal sheet.

The Generalized Incremental Stress State Model (GISSMO) is a phenomenological formulation developed by Neukamm et al. [81] and later presented by Andrade et al. [82] that allows for an incremental description of damage accumulation, including softening and failure. The initial development aimed at modelling of forming and crash using the same damage model for both simulation steps and accumulate damage of the forming analysis for further use in crash analysis. The model is based on the correlation of the triaxiality,  $\eta$ , with the values of strain at failure and of the instability strain. The triaxiality is calculated according to Eq. (2.1):

$$\eta = \frac{\sigma_h}{\sigma_{vm}} \quad (2.1)$$

Where  $\sigma_h$  is the hydrostatic stress and  $\sigma_{vm}$  is the Von Mises equivalent stress. The treatment of post-localization is done through the definition of a mesh size regularization. This is realized through the damage formulation. A mesh size

dependent failure strain is formulated for energy regularization. The damage is coupled to the stress tensor in post-localization deformation. The damage variable,  $\dot{D}$ , is described as an exponential function:

$$\dot{D} = \frac{n}{\varepsilon_f(\eta)} D^{(1-\frac{1}{n})} \dot{\varepsilon}_p \quad (2.2)$$

Where  $D$  is the current value of the damage,  $\dot{\varepsilon}_p$  is the equivalent plastic strain rate,  $n$  is the damage exponent and  $\varepsilon_f$  is equivalent plastic strain at fracture [84]. The instability measure  $\dot{F}$ , which represents the necking onset, is therefore formulated according to the following:

$$\dot{F} = \frac{n}{\varepsilon_{inst}(\eta)} F^{(1-\frac{1}{n})} \dot{\varepsilon}_p \quad (2.3)$$

The difference between functions  $\dot{D}$  and  $\dot{F}$  is represented by the limiting strain that are considered:  $\varepsilon_f$  and  $\varepsilon_{inst}$  that are respectively the strain at fracture and instability strain. When the instability is reached,  $F=1$ , it is assumed that damage is coupled to the stress tensor using Lemaitre's (1985) effective stress concept.

$$\sigma_{eff} = \sigma \left[ 1 - \left( \frac{D-D_{crit}}{1-D_{crit}} \right)^m \right] \quad (2.4)$$

The value for  $D_{crit}$  is determined as the onset of necking is reached. The exponent  $m$  is termed fading exponent, it allows for a regularization of fracture strain and the energy consumed during post-instability deformation [85, 86].

The GISSMO damage criterion is starting to become more and more used, in particular, if multi-stage or incremental processes are involved, since the FLC fails to correctly represent the behaviour of the material. The majority of the studies is carried out at room temperature, but, for the hot stamping process, a set of data at high temperature, so in the condition at which the deformation in the hot stamping process normally occurs, is necessary and no such information is present in literature yet.

## 2.8 Aim of the work

The present work is articulated in different fields of research, each one with a specific placement inside the framework of the presented state of the art:

- Phase transformation kinetic: a set of experimental data relative to the batch of material which will be the focus of the whole work, is of fundamental importance. Moreover, the cooperation with Ford GMBH enhanced the connection between the research and the industrial problem, focusing the research in a specific set of experimental tests and numerical simulations aimed to understand not only the behaviour of the material on its own, but also the behaviour of the material in the specific context of the hot stamping process, helping the development of the process itself;
- Thermo-mechanical properties: the literature in this field is quite vast, if tensile tests data regarding the austenite phase or the ferrite + pearlite mixture are needed. The lack of the state of art regards the tensile tests of bainite and martensite phases, and this work aims to fill this lack with a complete set of tensile tests data which regards all the phases, namely austenite, ferrite + pearlite, bainite and martensite. These data are presented with a modified Johnson-Cook fitting model which can describe the entire rheology of the material and can be implemented in the FE models. The anisotropy of the material in hot conditions was also investigated, in order to obtain a set of data relative to the batch of material used in the whole work. The cooperation with Ford GMBH helped understanding the material properties in the usual conditions of the hot stamping process, and developing a more suitable condition to perform the deformation during the forming step;
- Formability: in literature, the data of the formability are often relative to the cold condition, but just very few research groups presented data of the formability in hot conditions. For this reason, hot Nakajima tests were performed, studying the influence of the temperature and of the microstructure on the FLC. The cooperation with Ford GMBH helped the understanding of the material behaviour in the conditions of the hot stamping process, and all the possible ways to enhance the process itself;
- Damage modelling: the GISSMO damage criterion is a quite new way to model the damage and fracture on materials, and it is usually

applied at room temperature. This work aims to apply the GISSMO damage criterion at high temperature, in the conditions at which the deformation occurs during the forming stage of the hot stamping process, so at high temperature.

This work aims to deepen the knowledge of the 22MnB5 material, performing numerous experimental tests coupled with the numerical simulations, aimed to calibrate the material model and the damage model. The smaller the differences between the simulation and the experimental test, the higher the precision when the simulation is aimed to reproduce more complex processes.

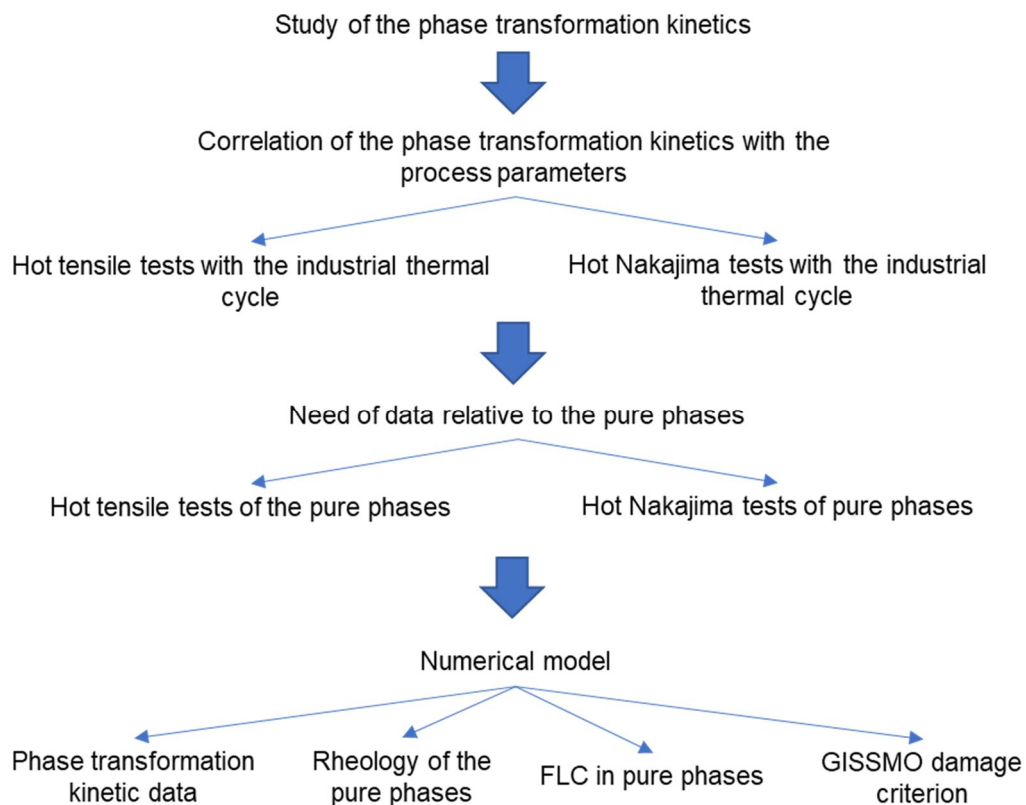


Figure 2.8: Flow chart of the activities performed for the thesis work.

## **CHAPTER 3**

### **Experimental equipment and procedures**



The aim of this Chapter is to present the material chosen for this work in detail, along with the equipment and the procedures that were used and followed to perform all the experimental tests useful for the development of this work. Depending on the type of test, a specific experimental apparatus was used and the procedures optimized in order to obtain a reliable set of data that can accurately describe the behaviour of the material.

### 3.1 Material 22MnB5

The material chosen for this work is 22MnB5 steel. Steel grade 22MnB5 in accordance with DIN EN 10083-3 is one of the boron-alloyed quenched and tempered steels. These grades are characterized in particular by their formability in the hot rolled state and their high strength after the heat treatment. The strength characteristics after quenching and tempering are achieved in particular by the low boron content, in addition to the carbon and manganese [87]. Boron, in its atomic state, is added to alloyed and unalloyed steels to enhance the hardness level and its effect is evident even if boron is added in very small concentration, i.e. 0.001%. The effect of boron depends also on the amount of carbon in steels, in particular, the hardenability increase with the inverse proportion to the percentage of carbon. If boron is added up to 0.01% to austenitic steels improves their high-temperature strength. On the other hand, boron is dangerous if added in high quantities: boron constituents become segregated in the austenite grain boundaries and this lowers the hardenability, decreases the toughness and causes embrittlement. [88]

*Table 3.1: Nominal composition of 22MnB5 [17]*

<b>Element</b>	<b>Max %</b>
<b>C</b>	0.25
<b>Si</b>	0.4
<b>Mn</b>	1.4
<b>P</b>	0.03
<b>S</b>	0.01
<b>Al</b>	0.01-0.1
<b>B</b>	0.005
<b>Ti+Nb</b>	0.12
<b>Cr+Mo</b>	1
<b>Fe</b>	Base

The 22MnB5 used for this experimental campaign has a thickness of 1.20 ( $\pm 0.05$ ) mm and 1.50 ( $\pm 0.05$ ) mm with an Al-Si coating on its surface. The base microstructure of 22MnB5 is constituted by a mixture of ferrite and pearlite in a percentage of about 60-40%. The thermal treatment applied in the usual hot stamping process transforms the ferrite-pearlite mixture to austenite and then, thanks to the fast cooling, the austenite transforms into martensite, as shown in Figure 1c, or a mixture of martensite and bainite.

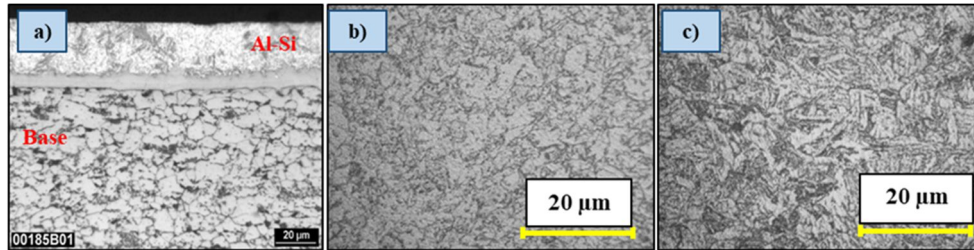


Figure 3.1: Microstructure of 22MnB5 in a) cross-section [89] b) as-delivered condition c) after thermal treatment [7].

### 3.2 Study of the phase transformation kinetics

As known from literature, steel can undergo a number of microstructural evolutions, depending on the thermal cycle that is applied to the metal sheet. For this reason, it is of fundamental importance to understand the conditions that lead to wanted or unwanted microstructures. The phase transformation kinetic studies regarded three aspects:

1. Collect the data to draw the specific CCT diagram of 22MnB5;
2. Study of the effect of applied pre-strain on the left-shift of the curves in the CCT diagram;
3. TTT curves for the phase transformation at constant temperature.

To perform these series of tests, the Gleeble 3800® (1) thermo-mechanical simulator was chosen and the experimental setup is shown in Figure 3.2. The Gleeble 3800® has a resistance heating system integrated that allows the heating of the specimen (2) through Joule effect, and the variation of the temperature at 1000°C is  $\pm 1^\circ\text{C}$ . The high precision in the control of the temperature makes the Gleeble 3800® the perfect tool to study the effect of the applied thermal cycle on the phase transformation kinetics of 22MnB5. The temperature of the specimen

was measured through a K-type thermocouple (5) spot welded on the centre of its gauge length, with the aim of monitoring and controlling the heating cycle parameters. A dilatometer (3) was used to monitor the tests and register the phase transformations through the dilatation or shrinkage of the specimen. An air nozzle (4) was placed above the specimen and used to cool it down at the chosen cooling rate. The specimen geometry was designed according to the UNI EN ISO 6892: 2016 standard and it is shown in Figure 3.3. The specimen thickness for this experimental campaign was 1.20 ( $\pm 0.05$ ) mm.

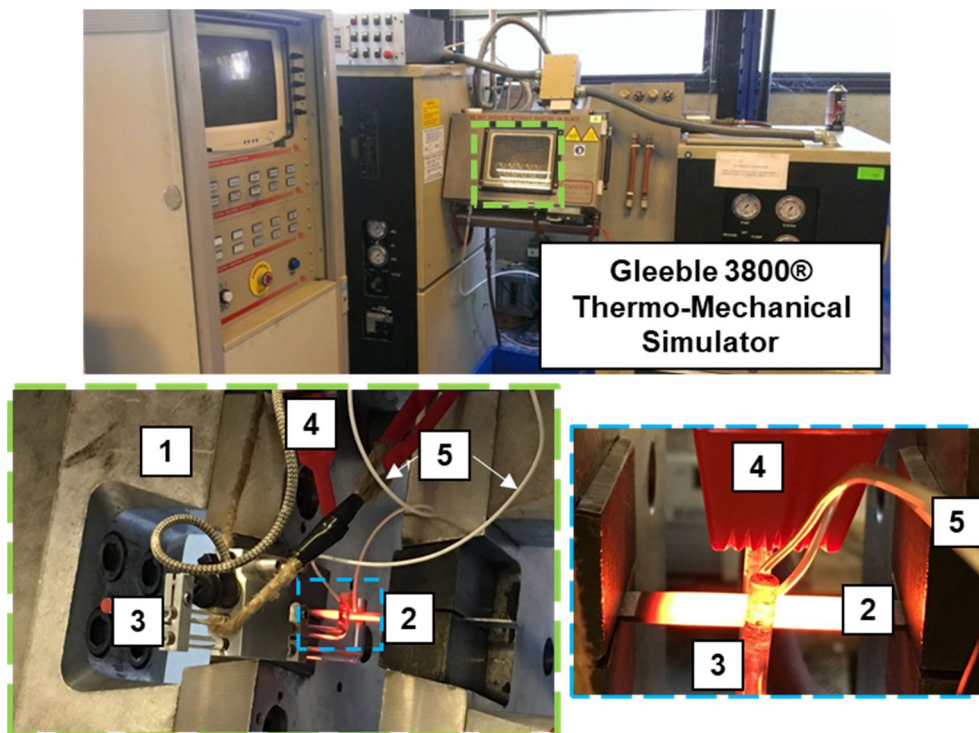


Figure 3.2: Gleeble 3800® equipped for the phase transformation kinetic tests.

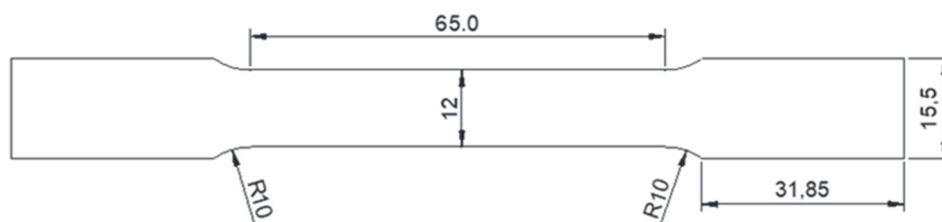


Figure 3.3: Specimen used for the phase transformation kinetic tests.

The thermal cycle applied to the specimen for the first part of the experimental plan, namely the drawing of the CCT diagram, is shown in Figure 3.4(a). The specimen is heated up from room temperature up to the austenitization temperature ( $T_{\text{aust}}$ ), namely  $950(\pm 1)^{\circ}\text{C}$ , with a heating rate of  $3(\pm 1\%)^{\circ}\text{C/s}$  and the specimen is then kept at that temperature for 6 minutes, in order to allow the complete transformation of the initial ferrite + pearlite mixture into austenite. Thanks to the air nozzle, the specimen is cooled down to room temperature with different cooling rates, starting from  $5(\pm 1\%)^{\circ}\text{C/s}$  to  $100(\pm 1\%)^{\circ}\text{C/s}$ , as reported more in detail in Table 3.2.

The thermal cycle applied for studying the effect of an applied pre-strain to the left-shift of the CCT curves is shown in Figure 3.4(b). After the first austenitization, the specimen is cooled down with a cooling rate of  $80(\pm 1\%)^{\circ}\text{C/s}$  at the temperatures at which the pre-strain is applied, namely  $700(\pm 1)^{\circ}\text{C}$  and  $800(\pm 1)^{\circ}\text{C}$ . Different amount of percentage pre-strain were applied (see Table 3.2) and two different strain rates, namely  $0.1\text{ s}^{-1}$  and  $1\text{ s}^{-1}$ , were chosen to apply the pre-strain to the specimen. At high temperature, the same amount of pre-strain, but applied with different strain rate, describes a different tensile state of the specimen and this can lead to different effect on the resultant CCT. After the application of the pre-strain, the specimen is then cooled down with different cooling rates, starting from  $5(\pm 1\%)^{\circ}\text{C/s}$  to  $100(\pm 1\%)^{\circ}\text{C/s}$ , as reported more in detail in Table 3.2.

*Table 3.2: Experimental plan for the phase transformation kinetics study.*

<b>Aim</b>	<b>Cooling rates (<math>^{\circ}\text{C/s}</math>)</b>	<b>Pre-strain</b>	<b>Repeatability</b>
<b>CCT diagram</b>	10, 15, 20, 25, 27, 30, 33, 35, 40, 50, 60, 80	-	
<b>CCT curves left-shift</b>	20, 25, 27, 30, 33, 35, 40, 50, 60, 80	T= 700, 800 $^{\circ}\text{C}$ %=5, 10, 15, 20 s.r.= 0.1, 1 $\text{s}^{-1}$	3

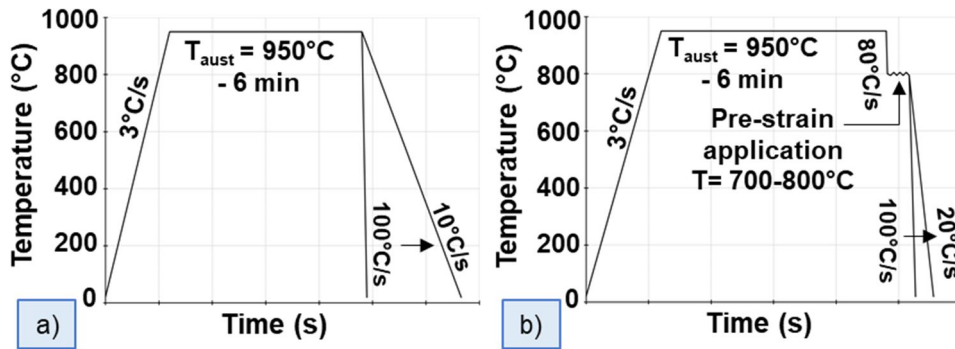


Figure 3.4: thermal cycle applied for the a) CCT diagram drawing and b) CCT curves left-shift.

The last important aspect that was studied as preliminary for the following tensile or Nakajima tests are the TTT curves for a set of specific temperatures, namely 450°C, 500°C, 550°C and 600°C, to understand the kinetic of transformation of austenite into bainite at those temperatures. Figure 3.5 shows the thermal cycle applied for this set of tests, which consists on a first austenitization, then the specimen is cooled down with a cooling rate of 100(±1%) °C/s at the temperature selected and kept at that temperature for 360 s. All these tests are performed using the dilatometer, fundamental to detect the dilatations or contractions of the specimens due to the phase transformation. The results are a set of saturation curves, which describes the time necessary to reach a wanted percentage of bainite in the specimen.

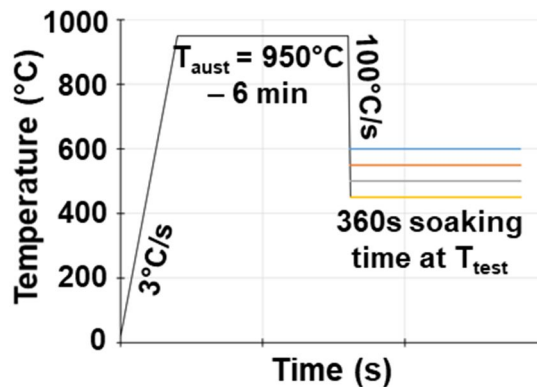


Figure 3.5: Thermal cycle applied for the study of the phase transformation kinetics at constant temperature.

### 3.3 Equipment and procedures for tensile tests

Experimental hot tensile tests were all carried out by using a 50kN servo-hydraulic dynamometer MTS 322, shown in Figure 3.6. The MTS 322 (1) is not equipped with an integrated heating system, so an electrical power generator was connected to the hydraulic wedge thanks to special PEEK-Cu grips (4), designed to grant the correct passage of the current together with an adequate insulation with the structure. The specimen (2) was covered with a stochastic black and white pattern and all the tests were filmed using a CCD Pike camera (5) and the frames were analysed with GOM Aramis™ in order to obtain the true strain data.



Figure 3.6: MTS 322 equipped for the hot tensile tests.

The GOM Aramis™ transforms the acquired frames into a set of strain data, using the deformation of the stochastic pattern dots as a reference to the deformation of the specimen. The definition of an element size, allows the program to convert the image into a series of mesh element where a series of parameters can be displayed, using colour maps, or plotted in graphs selecting the desired points. Figure 3.7 shows the Aramis elaboration.

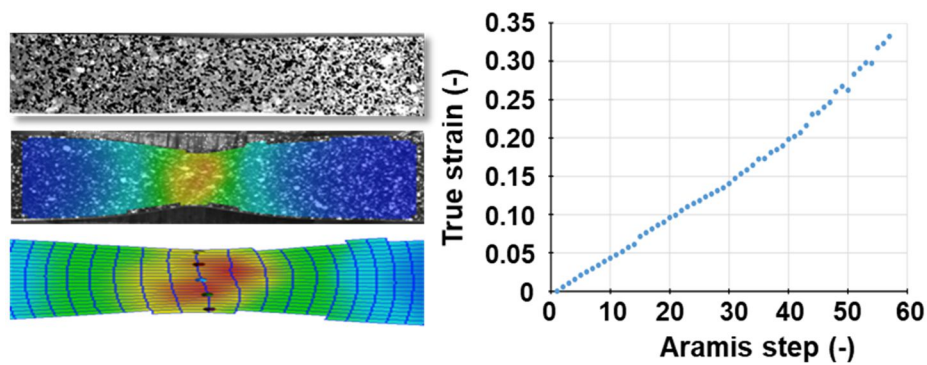


Figure 3.7: Aramis<sup>TM</sup> elaboration and resultant strain plot.

The specimen used for the hot tensile test was the standard dog-bone specimen according to UNI EN ISO 6892: 2016 standard, shown in Figure 3.3, with a thickness of  $1.20 (\pm 0.05)$  mm. The gauge length of the specimen was determined bringing the specimen at  $950 (\pm 1\%)$  °C and filming the test with a thermo-camera (6). The gauge length is of fundamental importance in order to determine the correct speed of the test to assure the wanted strain rate. Figure 3.8 shows the thermo-camera frame and the measured temperature, allowing the determination of the gauge length, which is  $30 (\pm 2)$  mm.

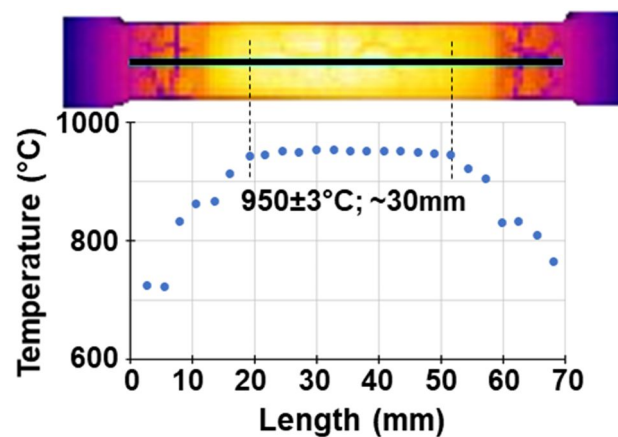


Figure 3.8: Specimen used for the hot tensile tests.

### 3.3.1 Preliminary studies on Austenite phase

According to the literature review (§2.3) and in particular the CCT diagram of steel, some conditions of cooling rates and temperatures that are critical, because the possibility of unwanted phase transformations is real and absolutely has to be avoided if a good final component is wanted. For this reason, the very

first tests performed on 22MnB5 regarded the correct combination of testing temperature and strain rate to avoid unwanted phase transformation during the tensile test. Figure 3.9 shows the thermal cycle applied to the tests aimed to study the effect of the testing temperature and the strain rate on the flow curves. The specimens were heated up with a heating rate of  $3(\pm 1\%)$  °C/s to 950 ( $\pm 1\%$ ) °C, then kept for 360 s at that temperature, cooled down to the chosen testing temperatures, with a cooling rate of  $35(\pm 1\%)$  °C/s and then, after 3 s of holding time at  $T_{\text{test}}$ , the mechanical deformation occurred. Table 3.3 reports in detail the experimental campaign plan. After the tensile tests, in order to highlight the microstructure, each sample was cut and incorporated in epoxy resin, ground and polished to a mirror finish using SiC paper up to 4000P, followed by 6, 3 and 1  $\mu\text{m}$  diamond paste. The samples were then treated with 5% Nital solution for 5s, in order to highlight the microstructure and analyse it with an optical microscope up to 1000X of magnitude.

Table 3.3: Experimental plan for the preliminary studies.

Aim	$T_{\text{aust}}$ (°C)	$T_{\text{test}}$ (°C)	Strain Rate (s <sup>-1</sup> )	Repeat-ability
Influence of $T_{\text{test}}$	950	500, 550, 600	0.01	3
Influence of strain rate	950	550	0.01, 0.05, 0.1	

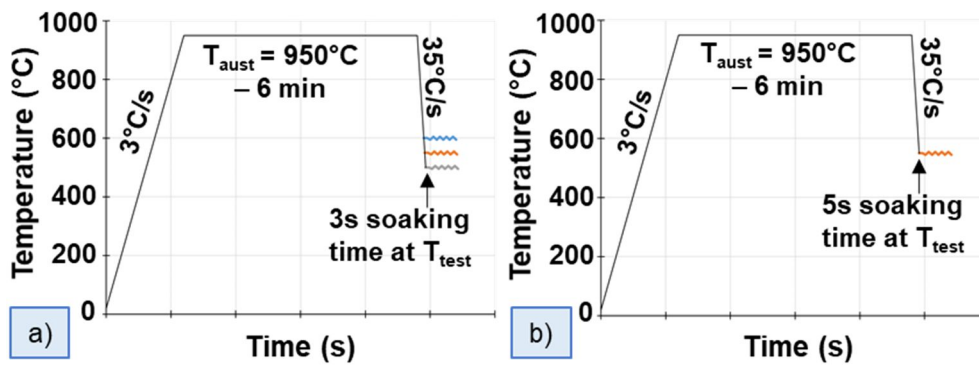


Figure 3.9: Thermal cycle applied for the study of a) the influence of  $T_{\text{test}}$  and b) the influence of strain rate.

### 3.3.2 Ferrite + Pearlite and Austenite phases' rheology

Figure 3.10(a) shows the thermal cycle used to test the ferrite+pearlite mixture, which consists of a heating at  $10(\pm 1\%)$  °C/s up to the testing temperature according to Table 3.4, and the mechanical testing started after 5 s of holding time at  $T_{\text{test}}$  to homogenize the temperature. The austenite phase is tested according to the temperature cycle of Figure 3.10(b), which consists of a heating at  $3(\pm 1\%)$  °C/s up to the austenitization temperature, namely  $950 (\pm 1\%)$  °C, followed by a soaking time of 360 s and a cooling at a rate of  $80(\pm 1\%)$  °C/s down to the temperature of the mechanical testing that is carried out after 3 s of holding time to stabilize the gauge length temperature. The latter is controlled by an infrared pyrometer that is used to adjust the air flow through the nozzles (3) that allow the controlled cooling (see Figure 3.6).

Table 3.4: Experimental plan for the hot tensile tests of Ferrite+Pearlite and austenite.

Phase	Temperature (°C)	Strain Rate (s <sup>-1</sup> )	Repeatability
Ferrite + Pearlite	Room T, 100, 200, 300, 400, 500, 600, 700, 800	0.1, 1, 10	3
Austenite	500, 550, 600, 650, 700, 750, 800, 850	0.1, 1, 10	

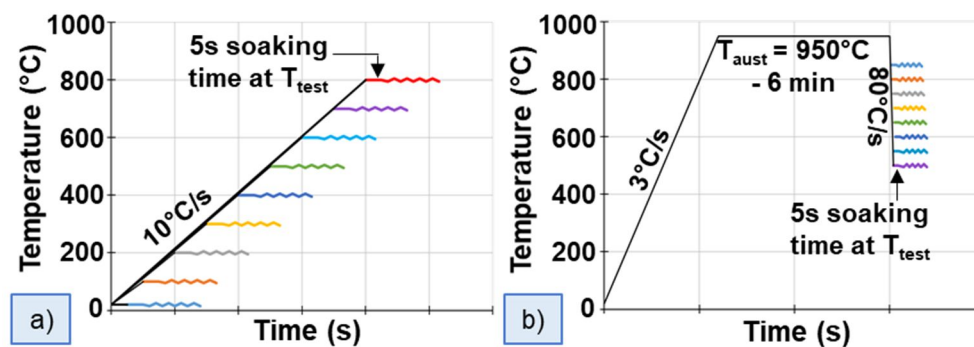
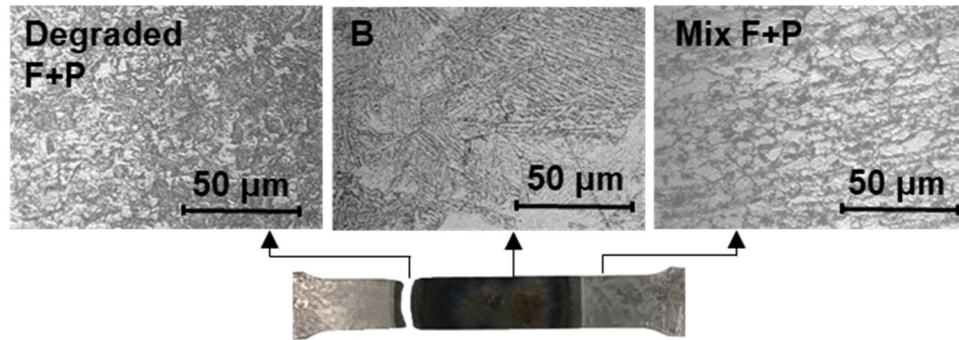


Figure 3.10: Thermal cycle applied for the hot tensile test of a) ferrite + pearlite mixture and b) austenite phase.

### 3.3.3 Bainite and Martensite phases' rheology

Due to their high strength, the bainite and martensite phases cannot be treated and tested using the method described in §3.3.1. In fact, by using the Joule effect set-up it is possible to accurately control the microstructural transformations, and

consequently the strength, in the gauge length, but the neighbouring areas that are not austenized, remain with a ferrite+pearlite microstructure as shown in Figure 3.11. Due to the prolonged exposition to temperatures around 800°C, these areas have poor mechanical properties due to the relevant grain growth and become preferential for the rupture during the tensile test.



*Figure 3.11: Microstructure distribution on the tensile specimen due to the Joule effect.*

To avoid such problem, a new set-up was developed to produce specimens having fully martensitic or the bainitic microstructures. Figure 3.12(a) shows the heating stage that was designed to be able to thermal treat 450x45mm strips. The equipment was made of copper grips, where the electrical power generator cables are connected (2), and air nozzles made with aluminium tubes to grant the homogeneous cooling over the entire stripe length (3). The temperature profile was controlled using an infrared pyrometer (4) positioned to measure the temperature of the centre of the strip. Figure 3.12(c) shows the thermal cycle used to produce the specimens, which consists of a heating at  $3(\pm 1\%)$  °C/s up to the austenitization temperature, followed by a soaking time of 360 s and a cooling at a rate of  $100(\pm 1\%)$  °C/s down to 450°C for the full bainitic transformation, and then a final cooling down to room temperature  $80(\pm 1\%)$  °C/s. After the thermal treatment, two standard dog-bone specimens per stripe were water cut to avoid the re-heating of the specimen edges. The mechanical cycles were then performed on the dynamometer according to the experimental plan presented in Table 3.5, by applying a heating rate of  $10(\pm 1\%)$  °C/s to avoid a too long permanence in temperature of the specimen, with possible deterioration of the microstructure. The two highest temperatures were chosen according to the

Continuous Cooling Transformation (CCT) diagram which describes the field of existence of the different phases.

Table 3.5: Experimental plan for the hot tensile tests of bainite and martensite.

Phase	Temperature (°C)	Strain Rate (s <sup>-1</sup> )	Repeatability
Bainite	Room T, 100, 200,	0.1, 1, 10	3
	300, 400, 500, 600		
Martensite	Room T, 100, 200, 300		

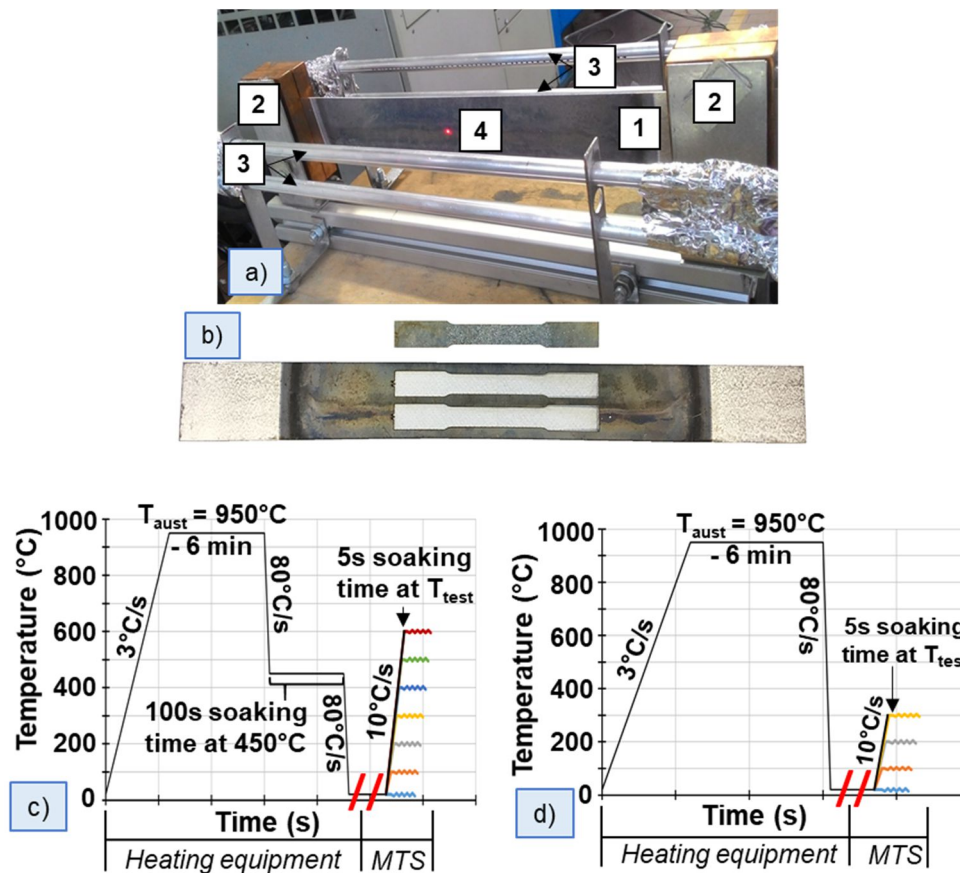


Figure 3.12: a) Equipment for the thermal treatment of the steel stripes and final dog-bone specimens; b) thermal cycle applied for the study of the bainite, and c) the martensite phase.

The thermal cycle applied to obtain the pure bainite phase was calibrated according to the TTT diagram of the 22MnB5 steel grade and the relative saturation curve of the bainite transformation obtained through dilatometric

measurements. The obtained dilatometric data, Figure 3.13(a), shows that after 40 s at  $450(\pm 1\%)$  °C, the austenite is fully transformed into bainite. To assess the effectiveness of the applied thermal cycle, HRC hardness tests were performed along the longitudinal middle plane of the strip. Figure 3.13(c) shows the measured values that are in the range [90, 91] of the typical HRC of the bainite and martensite phases. The temperatures registered by the pyrometers, relative to the bainite phase thermal cycle, and reported in Figure 3.13(b) confirms the hardness measures since the temperature registered followed the set cycle. The initial divergence between the Thermal Cycle 1 (TC1) and the Thermal Cycle 2 and 3 (TC2, TC3) is due to the fact that the heat first start to rise in the centre of the stripe and from there it diffuses along all the length of the stripe. Nevertheless, the target temperature is reached in the needed length of the stripe.

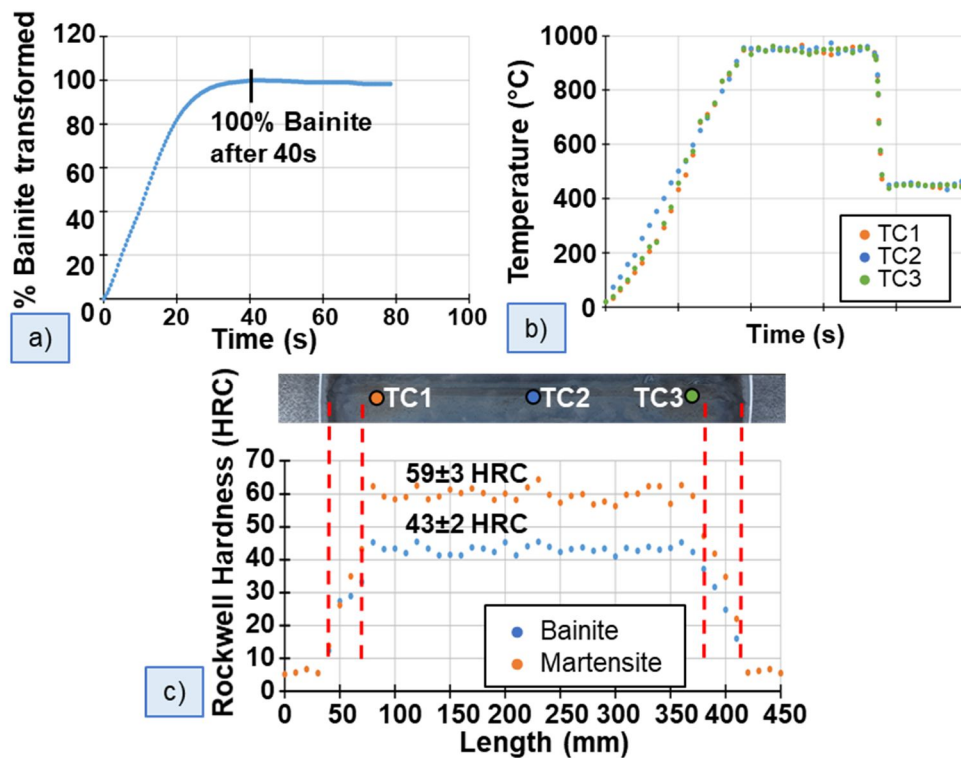
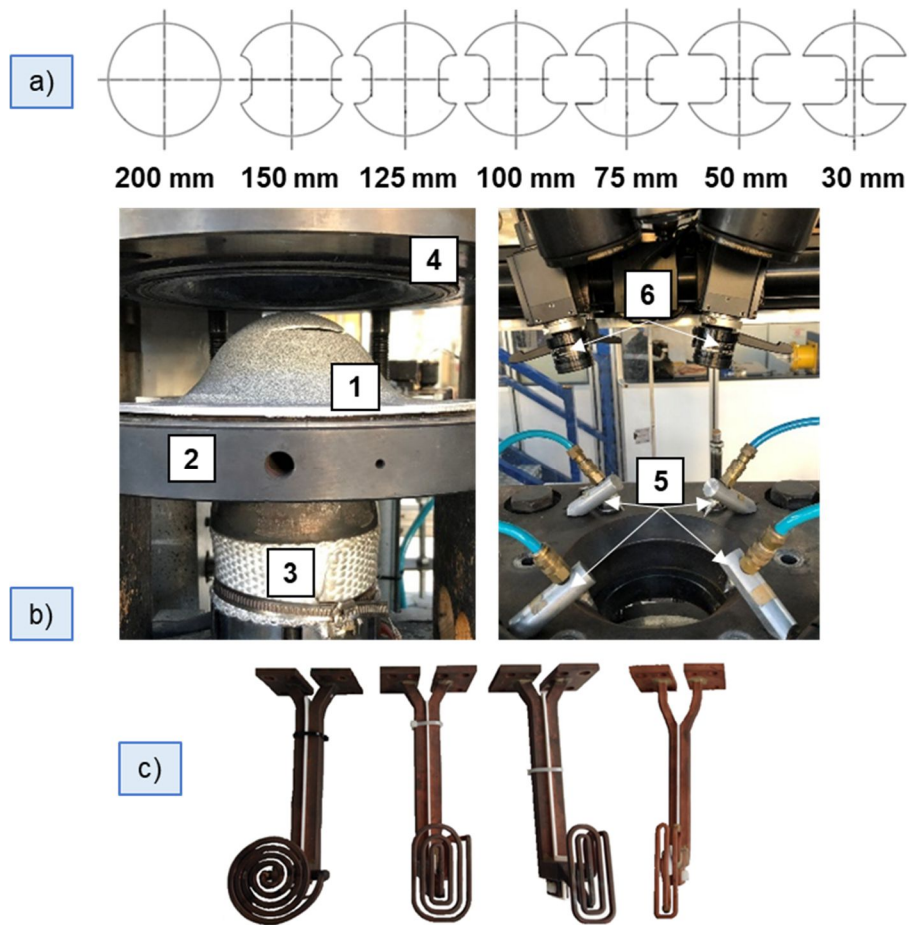


Figure 3.13: a) Curve of the transformation of austenite into bainite; b), thermal cycle registered by the pyrometers and c) Rockwell hardness C of the heat-treated stripes.

### 3.4 Equipment and procedures for Nakajima tests

The hot Nakajima tests were performed on  $1.50(\pm 0.05)$  mm thick and  $1.20(\pm 0.05)$  mm thick 22MnB5 sheets. Seven geometries were considered

according to the ISO 12004-2-2008 standard. Figure 3.14(a) shows the specimens geometry, namely the 30 mm width, to reproduce the uniaxial stress state, the 100 mm width, for the plane stress state, the 200 mm width, for the axisymmetric stress state, and the intermediate geometries, namely 50 mm, 75 mm, 125 mm and 150mm. Figure 3.14(b) shows the experimental apparatus used for the hot Nakajima tests. The specimen (1) is fixed between the die (4) and the blank holder (2). The punch (3), equipped with electrical cartridge heaters that allows heating it up to the maximum temperature of  $950(\pm 15)$  °C, is pre-heated at the same temperature at which the test takes place to ensure the specimen deformation under isothermal conditions. For the purposes of this investigation and according to ISO standard [46], the punch was kept at the same temperature of the specimen. The blank is heated thanks to an inductor head, mounted on a pneumatic system which allows the movement of the copper head both in the horizontal and the vertical directions, to ensure the correct displacement and proper heating of the specimen. Four different inductor heads were used, as shown in Fig. 3.14(c), to avoid the edge effect, which causes the edges of the specimen to be hotter than the centre, creating a preferential area where the fracture initiates. The temperature of the specimen is controlled by a type-K thermocouple spot-welded in different points of the sheet surface, where the deformation occurs. In the same time, the temperature of the punch is controlled by two type-K thermocouples inserted in the punch as close as possible to its hemispherical surface. The correct cooling of the specimen is granted by the use of four air nozzles (5) The strain field in the sheet during deformation was measured using the GOM Aramis™ optical system (6), made of two cameras and equipped with a proper lighting equipment, providing the possibility to display 3D-coordinates of the surface by means of a stochastic pattern previously applied to the sheet metal and capable of resisting high temperature. In order to assure the correct lubrication, a 0.1 mm graphite foil was placed between the punch and the specimen.



*Figure 3.14: a) Specimens used for the hot Nakajima tests, b) Nakajima testing equipment, c) inductor heads used to heat the specimen during the test.*

The two cameras placed above the specimen film the experimental tests and the software Aramis<sup>TM</sup> convert the frames in a 3D image of the specimen, where the maps of the major and minor strain can be visualized. Using a series of parallel sections it is possible to obtain the major and minor strain values that will be inserted in the FLC. Figure 3.15 shows the elaboration steps of Aramis<sup>TM</sup>.

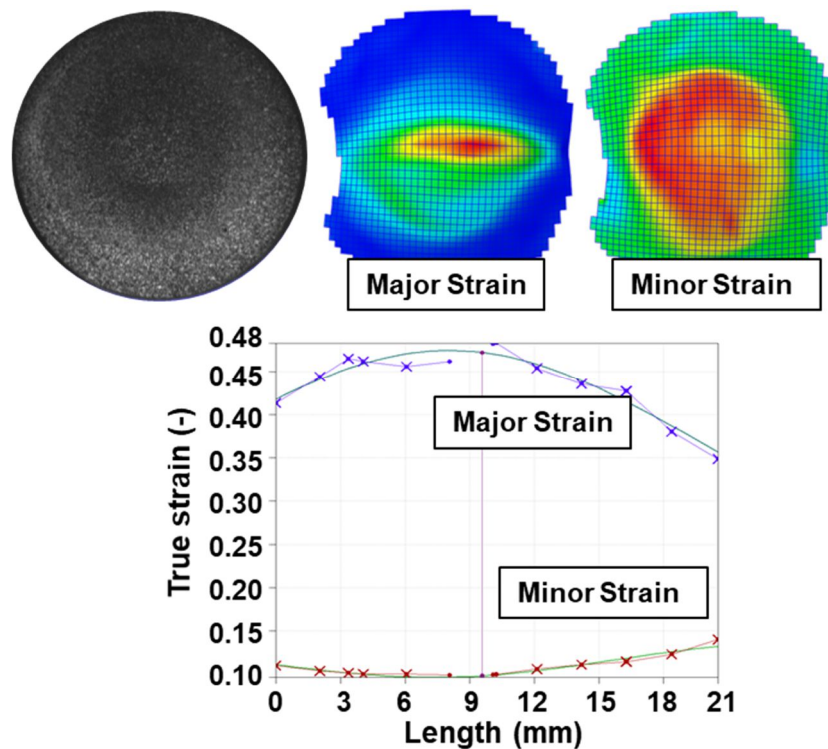


Figure 3.15: Aramis<sup>TM</sup> elaboration and resultant strain plot.

The hot Nakajima tests can be divided into three different experimental campaigns. Depending on the aim of the test, different thermal cycles were applied to the specimen.

### 3.4.1 Influence of the temperature on the formability

The first experimental campaign was carried out to study the influence of the temperature on the Forming Limit Curve (FLC). This experimental campaign was carried out on the 1.50(±0.05) mm thick 22MnB5 sheets and all seven specimens' geometries were used. Table 3.6 reports the main experimental parameters of the experimental campaign. Figure 3.16(a) shows the thermal cycle applied to the specimens: after the heating at 3(±0.5) °C/s from room temperature to the austenitization temperature 950(±15) °C, the specimen was kept at this temperature for 6 minutes and then cooled down at 30(±0.5) °C/s by means of the air nozzles to the testing temperature; after 10 s at  $T_{\text{test}}$ , the specimen was deformed till fracture. Figure 3.16(b) shows the thermal profile of the specimen recorded by the thermo-camera.

Table 3.6: Experimental plan for the hot Nakajima tests- influence of temperature.

Temperature (°C)	Strain Rate (s <sup>-1</sup> )	Repeatability
500	0.1	5
600		

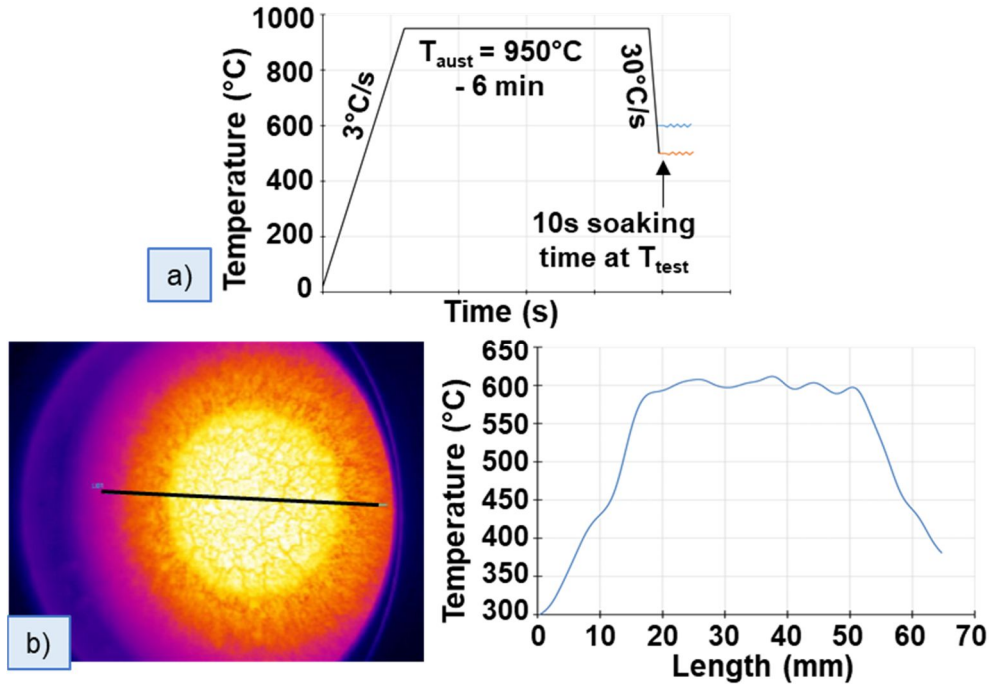


Figure 3.16: a) Thermal cycle applied, b) thermo-camera data.

### 3.4.2 Influence of the microstructure on the formability

This experimental campaign was carried out to study the influence of the microstructure on the Forming Limit Curve (FLC). This experimental campaign was carried out on the 1.50(±0.05) mm thick 22MnB5 sheets and three geometries were used, namely 30 mm, 100 mm and 200 mm. The thermal cycle applied during the tests is shown in Fig. 3.17(a)-(c): after the heating at 3(±0.5) °C/s from room temperature to the austenitization temperature ( $T_{\text{aust}}$ ) 950(±15) °C, the specimen was kept at this temperature for 360 s and then cooled down at 80(±0.5) °C/s, by means of the air nozzles, to 600(±8) °C. To calibrate the soaking time to be set in the different Nakajima test conditions, the TTT curve at 600°C of 22MnB5 had to be obtained, in order to define the correct thermal cycles that have to be applied. The setup used for obtaining the TTT curves was

the same described in §3.2 and Figure 3.2; the specimen was brought to austenitization temperature,  $950(\pm 1)$  °C, with a heating rate of  $3 (\pm 1\%)$  °C/s and the specimen is then kept at that temperature for 6 minutes, in order to allow the complete transformation of the initial ferrite + pearlite mixture into austenite. Thanks to the air nozzle, the specimen is cooled down to  $600(\pm 1)$  °C with a cooling rate of  $100(\pm 1\%)$  °C/s and kept at that temperature for 300s. Three different conditions are tested according to the saturation curve shown in Fig 3.17(d):

1. 100% austenite: after the cooling stage, the specimen is kept at  $600(\pm 8)$  °C for 5 s before the test, as shown in Fig 3.17(a);
2. 50% austenite – 50% bainite: after the cooling stage, the specimen is kept at  $600(\pm 8)$  °C for 30 s before the test, as shown in Fig 3.16(b) and according to the saturation curve shown in Fig 3.17(d);
3. 100% bainite: after the cooling stage, the specimen is kept at  $600(\pm 8)$  °C for 200 seconds before the test, as shown in Fig 3.17(c).

The strain rate selected was  $1\text{s}^{-1}$ ; each geometry was tested 5 times and the FLD points here reported are the mean values. The choice to select three different percentage of austenite and bainite in the specimen stands on the understanding of the differences in the formability when the piece is deformed in pure austenite phase, or when the deformation occurs later when the austenite evolves in a tougher phase, such as bainite.

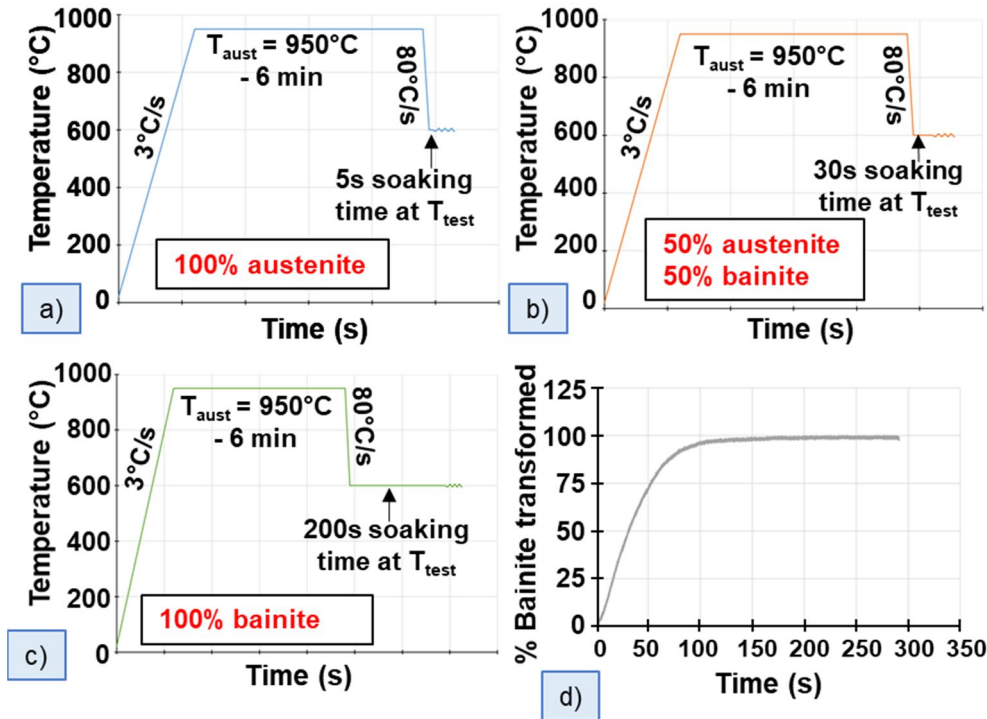


Figure 3.17: Thermal cycles applied for the a) 100% austenite tests, b) 50% austenite-50% bainite tests, c) 100% bainite tests, d) saturation curve at 600°C.

### 3.5 GISSMO damage criterion

The experimental tests performed to obtain the required data for the calibration of the GISSMO damage criterion are divided into hot tensile tests and hot Nakajima tests, all performed with 1.20(±0.05) mm thick specimens.

The specimens used for the tensile tests are shown in Figure 3.18 (a). In order to cover the whole range of the triaxiality values required by the GISSMO model, a series of tensile tests on smooth, notched and shear specimens were performed, according to the experimental plan presented in Table 3.7. The nominal notch radii were chosen equal to 2, 5 and 10 mm, while the shear specimen was designed according to the ASTM B831 standard. The specimens, from an initial ferrite+pearlite microstructure, were brought to the austenitization temperature, namely 950(±1%) °C, for 360 s; then, thanks to the air nozzle (3), the specimen was cooled down to the testing temperature with a cooling rate of 80(±1%) °C/s. After a soaking time of 5(±0.2) s, the specimen was tested till rupture. All the specimens were coated with a stochastic black and white pattern and all the tests were filmed using a CCD camera (5). The frames were then analyzed using GOM

Aramis™, in order to calculate the true strain data. To identify the fracture strain of the shear samples, the following procedure was identified on the basis of [85] and [92]: first, three lines were drawn on the deformation zone of the sample along the horizontal direction, then, after the sample fracture, a lateral image of the fracture area was acquired using a table microscope, aligning the vertical axis of the sample with the horizontal direction of the image later on processed in a CAD software; finally, the angles between the lines that extended from the highlight endpoint and the vertical line were measured and the average angle calculated.

Table 3.7: Experimental plan for the hot tensile tests for the calibration of GISSMO.

Specimen	Temperature (°C)	Strain Rate (s <sup>-1</sup> )	Repeatability
<b>Smooth</b>			
<b>Notch 2 mm</b>	700	1	3
<b>Notch 5 mm</b>			
<b>Notch 10 mm</b>			
<b>Shear</b>			

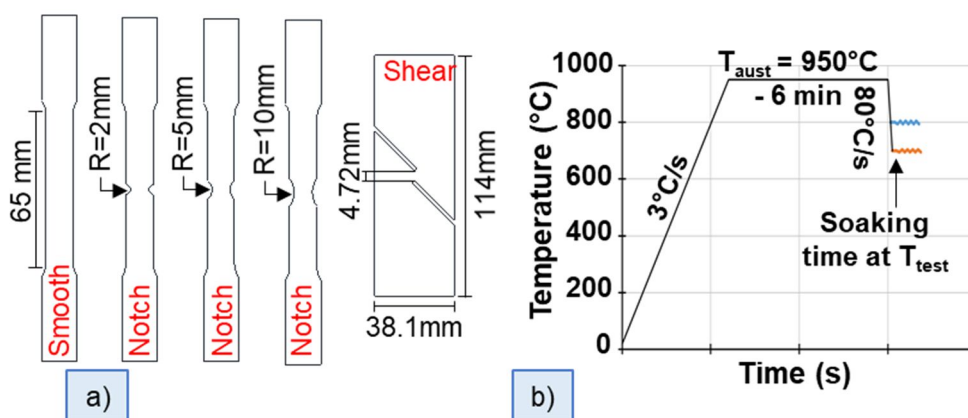


Figure 3.18: a) Specimens used for GISSMO calibration, b) thermal cycle.

The hot Nakajima tests were carried out on two geometries (see Figure 3.14 (a): the 200 mm geometry was necessary to complete the set of tests necessary for the calibration, the 100 mm geometry was necessary for the validation of the model, performed after the calibration. The thermal cycle applied is the same shown in Figure 3.18 and the thickness of the specimens is 1.20(±0.05) mm. The repeatability chosen for the Nakajima tests is 3.



## **CHAPTER 4**

### **Numerical modelling**



This chapter is dedicated to the explanation of all the settings of the numerical simulations run in LS-DYNA code. Three types of numerical simulations were run, namely simulations to reproduce the CCT left-shift, hot tensile test simulation to calibrate the GISSMO damage criterion and hot Nakajima simulations to reproduce the experimental FLCs and to calibrate and validate the GISSMO damage criterion. The description of the numerical simulations start with the presentation of the material models and the thermal models implemented, then the setting of all the simulations run are reported.

## 4.1 Material model

LS-Dyna code offers a wide range of material models to choose from, allowing great freedom to the user. Among all the material models, the chosen one for the whole thesis work is *MAT\_244\_UHS\_STEEL* [93].

*MAT\_244\_UHS\_STEEL* is based on hypo elasticity and the stress rates are given by Hooke's generalised law [94]. The rate  $\dot{\sigma}_{ij}$  is given by:

$$\dot{\sigma}_{ij} = (C_{ijkl} \dot{\varepsilon}_{kl}^e) = C_{ijkl} (\dot{\varepsilon}_{kl} - \dot{\varepsilon}_{kl}^p) + \dot{C}_{ijkl} (\varepsilon_{kl} - \varepsilon_{kl}^p) \quad (4.1)$$

Where  $\varepsilon_{kl}^e$  represents the elastic strain,  $C_{ijkl}$  is the elastic stiffness,  $\varepsilon_{kl}^p$  is the plastic strain and  $\varepsilon_{kl}$  is the total strain. The rate formulation of the elastic stiffness is included due to the optional temperature-time dependency of the Young modulus. In associated plasticity, the plastic flow is orthogonal to the yield surface  $y(\sigma_{ij}, \bar{\varepsilon}_1^p, \dots, \bar{\varepsilon}_5^p) = 0$ . The yield function is expressed as:

$$y = \bar{\sigma} - \sigma_y(\bar{\varepsilon}_1^p, \dots, \bar{\varepsilon}_5^p) \quad (4.2)$$

Where  $\bar{\sigma}$  is the effective stress and  $\sigma_y$  is the total hardening function. In this model with five phases the total hardening function is composed of a mixture of the five phases:

$$\sigma_y = x_1 \sigma_1^y(\bar{\varepsilon}_1^p) + \dots + x_5 \sigma_5^y(\bar{\varepsilon}_5^p) \quad (4.3)$$

Where  $x_i$  is the true volumetric fraction of the phase  $i$  and  $\sigma_i^y$  is the hardening function of the phase  $i$ . If the effective stress reaches the yield stress the material undergoes plastic deformation as an ordinary von Mises material. However, if the effective stress is less than the yield stress and phase transformations have begun, it is still possible to have plastic deformations. These plastic deformations

that occur below the yield stress are due to the transformation induced plasticity (TRIP) [66].

*MAT\_244\_UHS\_STEEL* is mainly suited for hot stamping processes where phase transformations are crucial. It has five phases and it is assumed that the blank is fully austenitized before cooling. The basic constitutive model is based on the work done by Akerstrom [59, 62] and Li [95]. The five different phases are identified in the software with numbers, ranging from 1, which corresponds to austenite, to 5, which corresponds to martensite; ferrite, pearlite and bainite are 2, 3 and 4 respectively. The phase distribution during cooling is calculated by solving the following rate equation for each phase transition:

$$\dot{X}_k = g_k(G, C, T_k, Q_k) f_k(X_k) \quad k = 2, 3, 4 \quad (4.4)$$

Where  $k$  represents the phases, namely ferrite, pearlite and bainite,  $g_k$  is a function dependent on the grain number  $G$ , the chemical composition  $C$ , the temperature  $T$  and the activation energy  $Q$ . Moreover, the function  $f$  is dependent on the actual phase  $X_k = x_k/x_{eq}$ :

$$f_k(X_k) = X_k^{0.4(X_k-1)} (1 - X_k)^{0.4X_k} \quad k = 2, 3, 4 \quad (4.5)$$

The true amount of martensite, i.e.  $k = 5$ , is modelled by using the true amount of the austenite left after the bainite phase:

$$x_5 = x_1 [1 - e^{-\alpha(MS-T)}] \quad (4.6)$$

Where  $x_1$  is the true amount of austenite left for the reaction,  $\alpha$  is a material-dependent constant and  $MS$  is the start temperature of the martensite reaction. The start temperatures are automatically calculated based on the composition (the chemical elements in the following equations represent the nominal weight of the indicated element):

- Ferrite,  $k=2$ :

$$\begin{aligned} FS = & 1185 - 203 \times \sqrt{C} - 15.2 \times Ni + 44.7 \times Si + 104 \times V + 31.5 \times Mo + \\ & + 13.1 \times W - 30 \times Mn - 11 \times Cr - 20 \times Cu + 700 \times P + 400 \times Al + \\ & + 120 \times As + 400 \times Ti \end{aligned} \quad (4.7)$$

- Pearlite,  $k=3$ :

$$PS = 996 - 10.7 \times Mn - 16.9 \times Ni + 29 \times Si + 16.9 \times Cr +$$

$$+290 \times As + 6.4 \times W \quad (4.8)$$

- Bainite, k=4:

$$BS = 910 - 58 \times C - 35 \times Mn - 15 \times Ni - 34 \times Cr - 41 \times Mo \quad (4.9)$$

- Martensite, k=5:

$$MS = 812 - 423 \times C - 30.4 \times Mn - 17.7 \times Ni - 12.1 \times Cr - 7.5 \times Mo + \\ + 10 \times Co - 7.5 \times Si \quad (4.10)$$

LS-DYNA card for this material is shown in Figure 4.1. The material model requires a series of data regarding the material, along with a series of crucial settings:

- RO, E, PR: density, elastic modulus and Poisson's ratio respectively;
- TUNIT: Number of time units per hour. Default is seconds that is 3600 time units per hour. It is used only for hardness calculations;
- CRSH: with the CRSH = 1 option it is now possible to transfer the material properties from a hot stamping simulation (CRSH = 0) into another simulation. The CRSH = 1 option reads a file from a simulation with CRSH = 0 and keeps all the history variables (austenite, ferrite, pearlite, bainite, martensite, etc) constant. This will allow steels with inhomogeneous strength to be analysed in, for example, a crash simulation;
- PHASE: switch to include or exclude middle phases from the simulation;
- HEAT: when HEAT is activated the re-austenitization and grain growth algorithms are also activated. The software can exclude heating (HEAT=0), allow only heating (HEAT=1) or switch between cooling and heating (HEAT=2). If this parameter is equal to 1 or 2, new flags are activated, namely:
  - AUST, FERR, PEAR, BAIN, MART: these parameters allow the user to insert a defined amount of each phase in the blank at the beginning of the simulation and the sum of the inserted quantities has to be equal to 1;

- GRK: growth parameter;
- GRQR: grain growth activation energy divided by the universal gas constant;
- TAU1, TAU2: Empirical grain growth parameter  $c_1$ , and  $c_2$  describing the function  $\tau(T)$ ;
- GRA, GRB: grain growth parameters  $A$  and  $B$ ;
- EXPA, EXPB: grain growth parameters  $a$  and  $b$ ;
- GRCC, GRCM; grain growth parameter with the concentration of non-metals in the blank, weight% of C or N (GRCC) or grain growth parameter with the concentration of metals in the blank, lowest weight% of Cr, V, Nb, Ti, Al (GRCM);
- HEATN: Grain growth parameter  $n$  for the austenite formation;

The grain growth is activated when the temperature exceeds a threshold value that is given by:

$$T = \frac{B}{A - \log_{10}[(GRCM)^a(GRCC)^b]} \quad (4.11)$$

And the rate equation for the grain growth is

$$\dot{g} = \frac{k}{2g} e^{-Q/RT} \quad (4.12)$$

The rate equation for the phase re-austenitization is given in Oddy [96]:

$$\dot{x}_a = n \left[ \ln \left( \frac{x_{eu}}{x_{eu} - x_a} \right) \right]^{n-1/n} \left[ \frac{x_{eu} - x_a}{\tau(T)} \right] \quad (4.13)$$

Where  $n$  is the parameter HEATN. The temperature-dependent function ( $T$ ) is given from Oddy [96] as  $(T) = c_1(T - Ts)c_2$ . The empirical parameters  $c_1$  and  $c_2$  are calibrated in Oddy to  $2.06 \times 10^8$  and 4.806 respectively;

- LCYi: material's flow curves for the different phases, where 1 is austenite, 2 is ferrite, 3 is pearlite, 4 is bainite and 5 is martensite;

- B, C, Co, Mo, Cr, Ni, Mn, Si, V, W, Cu, P, Al, As, Ti: chemical composition of the steel, represented by the weight percentages of all the element here listed; in all the numerical simulations run, the percentage of the various element was set according to [59], and here reported in Table 4.1.

*Table 4.1: Nominal composition of 22MnB5 by Akerstrom [59].*

<b>Element</b>	<b>Weight %</b>
<b>B</b>	0.003
<b>C</b>	0.23
<b>Cr</b>	0.211
<b>Mn</b>	1.25
<b>Si</b>	0.29
<b>P</b>	0.013
<b>S</b>	0.001

- KFER, KPER: correction factors for boron in the ferrite and pearlite, respectively, reactions;
- LCTRE: curve for transformation induced strains;
- THEXP1, THEXP5 or LCTH1, LCTH5, TABTH: coefficient (THEXPi), or curve (LCTHi), or table (TABTH) of thermal expansion in austenite and martensite, respectively;
- LAT1, LAT5: latent heat for the decomposition of austenite into ferrite, pearlite and bainite (i=1), or of austenite into martensite (i=5);
- QR2, QR3, QR4: activation energy divided by the universal gas constant for the diffusion reaction of the austenite-ferrite, austenite-pearlite, austenite-bainite reactions respectively;
- ALPHA: material constant for the martensite phase. A value of 0.011 means that 90% of the available austenite is transformed into martensite at 210 degrees below the martensite start temperature, whereas a value of 0.033 means a 99.9% transformation;
- GRAIN: ASTM grain size number for austenite, usually a number between 7 and 11;

- TOFFE, TOFPE, TOFBA: number of degrees that the ferrite is bleeding over into the pearlite reaction, that the pearlite is bleeding over into the bainite reaction or that the bainite is bleeding over into the martensite reaction, respectively;
- PLMEMi: memory coefficient for the plastic strain that is carried over from the austenite. A value of 1 means that all plastic strains from austenite is transferred to the ferrite phase (i=2), or to the pearlite phase (i=3), or to the bainite phase (i=4), or to the martensite phase (i=5); a value of 0 means that nothing is transferred;
- STRC, STRP: effective strain rate parameters  $C$  and  $P$ ;
- REACT: flag for advanced reaction kinetics input, if it is equal to 1, new parameters are activated, namely:
  - FS, PS, BS, MS: manual start temperature for ferrite, pearlite, bainite and martensite respectively;
  - MSIG: describes the increase of martensite start temperature for cooling due to applied stress;
  - LCEPS23, LCEPS4: curve with plastic strain in abscissa that scales the activation energy QR2, QR3 or QR4:
 
$$QR_i = Q_i \times LCEPS(\varepsilon_{pl})/R \quad (4.14)$$
  - LCEPS5: curve which describes the increase of the martensite start temperature for cooling as a function of plastic strain:
 
$$MS^* = MS + MSIG \times \sigma_{eff} + LCEPS5(\varepsilon_{pl}) \quad (4.15)$$
- CWM and TEMPER: flag for computational welding mechanics input and for tempering input, respectively. Both parameters activate new flags, but in this research work, neither of these flags were activated.

*MAT_UHS_STEEL_(TITLE) (244) (0)							
TITLE							
MID	RO	E	PR	TUNIT	CRSH	PHASE	HEAT
					0	0	2
LCY1	LCY2	LCY3	LCY4	LCY5	KFER	KPER	B
					0.0	0.0	0.0
C	Co	Mo	Cr	Ni	Mn	Si	V
0.0	0.0	0.0	0.0	0.0	0.0	0.0	0.0
W	Cu	P	Al	As	Ti	CWM	LCTRE
						0	
THEXP1	THEXP5	LCTH1	LCTH5	TREF	LAT1	LAT5	TABTH
				273.15			
QR2	QR3	QR4	ALPHA	GRAIN	TOFFE	TOFPE	TOFBA
0.0	0.0	0.0	0.0	0.0	0.0	0.0	0.0
PLMEM2	PLMEM3	PLMEM4	PLMEM5	STRC	STRP	REACT	TEMPER
						1	0
AUST	FERR	PEAR	BAIN	MART	GRK	GROR	TAU1
0.0	0.0	0.0	0.0	0.0	0.0	0.0	2.08E+8
GRA	GRB	EXPA	EXPB	GRCC	GRCM	HEATN	TAU2
3.11	7520.	1.0	1.0			1.0	4.806
FS	PS	BS	MS	MSIG	LCEPS23	LCEPS4	LCEPS5
0.0	0.0	0.0	0.0				

Figure 4.1: MAT\_244\_UHS\_STEEL card in LS\_DYNA code.

The potential of this material is very high, but the number of parameters that have to be inserted is not negligible. This material model was used for all the simulations run in this work.

## 4.2 CCT left-shift simulations

The first set of simulations run for this work regards the calibration of the parameters LCEPS4 and LCEPS5 to reproduce the left-shift of the CCT that regards the martensite and the bainite phases. To this aim, a series of explicit thermo-mechanical simulations were set. The geometry implemented is the one of the tensile specimen, shown in Figure 3.3, and it was implemented as a shell element with a thickness of 1.2 mm. The strain rate and the temperature implemented in the simulations were the same used in the experimental tests. LS-DYNA offers a wide choice of shell elements and, among all of them, the shell element number -16, fully integrated shell element (Belytschko - Won - Chiang),

was chosen. The number of integration points in the thickness can be chosen by the user and, for these simulations, it was set to 5. The mesh size was chosen equal to 2 mm, but with the CONTROL\_ADAPTIVE card active, so the re-meshing of the specimen during the simulation is allowed. The temperature is implemented using the BOUNDARY\_TEMPERATURE\_SET card, which allows the correlation of a specific set of nodes with a defined temperature, implemented as a constant value or a time-temperature curve. For this case, a time-temperature curve was used, describing the thermal profile shown in Figure 3.4 (b). To correctly represent the cooling stage of the thermal cycle, the card BOUNDARY\_CONVECTION\_SET was used, in order to simulate the air flux of the nozzle during cooling, inserting the heat transfer coefficient with air ranging from 100 W/m<sup>2</sup>K to 520 W/m<sup>2</sup>K. Figure 4.2 describes the specimen used and the defined mesh, with the temperature distribution map visualized and compared with the experimental thermo-camera data.

A series of simulations describing different cooling rates, see Table 3.2, were run, and the percentage of the different phases were recorded to draw a new CCT curve that was compared with the experimental one. The point of the starting transformation was taken when the new phase percentage was equal to 0.1% and the end of the phase transformation was taken when the plateau was reached. The parameters LCEPS4 and LCEPS5 of MAT\_244 were calibrated comparing the experimental and the numerical results, in order to adjust the scale factor of QR4 parameter and obtain the correct shift. The initial QR4 was set equal to 10290 K, according to the data provided by Ford.

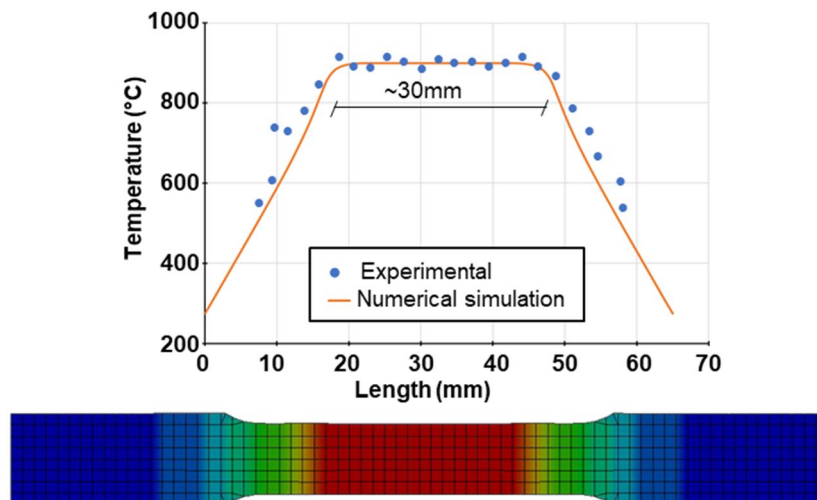


Figure 4.2: Implemented temperature profile compared with the experimental data.

### 4.3 Nakajima tests simulations

The second series of numerical simulations regarded the dependency of the microstructural phase on the resultant FLC, so a series of explicit thermo-mechanical simulations of the Nakajima test were set to confirm the experimental data. As in the experimental tests, three geometries were considered, namely the 30 mm, 100 mm and the 200 mm specimens, here reported in Figure 4.3 with the initial mesh of 2 mm and the temperature profile map highlighted and compared with the data obtained through the thermo-camera analysis. The temperature was implemented as a time-temperature curve, linked to specific nodes of the specimen thanks to the BOUNDARY\_TEMPERATURE\_SET card. Again, to correctly represent the cooling stage of the thermal cycle, the card BOUNDARY\_CONVECTION\_SET was used, in order to simulate the air flux of the nozzle during cooling. The strain rate and the temperature implemented in the simulations were the same used in the experimental tests.

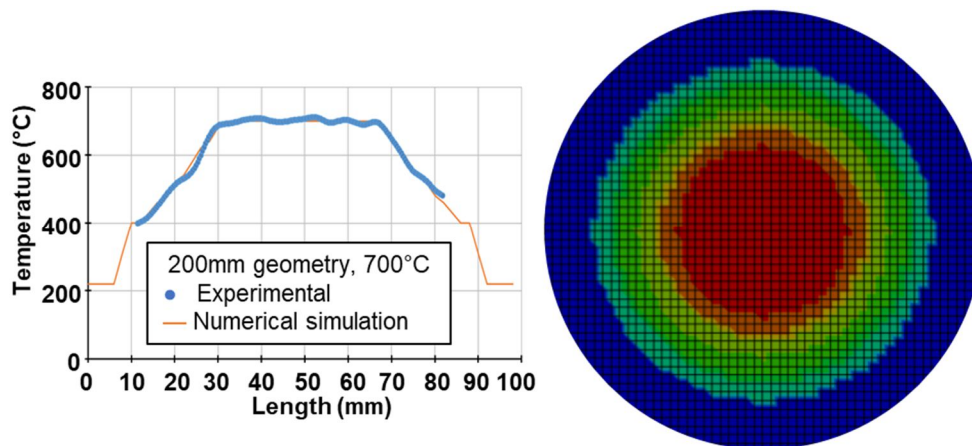
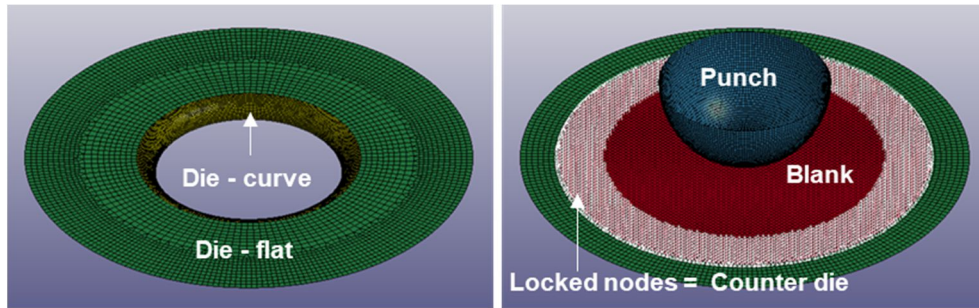


Figure 4.3: Implemented specimens' geometries and temperature profiles comparison.

Like in the simulations of the CCT left-shift, the CONTROL\_ADAPTIVE card was activated, allowing the re-meshing of the specimen during the deformation. The shell element used was still number -16, and the thickness was set to 1.5 mm, with 5 integration points in the thickness. Figure 4.4 shows the basic setting of the geometries in the simulation, with the punch and the die simulated as rigid bodies, while the specimen simulated as the deformable part. Both the punch and the curved area of the die were simulated using a very fine mesh, in order to avoid edges due to a coarse mesh that cannot follow the geometry. The punch temperature was set constant at 600°C and the die

temperature to 120°C, since in the experimental tests the punch is brought at the same temperature of the specimen to perform the tests in isothermal conditions, and the data of the thermo-camera revealed that the die reaches the temperature of 120°C due to thermal exchange. The counter die is not simulated as a part, but, instead, the nodes at the edge of the specimen, which should have been under the load of the blank holder, are blocked and no movement is allowed.



*Figure 4.4: Nakajima simulation tools and geometries setting.*

In these simulations, it is very important to implement the thermal parameters and the friction coefficients very accurately, since both can affect the final results. The thermal parameters can be added using the card `MAT_T01_THERMAL_ISOTROPIC`, which allows the implementation of different parameters, such as HC, specific heat, and TC, thermal conductivity, relative to the part of the simulation linked with the thermal material. For this set of simulations, HC was set equal to 741 J/KgK and TC was set equal to 34 W/mK. The data relative to the contact between the specimen and the tools, namely the die and the punch, is defined using the `CONTACT_FORMING_ONE_WAY_SURFACE_TO_SURFACE_THERMAL` card. In this card, the friction coefficients, both static, FS, and dynamic, FD, are defined as a constant value or with a curve defined as velocity vs friction, or temperature vs friction or pressure vs friction. In this case, the friction between the specimen and the punch was set according to the characteristic of the graphite foil used in the experimental test, so FS was set equal to 0.1 and FD equal to 0.06. In this card, the heat transfer coefficient, HTC, between the punch and the specimen is defined and set equal to 200 W/m<sup>2</sup>K.

## 4.4 GISSMO damage criterion simulations

The third set of simulations regarded the calibration and validation of the GISSMO damage criterion. To this aim a series of explicit-thermo-mechanical simulations were set. The tensile tests simulations were set using the same geometries, strain rate and temperatures of the experimental tests, and, to be sure that the mesh accurately reproduce the notched specimens and the shear specimen, a mesh equal to 1 mm was set and the central area of the specimen was meshed with a size of 0.5 mm. The thickness of the shell was set equal to 1.2 mm and 5 integration points on the section were set. The temperature was implemented in the same way already described, so with a time-temperature curve linked to specific nodes of the specimen. The setting of the Nakajima tests was the same described in §4.4 and the geometries considered were the 200 mm specimen for the calibration of the model and the 100 mm specimen for the validation of the model. The strain rate and the temperature implemented in the simulations were the same used in the experimental tests. The simulations run for this section were divided in three steps:

1. Simulation of the tensile and Nakajima tests without the fracture criterion to determine the values of the triaxiality of each geometry tested and determine the influence of the temperature on it;
2. Calibration of the GISSMO damage criterion using the simulations of tensile tests and Nakajima tests of the 200 mm specimen;
3. Validation of the GISSMO damage criterion using the simulation of the Nakajima tests of the 100 mm specimen.

LS-DYNA code allows the implementation of the GISSMO damage criterion using the card `MAT_ADD_EROSION`, Figure 4.5. To calibrate the model, it is required to correlate stress triaxiality to the values of the strain at fracture,  $\epsilon_f$ , and to the values of instability strain,  $\epsilon_{inst}$ , and these two curves represent the flags `LCSDG` and `ECRIT` respectively. Along with these parameters, the values of the damage exponent,  $n$ , and the fading exponent,  $m$ , have to be defined, which are inserted in the material card with the flags `DMGEXP` and `FADEXP` respectively. The flag `IDAM` is necessary to indicate to the software the damage criterion, which, in this case, was set to the GISSMO (flag =1), and `DMGTYP` was set equal to 1, which means that elements will be deleted if  $D \geq 1$ .

*MAT_ADD_EROSION_(TITLE) (000) (0)							
TITLE							
MID	EXCL	MXPRES	MNEPS	EFFEPS	VOLEPS	NUMFIP	NCS
		0.0	0.0	0.0	0.0	1.0	1.0
MNPRES	SIGP1	SIGVM	MXEPS	EPSSH	SIGTH	IMPULSE	FAILTM
IDAM	DMGTYP	LCSDBG	ECRIT	DMGEXP	DCRIT	FADEXP	LCREGD
LCFLD		EPSTHIN	ENGCRT	RADCRT			
		0.0	0.0	0.0			

Figure 4.5: MAT\_ADD\_EROSION card.

The parameters  $n$  and  $m$  can be obtained thanks to LS\_OPT, optimization software on the basis of the Sequential Response Surface Method (SRSM) [97, 98], whose procedure consists in varying the two exponents until the mismatch between the experimental and computed force vs. displacement curves is small enough [86]. Figure 4.6 shows the flow chart of how the LS\_OPT software is able to calculate the parameters.

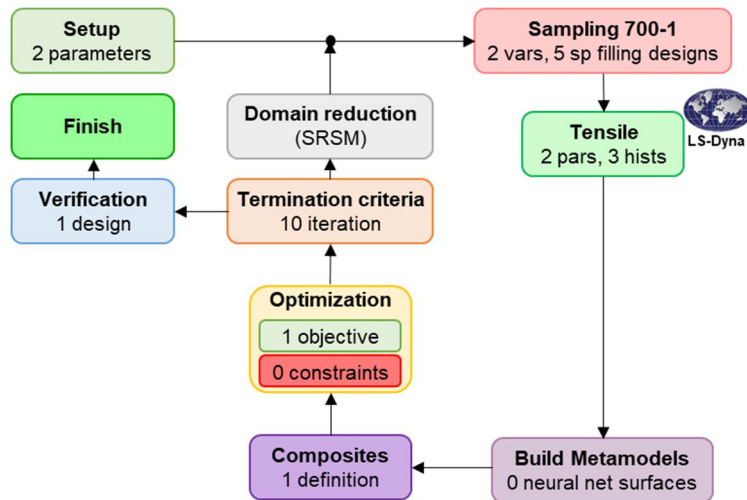


Figure 4.6: Flow chart of the LS\_OPT calculations.

Along with this series of cards and parameters, the card MAT\_NONLOCAL. In nonlocal failure theories, the failure criterion depends on the state of the material within a radius of influence which surrounds the integration point. An advantage of nonlocal failure is that mesh size sensitivity on failure is greatly reduced leading to results which converge to a unique solution as the mesh is refined. Without a nonlocal criterion, strains will tend to localize randomly with

mesh refinement leading to results which can change significantly from mesh to mesh. The nonlocal failure treatment represents a great help in predicting the onset and the evolution of material failure.

## 4.5 Explicit simulations settings

The simulations ran for the present work were all set as explicit simulations. In order to maintain the simulations meaningful and in the usual range of the explicit model, a scaling factor equal to 1000 was inserted, which means that 1 s is converted in 0.001 s in the simulation. For this reason, the time-dependant data implemented have to be adapted.

- *Stress-strain curves*: the set of curves are implemented in this way:
  - The curves are implemented using *DEFINE\_CURVE* card, with strain in abscissa and stress in ordinate;
  - The curves relative to the same temperature, but with different strain rates are collected together using *DEFINE\_TABLE\_2D* card, where in abscissa the strain rate is defined and the number of the correspondent curve in ordinate. At this step, the flag *SFA*, scale factor for the abscissa, was set equal to 1000, in order to rescale the strain rate;
  - The Tables 2D were then united in a single Table 3D (*DEFINE\_TABLE\_3D*) where in abscissa the temperatures of the tests are inserted, and in ordinate the number of the correspondent Tables 2D were inserted; in this way, the curves inserted at the beginning are linked to a specific temperature and strain rate.
- *Velocity of the moving nodes*: the scale factor can be inserted both in the values of the curve, or in the flags *SFA* or *SFO* (scale factor value for the abscissa or the ordinate) of the *DEFINE\_CURVE* card, or in the *SF* flag of *BOUNDARY\_PRESCRIBED\_MOTION* card, which describes the direction of the motion.
- *Thermal parameters*: the rescaling of the thermal parameters can be done rescaling manually the time-dependent variables, or, in the

*CONTROL\_THERMAL\_SOLVER* card there is the parameter TSF (Thermal Speedup Factor): this factor multiplies all thermal parameters with units of time in the denominator (e.g., thermal conductivity, convection heat transfer coefficients). It is used to artificially time scale the problem. Its main use is in metal stamping. If the velocity of the stamping punch is artificially increased by 1000, then set  $TSF = 1000$  to scale the thermal parameters.

- *MAT\_244*: in this material model, specifically for the calculation of hardness, the flag TUNIT, which represent the number of time units per hour, can be scaled. The default is seconds that is 3600 time units per hour.

## **CHAPTER 5**

### **Results and discussion**



The aim of this Chapter is to present the results obtained during the three-year work and discuss every aspect in detail to describe the behaviour of the material.

## 5.1 Phase transformation kinetics

The first set of tests regarded the collection of data to draw the CCT curve of 22MnB5. These data are necessary to draw all the thermal cycles for the following tests.

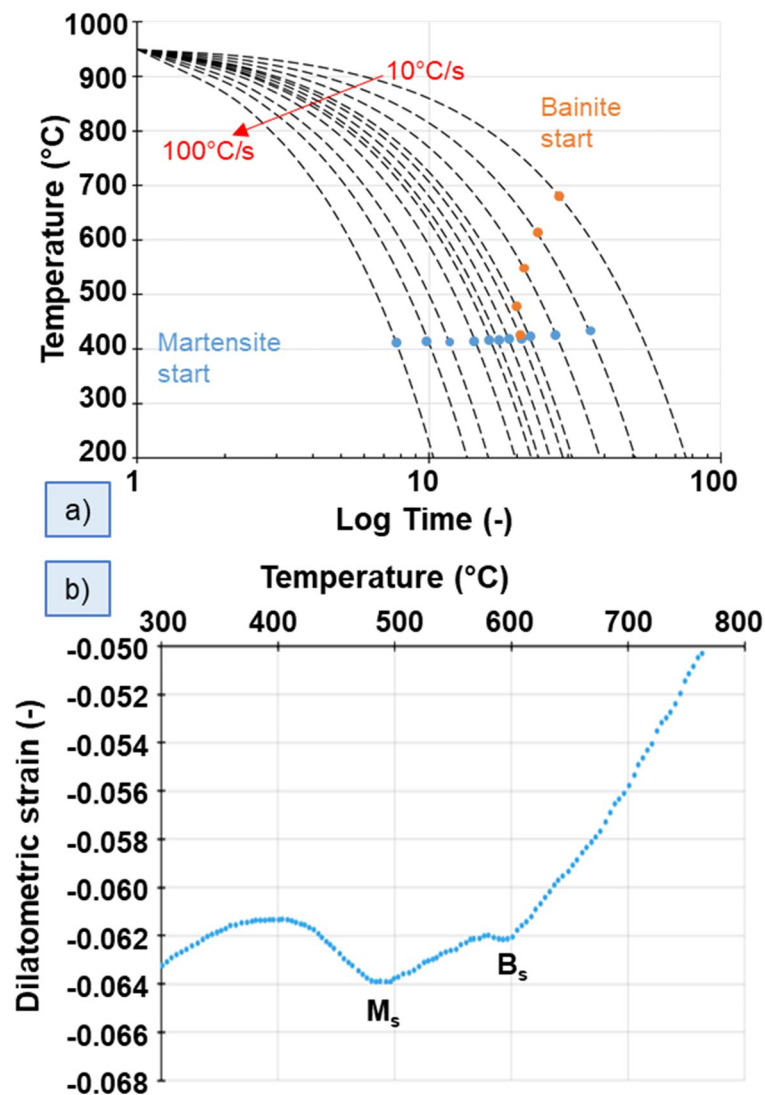


Figure 5.1: a) Experimental CCT diagram of 22MnB5 steel, b) dilatometric curve to detect the CCT points, 20°C/s cooling rate.

Figure 5.1 (a) describes the CCT curve, considering the cooling rates listed in Table 3.2. The points in the CCT curves are obtained analysing the dilatometric curves, like the one shown in Figure 5.1 (b) as an example. The first cooling rate to obtain bainite is 27°C/s and the transformation of austenite into bainite is complete if the specimen is cooled down to room temperature with a cooling rate of 10°C/s.

The studies conducted by Barcellona and Nikravesh [32, 33] state that an applied strain brings modifications to the CCT curve, so the second experimental campaign was carried on to confirm these results and better understand the behaviour of the material in the conditions of the hot stamping process. Table 3.2 reports the experimental campaign followed, but, due to the fact that particular combinations of temperature, strain rate and % strain causes unwanted necking on the specimen, the new experimental plan is here presented in Table 5.1. The necking has to be avoided, since the dilatometer which is placed in contact with the edges of the specimen, slips and fails the measurement. Figures 5.2-5.7 show the results of the experimental tests showing the CCT left-shift due to applied pre-strain. It is evident that the higher the pre-strain, the more shifted is the bainite or martensite start. This influences the design of the dies used in the forming-quenching stage of the hot stamping process, since the amount of heat that has to be removed from the cooling blank is higher than in the un-strained condition. This aspect is very important and has to be taken into account in the numerical simulations. In §5.6.1 the results of the numerical simulations of the CCT left shift are presented.

*Table 5.1: new experimental plan for the study of the CCT left-shift.*

<b>Temperature (°C)</b>	<b>Pre-strain (%)</b>	<b>Strain rate (s<sup>-1</sup>)</b>
<b>700</b>	5, 10, 15	0.1
	5, 10	1
<b>800</b>	5, 10, 15, 20	0.1
	5, 10	1

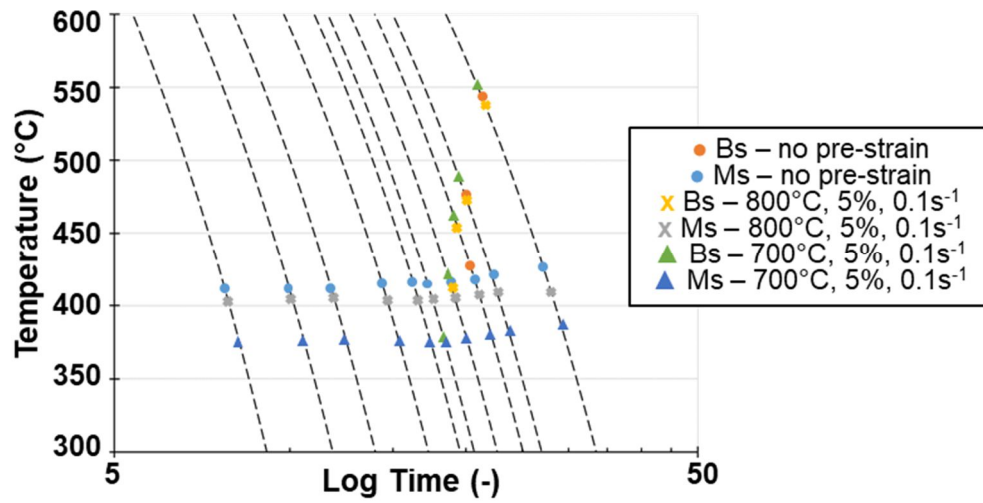


Figure 5.2: CCT left-shift, 5% pre-strain applied at 800°C and 700°C, with strain rate  $0.1 \text{ s}^{-1}$ .

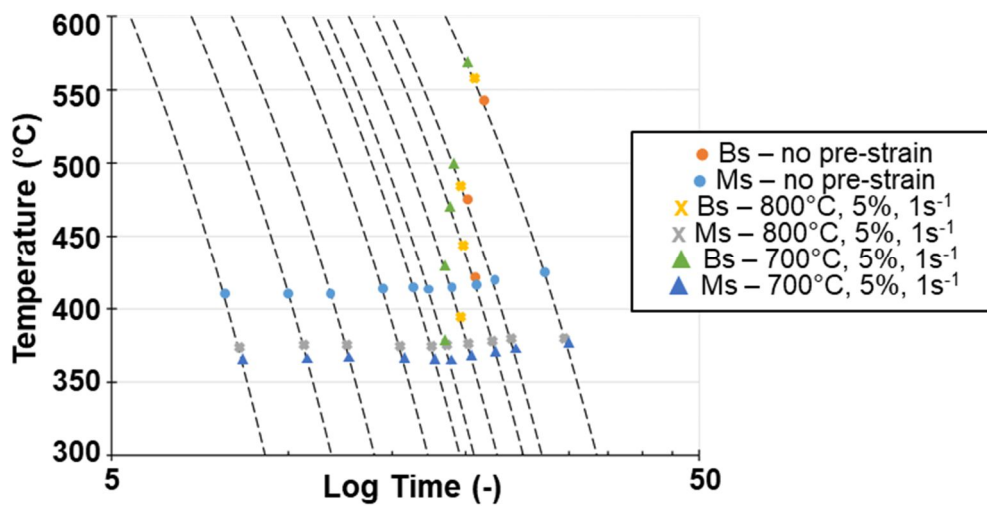


Figure 5.3: CCT left-shift, 5% pre-strain applied at 800°C and 700°C, with strain rate  $1 \text{ s}^{-1}$ .

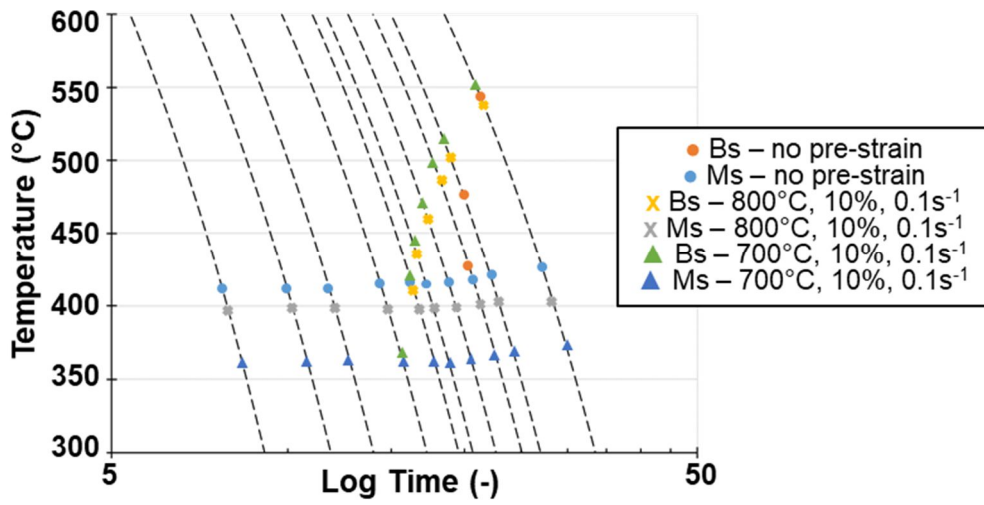


Figure 5.4: CCT left-shift, 10% pre-strain applied at 800°C and 700°C, with strain rate  $0.1 \text{ s}^{-1}$ .

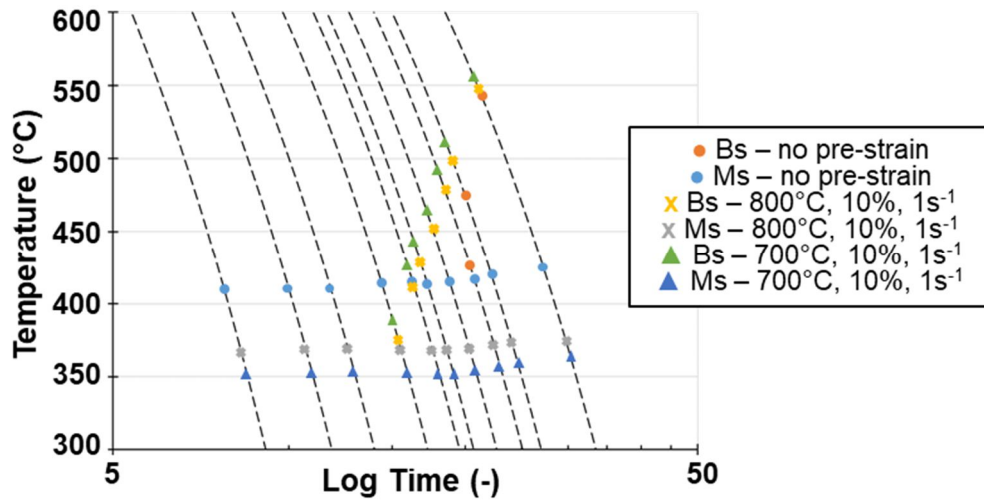


Figure 5.5: CCT left-shift, 10% pre-strain applied at 800°C and 700°C, with strain rate  $1 \text{ s}^{-1}$ .

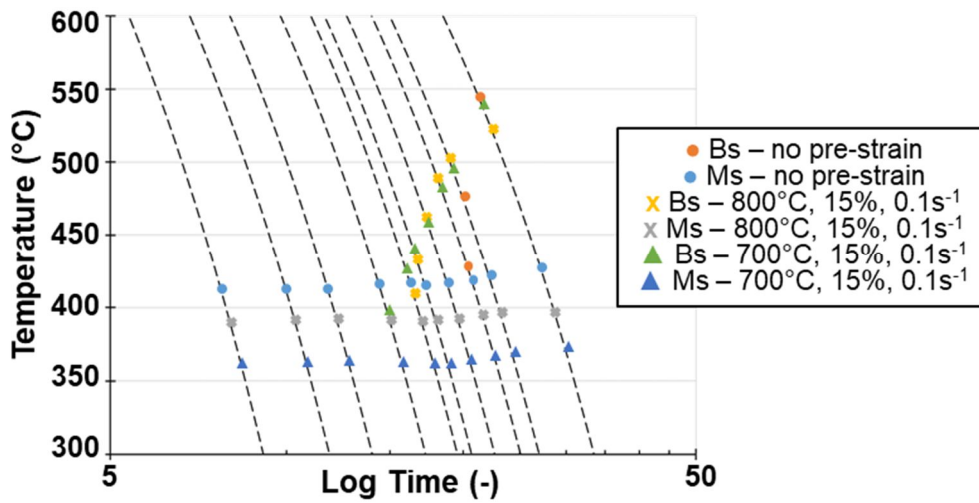


Figure 5.6: CCT left-shift, 15% pre-strain applied at 800°C and 700°C, with strain rate  $0.1 \text{ s}^{-1}$ .

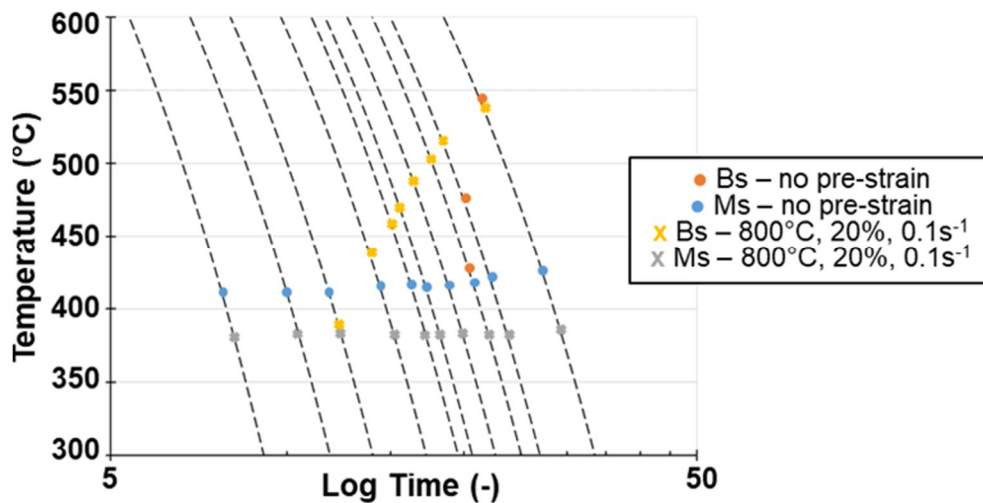


Figure 5.7: CCT left-shift, 20% pre-strain applied at 800°C, with strain rate  $0.1 \text{ s}^{-1}$ .

## 5.2 Study of 22MnB5 rheology

### 5.2.1 Preliminary studies on Austenite phase

After having obtained the data regarding the CCT curves of 22MnB5, a series of preliminary tests aimed to investigate the influence of the different parameters, namely the (i) process temperature and the (ii) strain rate, on the flow stress curves were performed. During the hot stamping process, the usual cooling rate after austenitization is between  $27^\circ\text{C/s}$  and  $35^\circ\text{C/s}$ , but, in respect with the CCT

curve, that range of cooling rates is very close to the bainitic nose, which represents the start of the evolution of austenite into bainite. The bainite phase is tougher than the austenite phase and this difference can lead to substantial modifications to the material behaviour. Figure 5.8 shows the true stress- true strain curves obtained tensile testing the specimens with a strain rate of  $0.01 \text{ s}^{-1}$  at three different testing temperatures, namely  $500^\circ\text{C}$ ,  $550^\circ\text{C}$  and  $600^\circ\text{C}$ , following the thermal cycle shown in Figure 3.9 (§3.3.1). As indicated in the graph, the curves show a flex which causes an evident increase of the true stress.

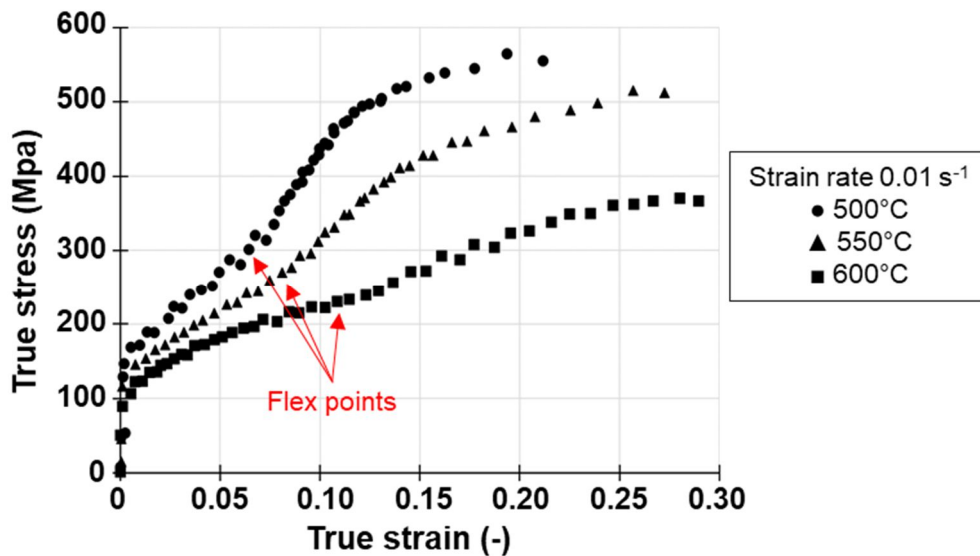


Figure 5.8: Flow curves sensitivity to the temperature at constant strain rate.

The same behaviour can be found tensile testing the specimens at a constant testing temperature of  $550^\circ\text{C}$ , but varying the strain rate, as shown in Figure 5.9. Also in this case, three different flex points can be found in the curves.

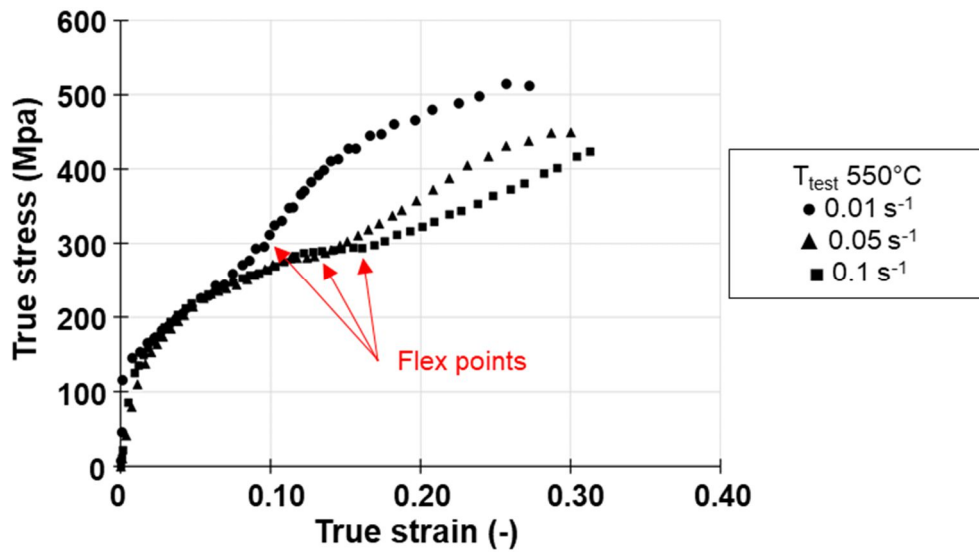


Figure 5.9: Flow curves sensitivity to the strain rate at constant testing temperature.

Analysing in detail the thermal cycles applied and comparing them with the CCT diagram of steel, it can be seen that the curve representing the cooling rate applied in these tests,  $35^{\circ}\text{C/s}$ , in the range of temperatures considered,  $500^{\circ}\text{C}$ - $600^{\circ}\text{C}$ , is very close to the bainitic nose, which is the start of the austenite transformation into bainite.

Table 5.2 reports the values of strain at which the flexes stand in the curves converted in values of time, since the strain rate and the gauge length are both known, and the values of time at which the tests ended, converted in estimated percentage of bainite. Comparing the values of time, with the CCT curve, Figure 5.10, it can be seen that the flex points, which are the change in slopes of the flow curves, represent the start of the phase transformation of austenite into bainite. The slower the test, i. e. the lower the strain rate, the more time is available for the transformation of austenite into bainite, the more evident is the increase in the slope. The percentage of bainite is calculated considering the saturation curves of the transformation of austenite into bainite at  $500^{\circ}\text{C}$ ,  $550^{\circ}\text{C}$  and  $600^{\circ}\text{C}$ , Figure 5.11, considering the time between the flex point and the fracture.

Table 5.2: data of strain, time and estimated % of bainite.

Test conditions		Flex		Fracture		
		Strain (-)	Time (s)	Strain (-)	Time (s)	% Bai
0.01 s <sup>-1</sup>	500°C	0.060	6.183	0.212	23.614	48.4
	550°C	0.086	8.980	0.272	31.259	46.4
	600°C	0.102	10.74	0.289	33.509	37.9
550 °C	0.01 s <sup>-1</sup>	0.086	8.980	0.272	31.259	46.4
	0.05 s <sup>-1</sup>	0.136	2.913	0.300	6.997	8.51
	0.1 s <sup>-1</sup>	0.169	1.841	0.313	3.675	3.82

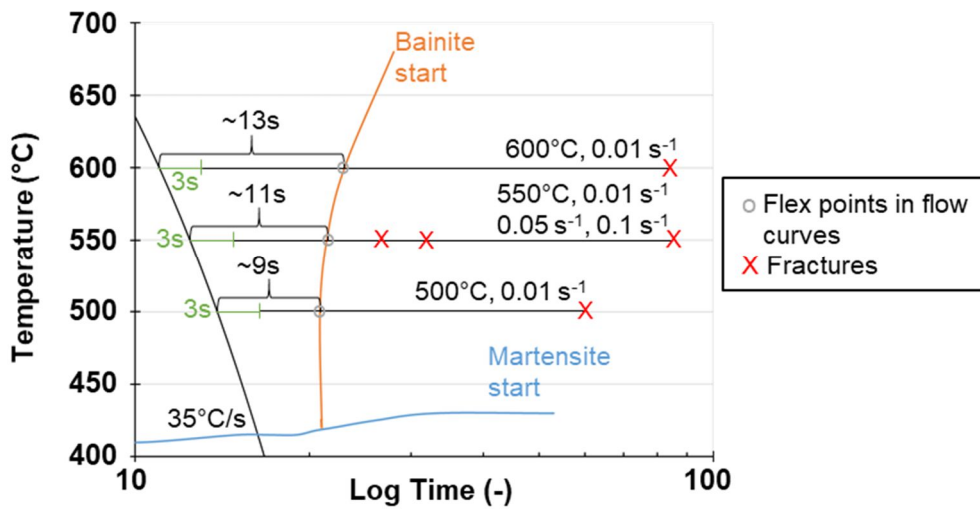


Figure 5.10: Times of the experimental tests compared with CCT curve.

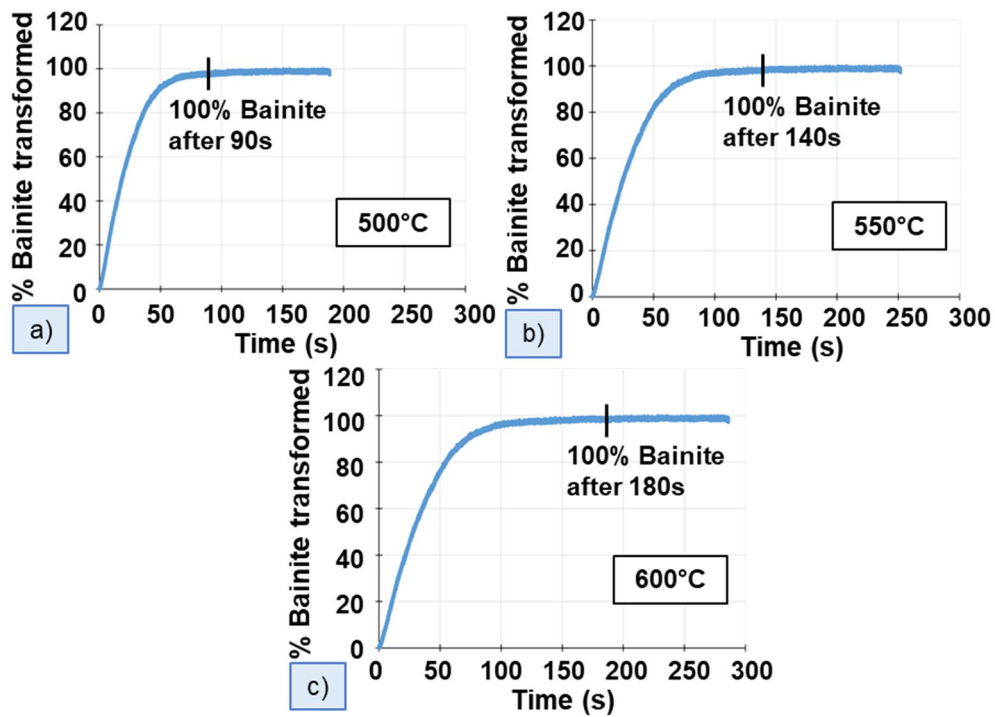


Figure 5.11: Saturation curve of the transformation austenite – bainite at a) 500°C, b) 550°C and c) 600°C.

To confirm this affirmation, a series of optical microscope analysis was performed and Figure 5.12 reports the results. It can be noticed the presence of bainite mixed with martensite for all the tests. The presence of martensite in the analysis is due to the fact that, after the end of the test, the specimens are all cooled down to room temperature with a strong air flux, which allows the transformation of the residual austenite into martensite.

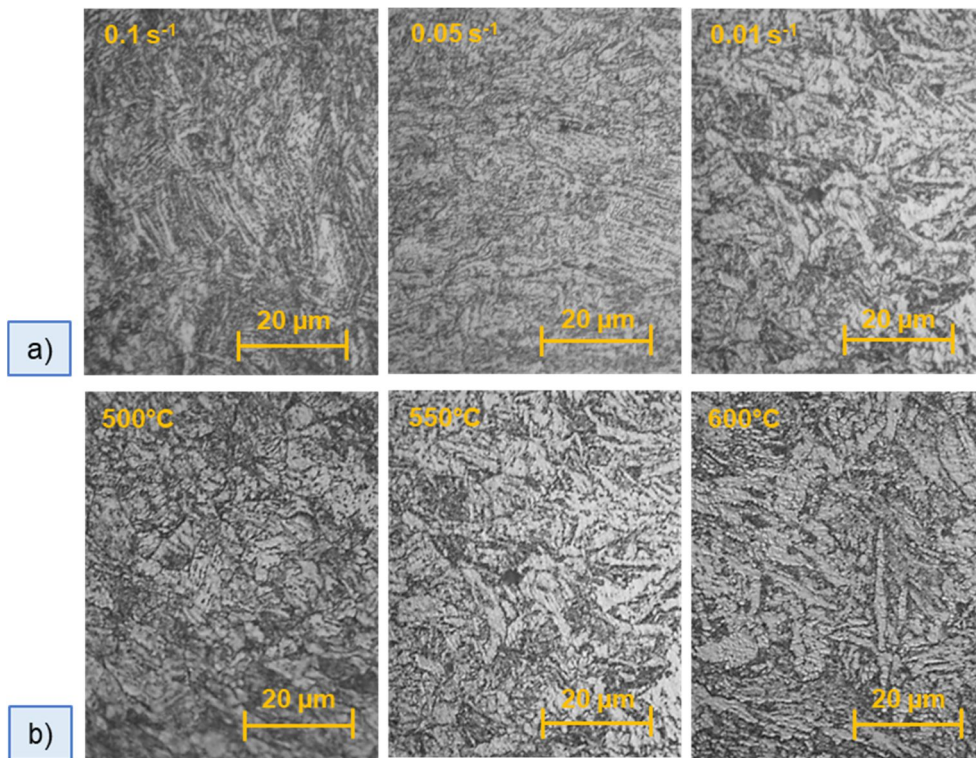


Figure 5.12: Optical microscope pictures of the specimens tested a) at constant  $T_{test} = 550^{\circ}\text{C}$ , b) at constant strain rate =  $0.01\text{ s}^{-1}$ .

These tests show that the applied thermal cycle, with the cooling rate equal to  $35^{\circ}\text{C/s}$ , leads to a mixture of phases when the tensile tests are performed near the bainitic nose. This is an unwanted situation both in the process, due to the fact that the true strain after the flex points increases of about 150-250 MPa, depending on the conditions, which cannot be neglected, and in the study of the austenite phase, to collect the necessary curves for the numerical simulations. For this reasons, a cooling rate of  $80^{\circ}\text{C/s}$  was chosen, instead of  $35^{\circ}\text{C/s}$ , to perform the whole set of tests to study the rheology of the pure austenite phase.

### 5.2.2 Rheology of the Ferrite + Pearlite mixture of phases

The 22MnB5 in the as-delivered conditions present a mixture made of 60% ferrite and 40% pearlite, as shown in Figure 3.1. It is important to understand the behaviour of the material in the non-treated conditions, in order to better understand all the results that are obtained after the thermal treatments.

Moreover, the data of the initial ferrite + pearlite mixture are important when the indirect hot stamping process or the tailor tempering process are considered as reference. Figures 5.13, 5.14 and 5.15 reports the results of the tensile tests performed on the ferrite + pearlite mixture, applying the thermal cycle shown in Figure 3.10 (a).

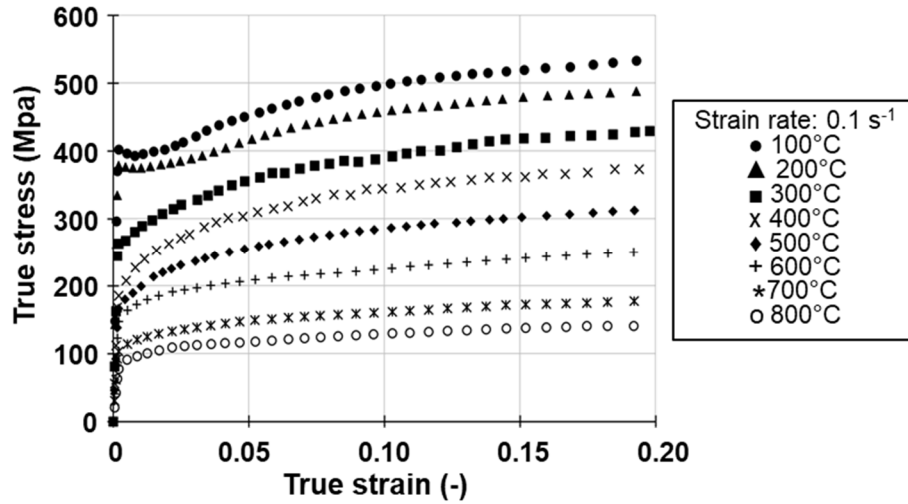


Figure 5.13: Ferrite + pearlite mixture tensile tests results for  $0.1 \text{ s}^{-1}$ .

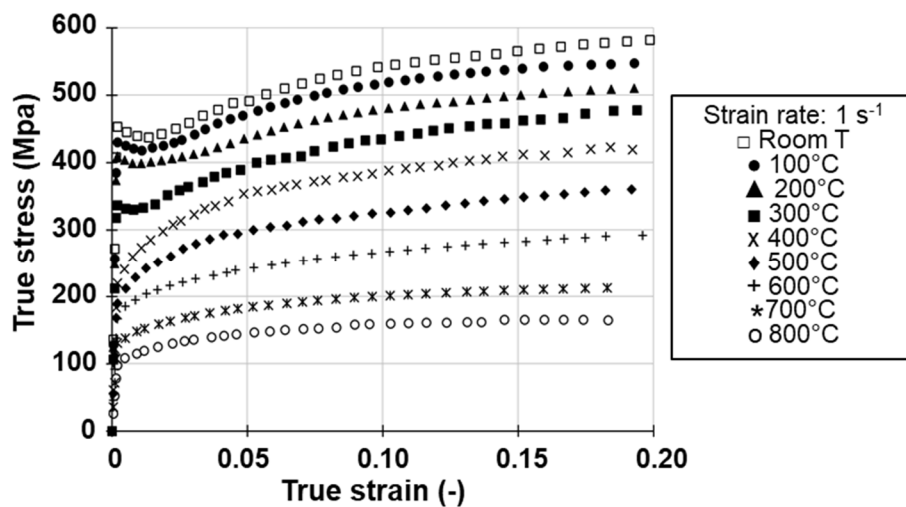


Figure 5.14: Ferrite + pearlite mixture tensile tests results for  $1 \text{ s}^{-1}$ .

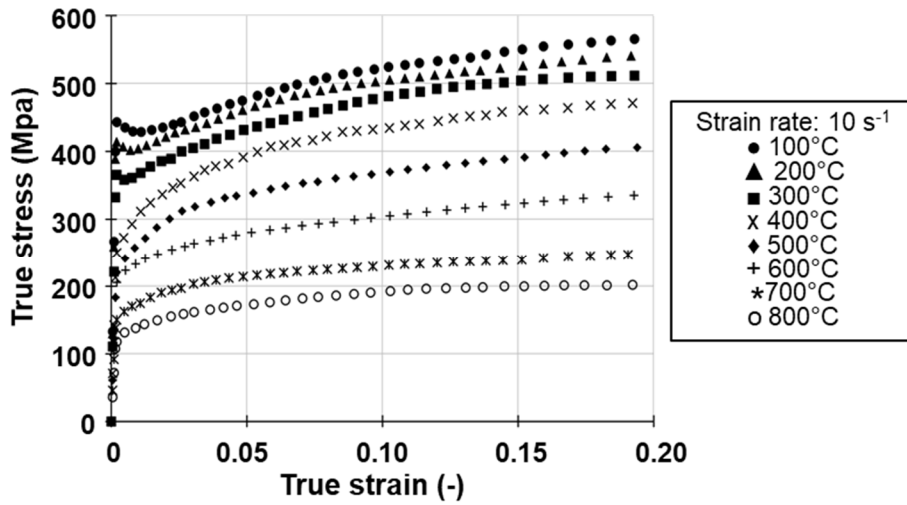


Figure 5.15: Ferrite + pearlite mixture tensile tests results for  $10 \text{ s}^{-1}$ .

The experimental data collected are in agreement with the literature [40]. The curves at the lower temperatures, namely room temperature,  $100^\circ\text{C}$ ,  $200^\circ\text{C}$  and  $300^\circ\text{C}$ , the curves present the upper yield strength, which represents the point at which a sudden levelling or drop in stress or load occurs as a material transition from elastic to plastic deformation. It also marks the beginning of yield point elongation (YPE) [98]. The strain rate influences the behaviour of the curves at  $300^\circ\text{C}$  since at  $0.1 \text{ s}^{-1}$  the upper yield strength is not visible while it becomes evident increasing the strain rate to  $1 \text{ s}^{-1}$  or  $10 \text{ s}^{-1}$ .

### 5.2.3 Rheology of the Austenite phase

The austenite phase was studied in detail, analysing numerous testing temperatures, starting from  $500^\circ\text{C}$  up to  $850^\circ\text{C}$  with a range of  $50^\circ\text{C}$ , according to the thermal cycle shown in Figure 3.10 (b). The true stress – true strain curves describing the austenite phase are shown in Figures 5.16, 5.17 and 5.18. The presented curves are in good agreement with the curves presented in literature [18, 34, 36, 37] and the effect on the strain rate is evident comparing the three plots.

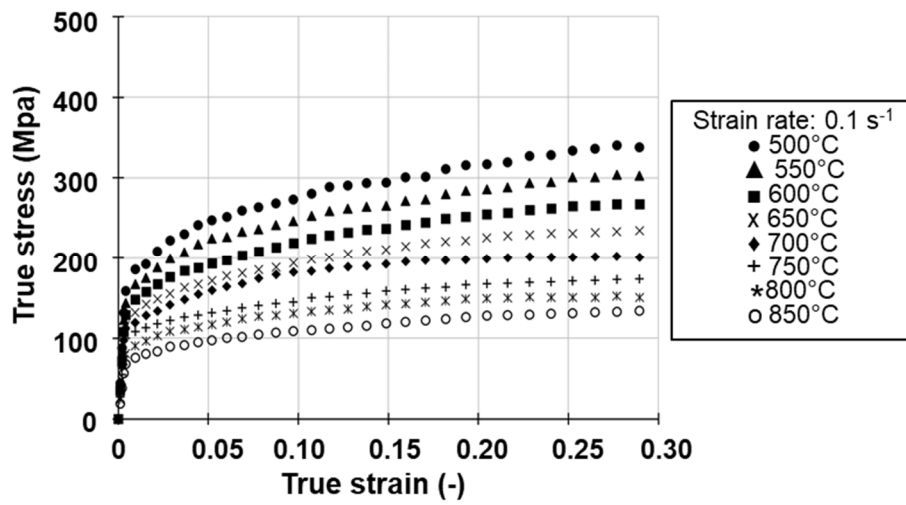


Figure 5.16: Austenite phase tensile tests results for  $0.1 \text{ s}^{-1}$ .

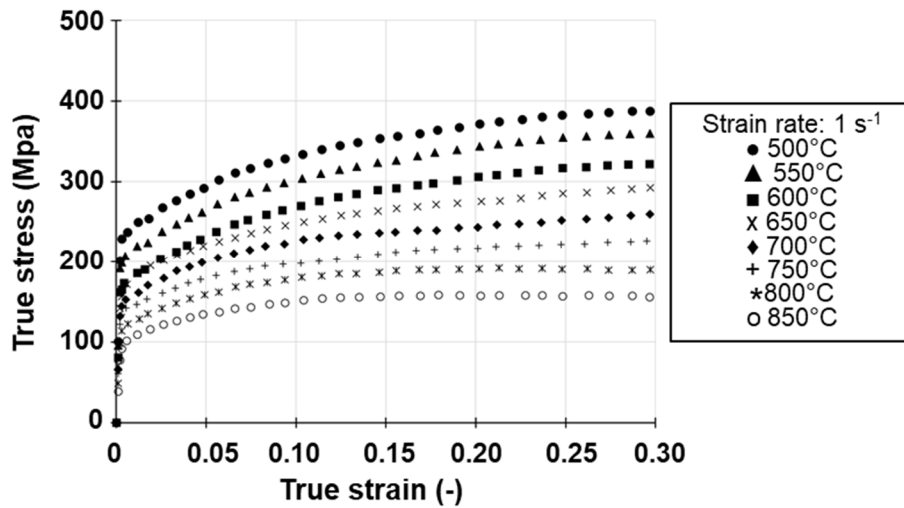


Figure 5.17: Austenite phase tensile tests results for  $1 \text{ s}^{-1}$ .

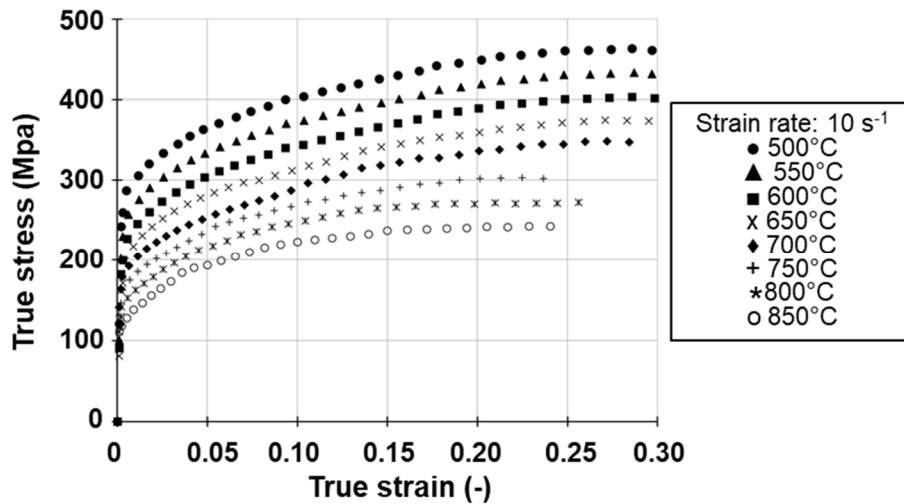


Figure 5.18: Austenite phase tensile tests results for  $10 \text{ s}^{-1}$ .

#### 5.2.4 Rheology of the Bainite phase

The tensile tests of the bainite phase are performed dividing the thermal cycle in two parts: the first part regards the stripe, and it is necessary to transform the ferrite + pearlite mixture, first in austenite, then in bainite; the second part regards the specimen, water cut from the treated stripe, and it is performed in the MTS equipped with the electrical power generator and the PEEK-Cu grips. The first tests performed on the bainite phase were to verify the sensitivity to strain rate and temperatures, since the range of the tested temperature included low temperatures, such as  $100^\circ\text{C}$ ,  $200^\circ\text{C}$  and  $300^\circ\text{C}$ . Figure 5.19 reports the preliminary tests performed at  $300^\circ\text{C}$  at  $0.1 \text{ s}^{-1}$  and  $10 \text{ s}^{-1}$ . The shift between the curves is very tiny and the sensitivity to the temperature and strain rate, until  $300^\circ\text{C}$ , can be negligible.

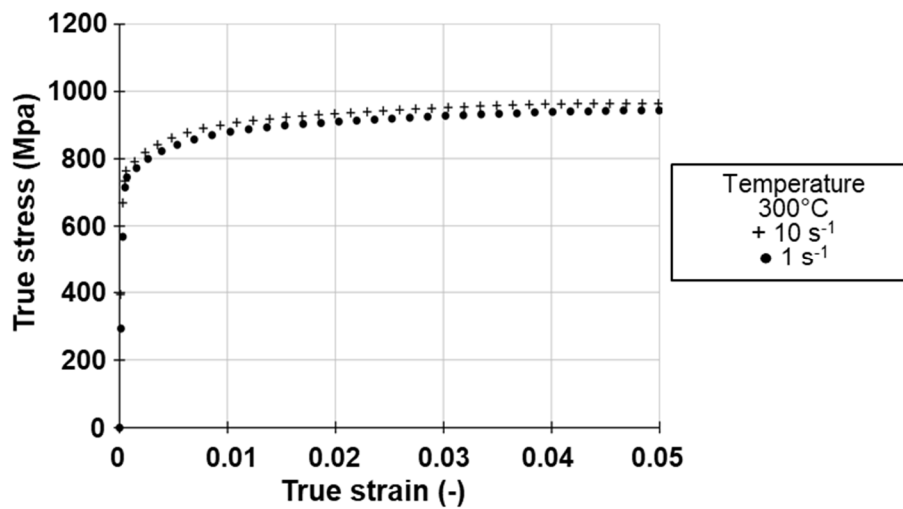


Figure 5.19: Temperature and strain rate sensitivity of bainite phase.

According to the preliminary tests, the experimental plan for the testing of the bainite phase can be modified as reported in Table 5.3.

Table 5.3: New experimental plan for the bainite phase.

Temperature (°C)	Strain Rate (s <sup>-1</sup> )
20	
100	
200	1
300	
400	0.1
500	1
600	10

Figures 5.20, 5.21, 5.22 and 5.23 reports the experimental results of the tensile tests of the bainite phase according to the experimental plan reported in Table 5.3.

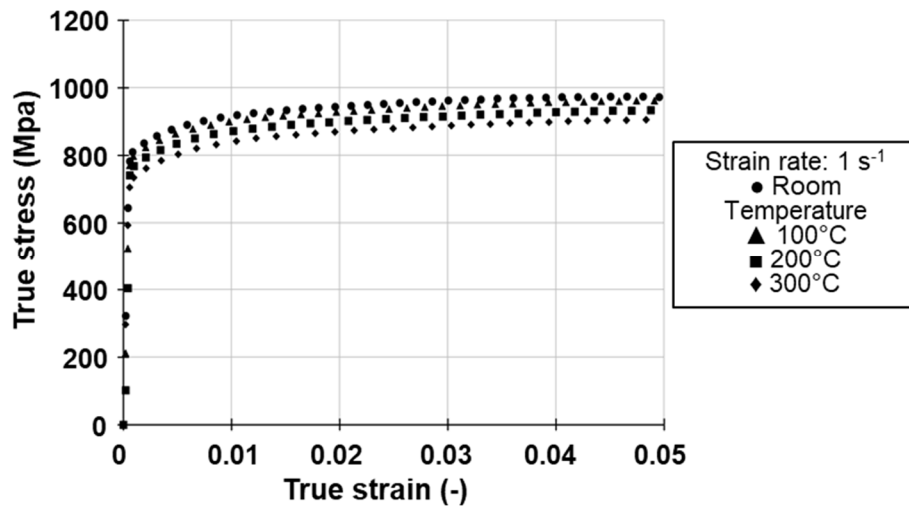


Figure 5.20: Bainite phase tensile tests results for low temperatures,  $1 \text{ s}^{-1}$ .

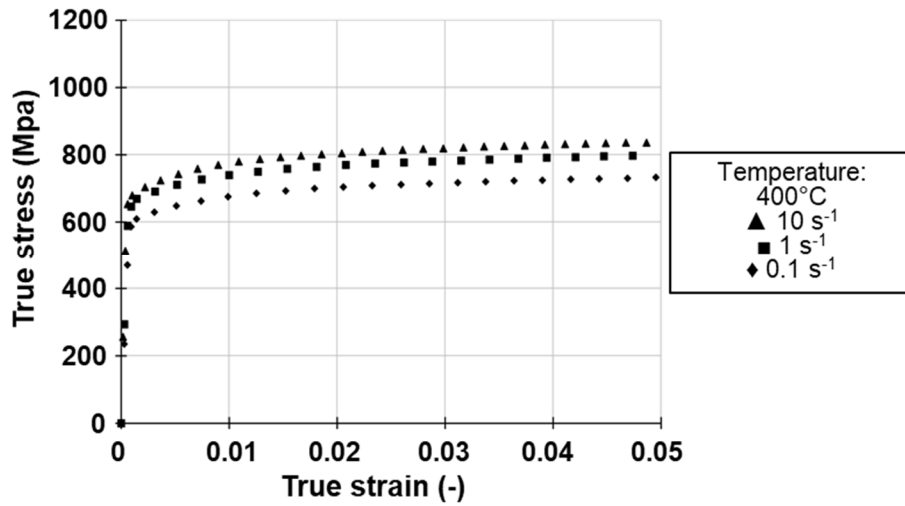


Figure 5.21: Bainite phase tensile tests results for  $400^\circ\text{C}$ .

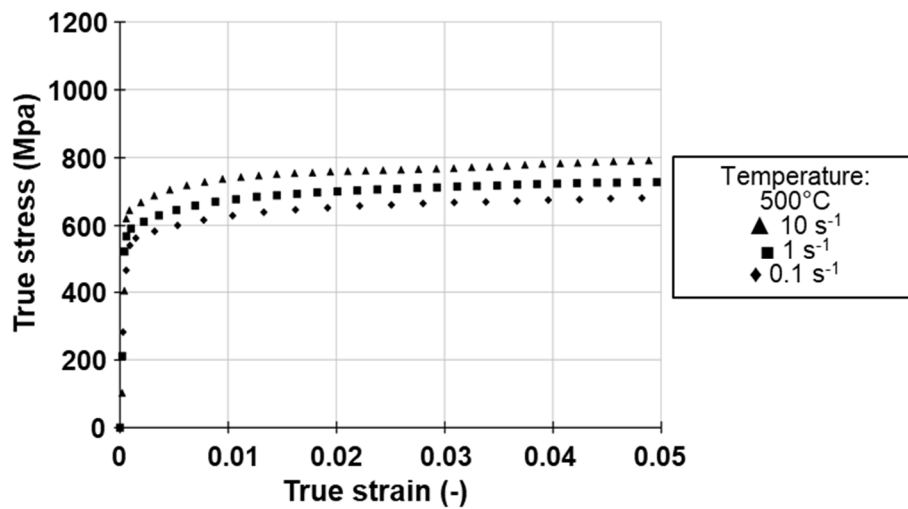


Figure 5.22: Bainite phase tensile tests results for 500°C.

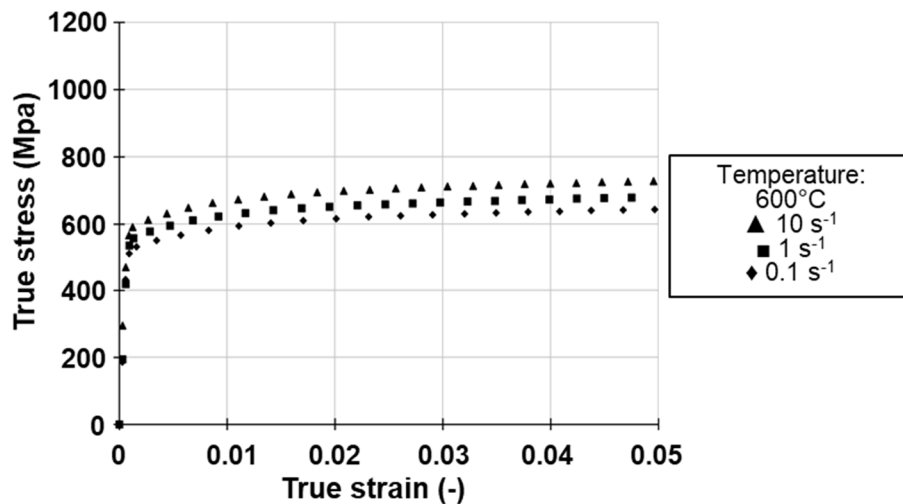


Figure 5.23: Bainite phase tensile tests results for 600°C.

### 5.2.5 Rheology of the Martensite phase

The tensile tests for the martensite phase were performed following the same procedure applied for the bainite phase. Before starting the experimental campaign of tensile tests for the martensite phase, the same sensitivity tests performed for the bainite phase were done. Figure 5.24 reports the results of the sensitivity tests, showing that even the martensite phase is not sensitive to the variation of temperature or strain rate. According to these results, the experimental plan for the martensite phase changed as reported in Table 5.4.

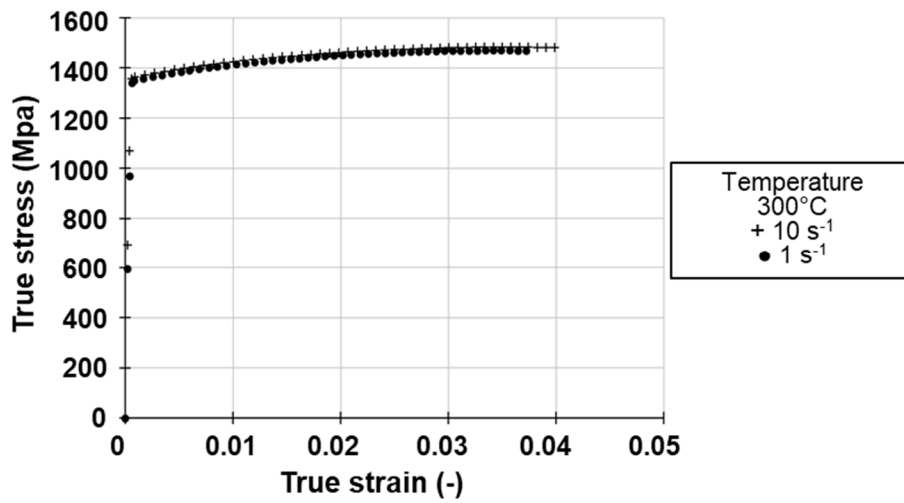


Figure 5.24: Temperature and strain rate sensitivity of the martensite phase.

Table 5.4: New experimental plan for the martensite phase.

Temperature (°C)	Strain Rate (s <sup>-1</sup> )
20	1
100	
200	
300	

In Figure 5.25 the experimental results of the tensile tests of pure martensite phase are reported. The curves at different temperatures are very close to one another, showing a lower dependency to temperature in respect with bainite tested in the same conditions. This can be due to the higher toughness of the martensite phase, in respect with bainite phase that lowers the sensitivity to temperature.

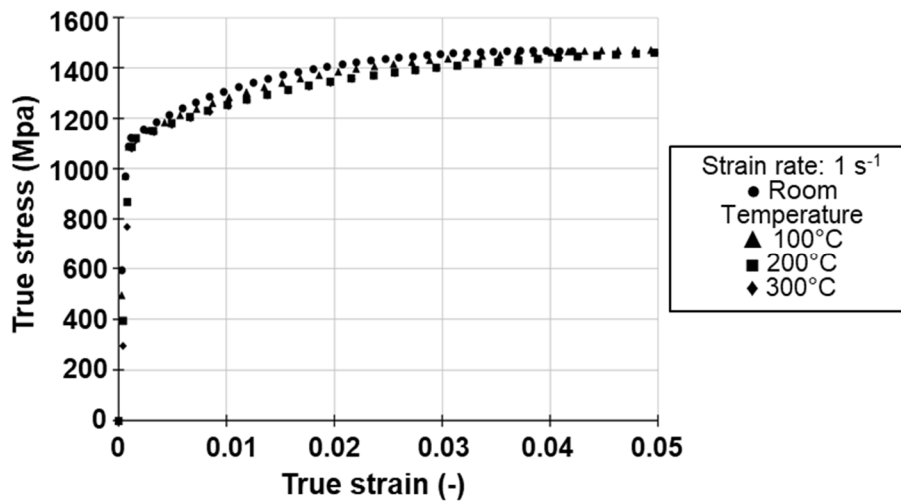


Figure 5.25: Martensite phase tensile tests results.

### 5.2.6 Analysis of the temperature

In order to confirm the goodness of the performed tests, it is necessary to assure that the hot tensile tests are performed at the correct temperature without massive variation during the test itself. Figure 5.26 shows the variation of the temperature during the tensile test for all the testing temperatures involved in this work. Table 5.5 presents the values of the maximum and minimum temperatures recorded during the test and the corresponding percentage of variation in respect to the reference temperature. The results show that the variation of temperature is very low and this represents the goodness of the heating system and the goodness of the hot tensile tests reported in the present work.

Table 5.5: Temperature variations during the hot tensile test.

Testing Temperature (°C)	Min T (°C)	Min % variation	Max T (°C)	Max % variation
800	790.07	-1.24	809.61	1.20
700	693.86	-0.88	707.62	1.09
600	595.31	-0.78	606.88	1.15
500	495.32	-0.94	504.04	0.81
400	395.61	-1.10	404.36	1.09
300	295.67	-1.44	305.24	1.75
200	196.38	-1.81	203.11	1.55
100	97.30	-2.70	102.86	2.86

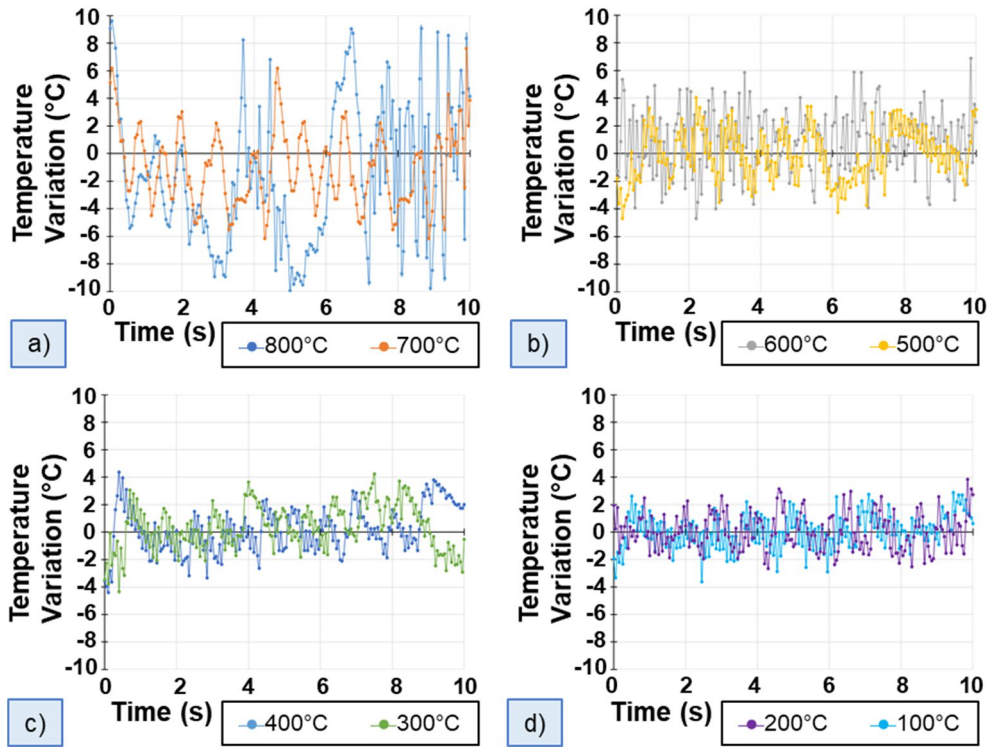


Figure 5.26: Temperature variation for the different testing temperatures involved in the paper, a) 800-700°C, b) 600-500°C, c) 400-300°C, d) 200-100°C.

### 5.3 Modified Johnson-Cook fitting model

#### 5.3.1 Calibration of the model

The experimental results were then fit using the original Johnson-Cook model [99] according to the following formulation:

$$\sigma_f = (A + B\varepsilon^n) \left[ 1 + C \ln \left( \frac{\dot{\varepsilon}}{\dot{\varepsilon}_0} \right) \right] \left[ 1 - \left( \frac{T - T_0}{T_m - T_0} \right)^m \right] \quad (5.1)$$

Where  $\varepsilon$  is the strain,  $\dot{\varepsilon}$  is the strain rate and  $T$  is the temperature (in Kelvin) at which the test is conducted;  $\dot{\varepsilon}_0$  and  $T_0$  are, respectively, the strain rate and the temperature of the quasi-static test, which, for this work, were selected as  $0.01 \text{ s}^{-1}$  and  $293\text{K}$ ;  $T_m$  is the melting temperature of the material tested, set at  $1723\text{K}$ .  $A$ ,  $B$ ,  $C$ ,  $n$  and  $m$  are the variables of the model which are found using linear regression having, as target, the minimization of the sum of the differences between the experimental and the calculated values of the stress,  $\sigma$ :

The Johnson-Cook model was used to fit the experimental data in order to implement the rheological behaviour of the 22MnB5 in FE software. The Johnson-Cook model fails to fit the flow curves at high temperature since it cannot represent the correct influence of the strain rate [22]. Figure 5.27 (a) shows the fitting of the curves at 850°C tested at 0.1 s<sup>-1</sup>, 1 s<sup>-1</sup> and 10 s<sup>-1</sup> in pure austenite phase, while Figure 5.27 (b) represents the difference (delta,  $\Delta$ ) between the experimental and the calculated values of the stress, according to the following equation:

$$\Delta\sigma = \sigma_{exp} - \sigma_{JC} \quad (5.2)$$

Where  $\sigma_{exp}$  is the experimental value of the stress and  $\sigma_{JC}$  is the calculated value of the stress according to the Johnson-Cook model. A positive value of  $\Delta\sigma$  means that the experimental value is higher than the calculated one, and so the fitting curve is lower than the experimental one; a negative value of  $\Delta\sigma$  means that the experimental value is lower than the calculated one, and so the fitting curve is higher than the experimental one. Table 5.6 shows the parameters used to fit the experimental data and Table 5.7 reports the average percentage errors between the experimental and the calculated values of the stress. Negative average errors means that the experimental curve is lower than the calculated one.

Table 5.6: Parameters of the Johnson-Cook original model.

Parameter	Value
<b>A</b>	2686.52 MPa
<b>B</b>	16994.6 MPa
<b>n</b>	0.222980 (-)
<b>C</b>	0.214590 MPa
<b>m</b>	0.013317 (-)

Table 5.7: Average percentage errors between the  $\sigma_{exp}$  and  $\sigma_{JC}$ .

Test conditions	Average % error
<b>850°C - 0.1 s<sup>-1</sup></b>	-8.20
<b>850°C - 1 s<sup>-1</sup></b>	-12.07
<b>850°C - 10 s<sup>-1</sup></b>	2.86

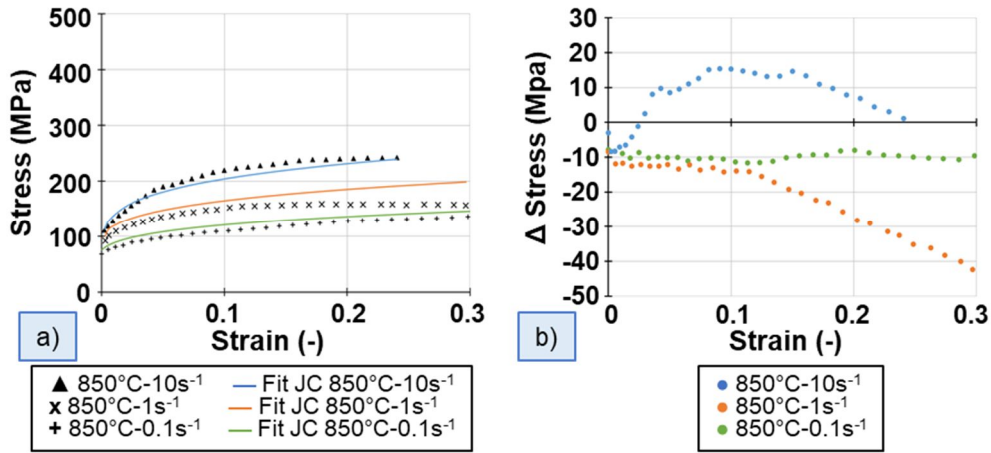


Figure 5.27: Experimental results for pure austenite phase tested at 850°C, at 0.1 s<sup>-1</sup>, 1 s<sup>-1</sup> and 10 s<sup>-1</sup> fit with original Johnson-Cook model, a) flow curves, b)  $\Delta\sigma$ .

For this reason, a modified Johnson-Cook model is here proposed, formulates as reported in Equation 5.3:

$$\sigma_f = (B\varepsilon^n) \left\{ 1 + \left[ \ln \left( \frac{\dot{\varepsilon}}{\dot{\varepsilon}_0} \right) \right]^k \right\} \left[ 1 - D \exp \left( \frac{T - T_0}{T_m - T_0} \right)^m \right] \left[ \dot{\varepsilon}^{j(T - T_0)} \exp \left( \frac{lQ}{RT} \right) \right] \quad (5.3)$$

Where  $\varepsilon$  is the strain,  $\dot{\varepsilon}$  is the strain rate and  $T$  is the temperature (in Kelvin) at which the test is conducted;  $\dot{\varepsilon}_0$  and  $T_0$  are, respectively, the strain rate and the temperature of the quasi-static test which were selected as 0.01 s<sup>-1</sup> and 293K;  $T_m$  is the melting temperature of the material tested, set ad 1723K;  $R$  is the universal gas constant and  $Q$  is the activation energy.  $B$ ,  $D$ ,  $n$ ,  $k$ ,  $m$ ,  $j$  and  $l$  are the variables of the model which are found using linear regression having, as target, the minimization of the sum of the differences between the experimental and the calculated values of the stress,  $\sigma$ .

The first modification to the model regards the term  $(A + B\varepsilon^n)$  which is modified in  $(B\varepsilon^n)$ . The effect of this modification is shown in Figure 5.28 (a). The modification of the first term of the equation reduces the delta for the curves relative to the strain rate 1 s<sup>-1</sup>; on the other hand, the modification of the first term brings almost no modification to the curve relative to the 0.1 s<sup>-1</sup> strain rate, and even rise the delta relative to the 10 s<sup>-1</sup> curve. The second modification to the model regards the term  $\left[ 1 + C \ln \left( \frac{\dot{\varepsilon}}{\dot{\varepsilon}_0} \right) \right]^k$  which is modified in  $\left\{ 1 + \left[ \ln \left( \frac{\dot{\varepsilon}}{\dot{\varepsilon}_0} \right) \right]^k \right\}$ . The effect of this modification is shown in Figure 5.28 (b). The modification of this second term of the equation reduces the delta for the curves relative to the strain rate 0.1 s<sup>-1</sup> and 10 s<sup>-1</sup>; the modification of the second term flattens but lowers, the

curve of the delta relative to the  $1 \text{ s}^{-1}$  case. The second modification to the model regards the term  $\left[1 - \left(\frac{T-T_0}{T_m-T_0}\right)^m\right]$  which is modified in  $\left[1 - D \exp\left(\frac{T-T_0}{T_m-T_0}\right)^m\right]$ . The effect of this modification is shown in Figure 5.28(c). The modification of the third term of the equation reduces the delta for all the curves.

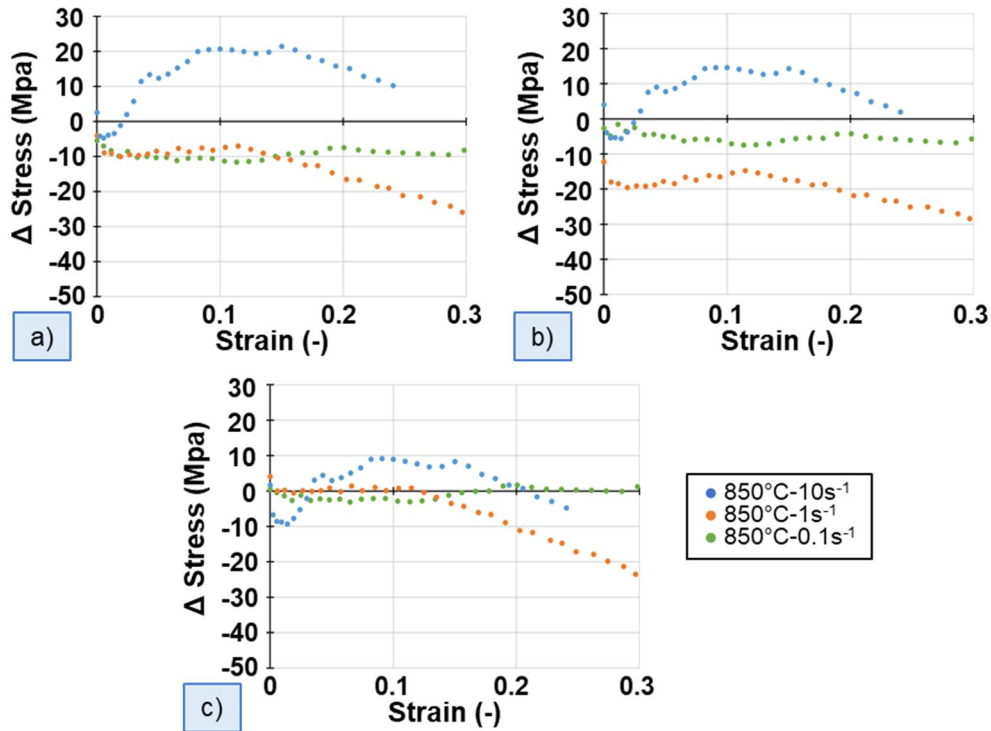


Figure 5.28: Delta between experimental and calculated stress a) first term modified, b) second term modified, c) third term modified.

In order to flatten all the three curves, a new term,  $\left[\dot{\epsilon}^{j(T-T_0)} \exp\left(\frac{lQ}{RT}\right)\right]$ , is added to the modified equation, and the effect of all the four terms is shown in Figure 5.29 (a), where the deltas are shown, and Figure 5.29 (b), where the whole experimental curves are shown and fit with the modified Johnson-Cook model.

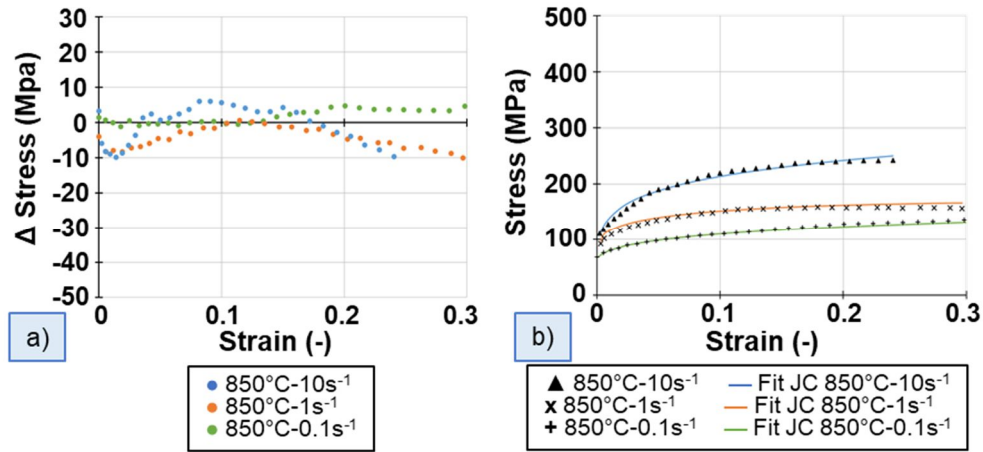


Figure 5.29: a) Delta between experimental and calculated stress, fourth term added, b) flow curves pure of austenite phase tested at 850°C, at 0.1 s<sup>-1</sup>, 1 s<sup>-1</sup> and 10 s<sup>-1</sup> fit with modified Johnson-Cook model.

With this modified Johnson-Cook model the values of the average errors are almost halved, as reported in Table 5.8.

Table 5.8: Average percentage errors between the  $\sigma_{exp}$  and  $\sigma_{JCM}$ .

Test conditions	Average % error
850°C - 0.1 s <sup>-1</sup>	1.40
850°C - 1 s <sup>-1</sup>	-3.07
850°C - 10 s <sup>-1</sup>	-0.62

### 5.3.2 Ferrite + Pearlite curves fitting

The experimental flow curves of the mixture ferrite + pearlite were fitted using the new Johnson-Cook model presented. Figures 5.30, 5.31 and 5.32 and Table 5.9 reports the flow curves and the parameters of the model respectively. The curves at low temperature, namely room temperature, 100°C, 200°C and 300°C, show the upper yield strength, which brings the initial part of the curve to be higher than the model predicts.

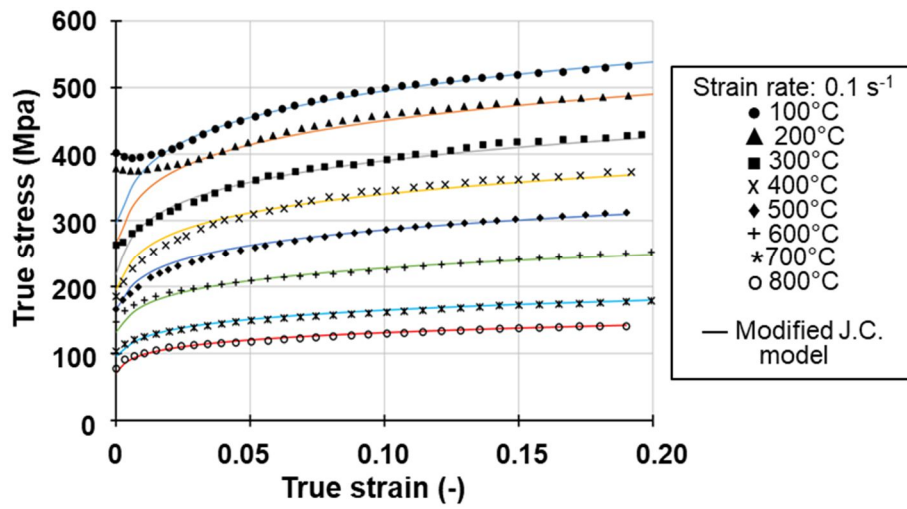


Figure 5.30: Fitted flow curves of the mixture ferrite+ pearlite tested at  $0.1 \text{ s}^{-1}$ .

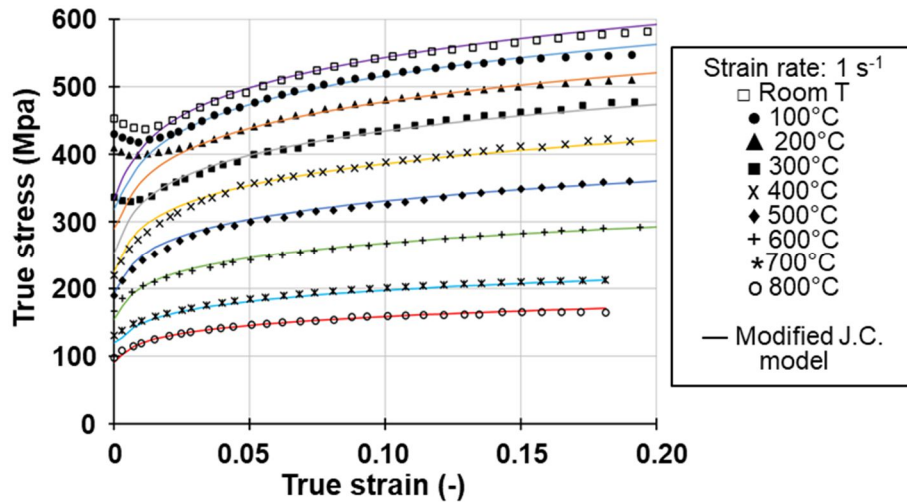


Figure 5.31: Fitted flow curves of the mixture ferrite+ pearlite tested at  $1 \text{ s}^{-1}$ .

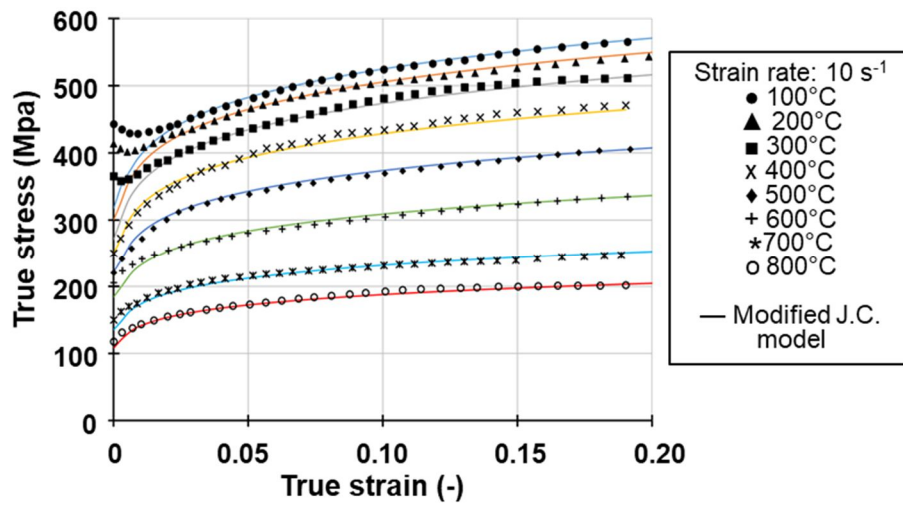


Figure 5.32: Fitted flow curves of the mixture ferrite+ pearlite tested at  $10 \text{ s}^{-1}$ .

Table 5.9: Parameters of the modified Johnson-Cook model used to fit the ferrite + pearlite flow curves.

Parameter	Value
<b>B</b>	505.229
<b>n</b>	0.121000
<b>k</b>	0.033937
<b>D</b>	0.315312
<b>m</b>	1.82261
<b>j</b>	0.000107
<b>l</b>	0.0000503

### 5.3.3 Austenite curves fitting

The experimental flow curves of the austenite phase were fitted using the new Johnson-Cook model presented. Figure 5.33, 5.34 and 5.35 and Table 5.10 reports the flow curves and the parameters of the model respectively.

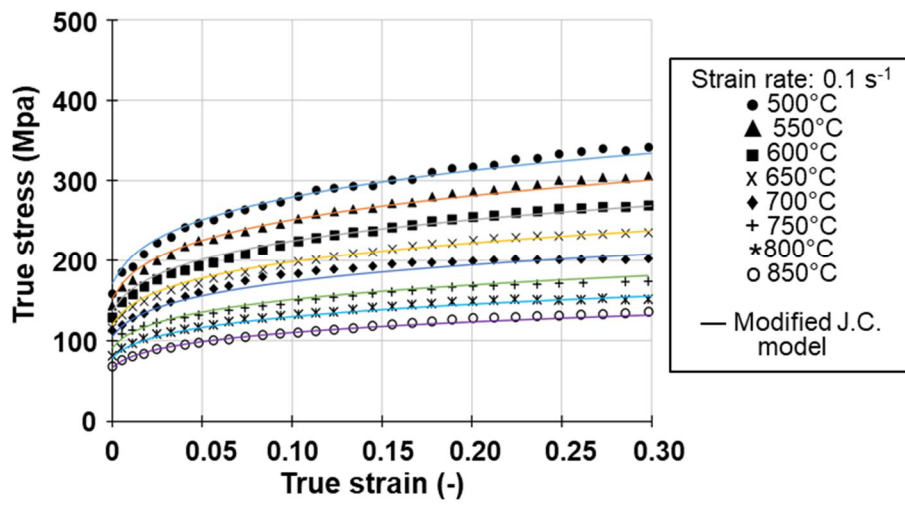


Figure 5.33: Fitted flow curves of the austenite phase tested at  $0.1 \text{ s}^{-1}$ .

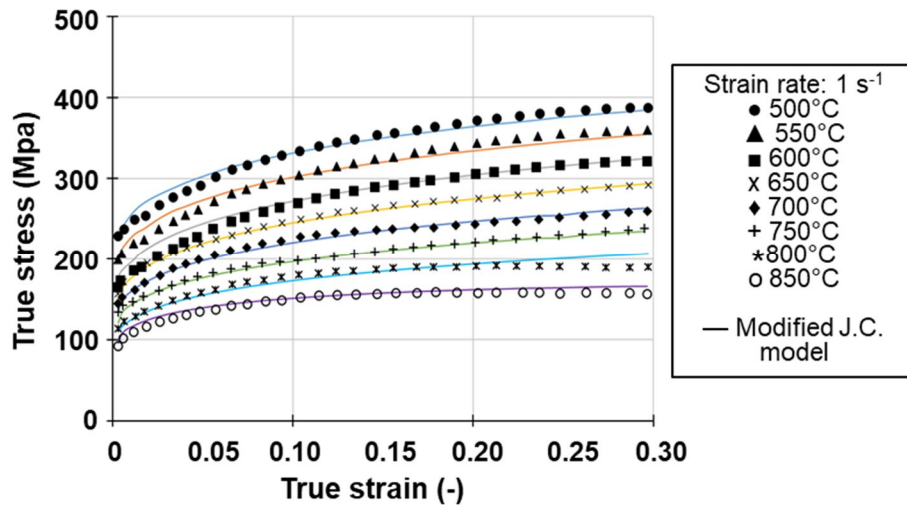


Figure 5.34: Fitted flow curves of the austenite phase tested at  $1 \text{ s}^{-1}$ .

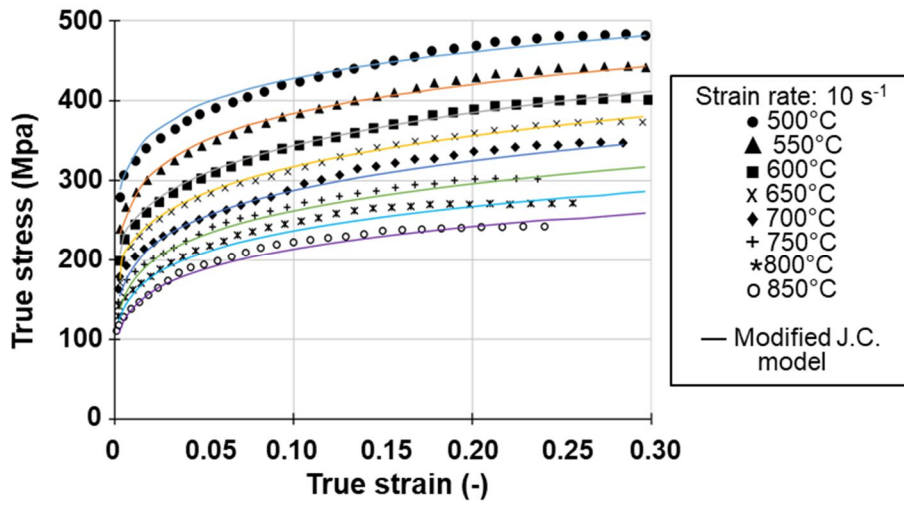


Figure 5.35: Fitted flow curves of the austenite phase tested at  $10\text{ s}^{-1}$ .

Table 5.10: Parameters of the modified Johnson-Cook model used to fit the austenite flow curves.

Parameter	Value
<b>B</b>	1258.64
<b>n</b>	0.168887
<b>k</b>	-0.342314
<b>D</b>	0.715311
<b>m</b>	0.408287
<b>j</b>	0.045742
<b>l</b>	0.000213

### 5.3.4 Bainite curves fitting

The thermal treated dog-bone specimens, which are made of pure bainite phase, were hot tensile tested according to the experimental plan presented in Table 5.3. The modified Johnson-Cook model was used to fit the experimental data, as reported in Figure 5.36, 5.37, 5.38 and 5.39. The fitting is very good and is able to represent all the experimental curves. Table 5.11 reports the parameters of the model.

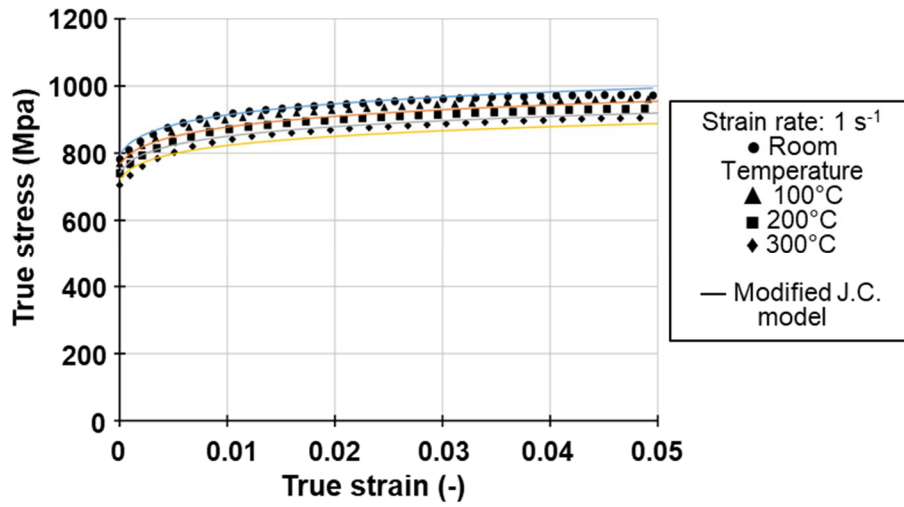


Figure 5.36: Tensile tests results for the pure bainite phase: low temperatures,  $1s^{-1}$ .

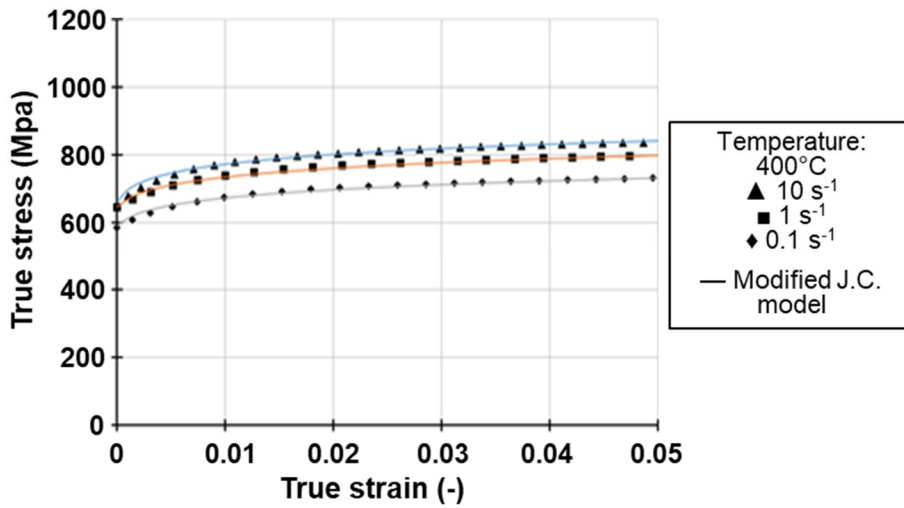


Figure 5.37: Tensile tests results for the pure bainite phase: 400°C.

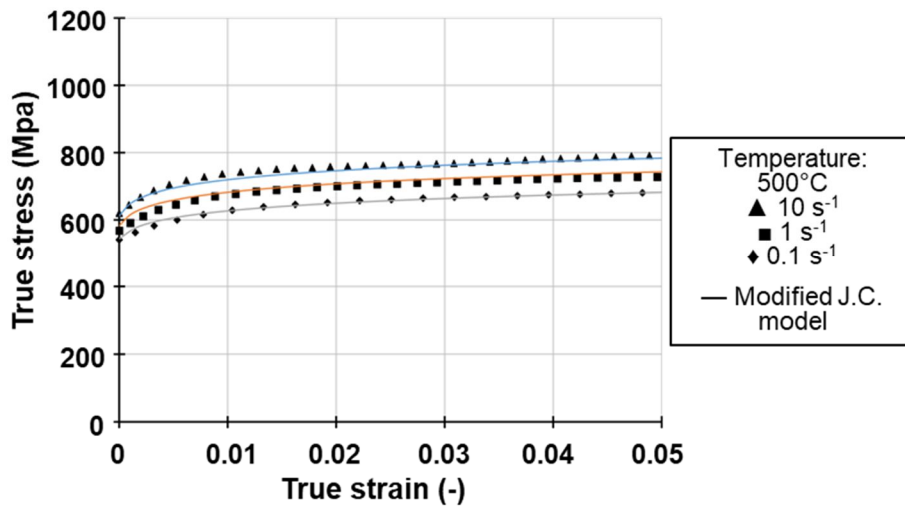


Figure 5.38: Tensile tests results for the pure bainite phase: 500°C.

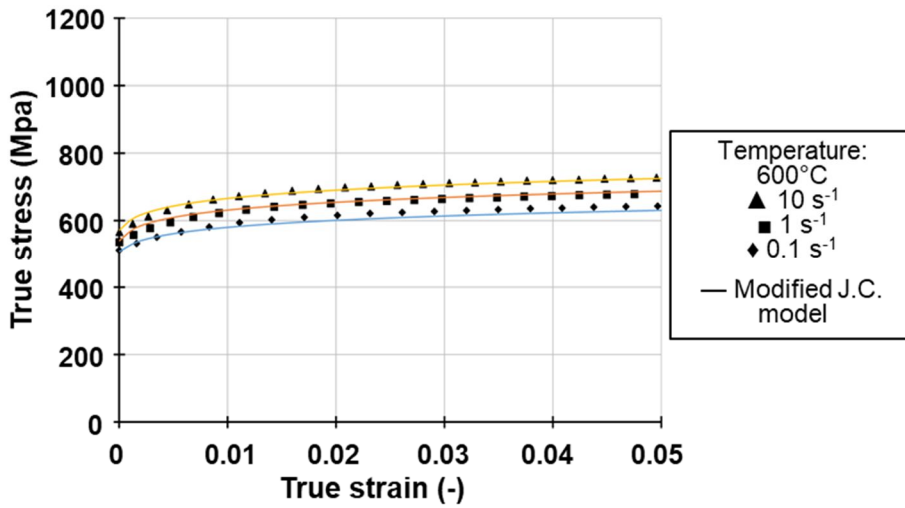


Figure 5.39: Tensile tests results for the pure bainite phase: 600°C.

Table 5.11: Parameters of the modified Johnson-Cook model used to fit the austenite flow curves.

Parameter	Value
<b>B</b>	1554.69
<b>n</b>	0.054275
<b>k</b>	0.221112
<b>D</b>	0.686795
<b>m</b>	0.324316
<b>j</b>	0.000198
<b>l</b>	0.0000176

### 5.3.5 Martensite curves fitting

The thermal treated dog-bone specimens, which are made of pure martensite phase, were hot tensile tested according to the experimental plan presented in Table 5.4. The experimental results of the hot tensile test for the pure martensite phase fit with the modified Johnson-Cook model are shown in Figure 5.40. The fitting is very good, the model can predict the insensitivity to the strain rate and the temperature. Table 5.12 reports the parameters of the model.

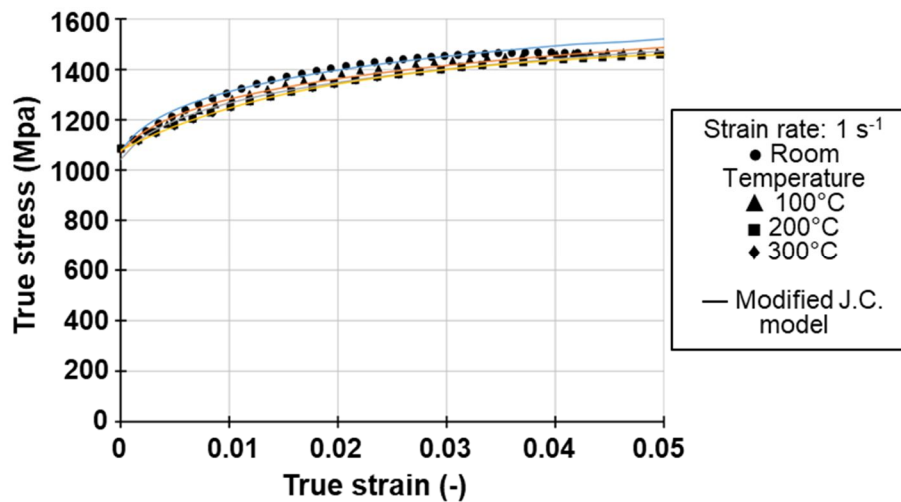


Figure 5.40: Tensile tests results for the pure martensite phase tested at  $1s^{-1}$ .

Table 5.12: Parameters of the modified Johnson-Cook model used to fit the austenite flow curves.

Parameter	Value
<b>B</b>	779.382
<b>n</b>	0.101467
<b>k</b>	0.440854
<b>D</b>	0.124254
<b>m</b>	0.833729
<b>j</b>	0.000176
<b>l</b>	0.000848

## 5.4 Study of the formability of 22MnB5

### 5.4.1 Influence of the temperature

The influence of the temperature on the formability of 22MnB5 was studied applying the thermal cycle shown in Figure 3.16 (a) to 1.50( $\pm 0.05$ ) mm thick sheets. All seven geometries were used for this experimental campaign, namely 30mm, 50 mm, 75 mm, 100 mm, 125 mm, 150 mm and 200 mm. Figures 5.41 and 5.42 display the FLCs determined under isothermal conditions at 600°C and 500°C and the comparison between them.

The FLC obtained at 600°C shows higher formability than the one at 500°C, meaning that higher temperature induces higher material formability, allowing obtaining more complex shapes without having cracks or failures of the material. Figure 5.42 shows the comparison of the two FLCs with the deformed specimens as reference. It is worth to note that the two curves differ in both the branches of the first and second quadrants. This may be due to the temperature that modifies the strain path, which, in turn, means a modification of the strain states to which the part is subjected during deformation. An example is that the plane strain state was obtained with the 75mm wide specimen at 600°C, whereas at 500°C with the 100mm wide specimen. This peculiar behaviour induced by temperature has to be taken into account when complex shapes or high deformation are required to obtain the final part. Another interesting aspect is the position of FLC points relative to the 200 mm geometry. These points should lie on the bisector of the first quadrant, which represent the axisymmetry condition, but, for both the temperatures, the point was found at higher major strain and lower minor strain.

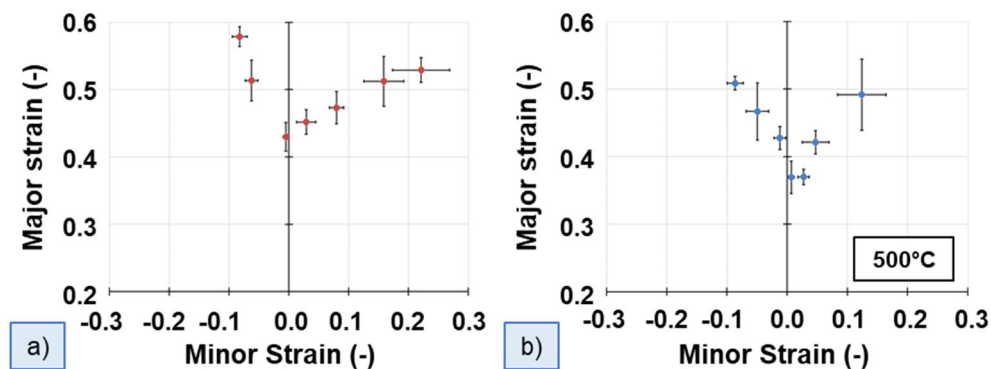


Figure 5.41: FLCs at a) 600°C and b) 500°C.

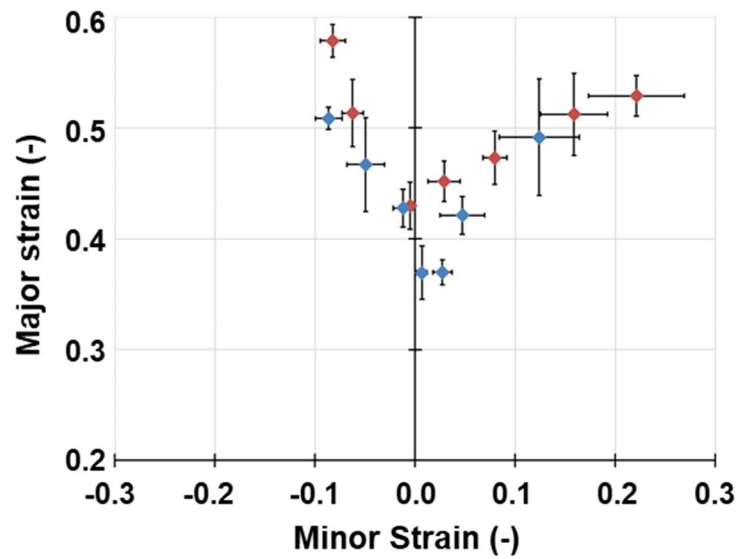


Figure 5.42: Comparison between FLCs at 600°C and 500°C.

#### 5.4.2 Influence of the microstructure

The influence of the microstructure on the formability of 22MnB5 was studied applying the thermal cycles shown in Figure 3.17 (a-c) to 1.50(±0.05) mm thick sheets. Three geometries were used for this experimental campaign, namely 30mm, 100 mm and 200 mm. Figure 5.43 displays the FLCs determined under isothermal conditions at 600°C. The three microstructure mixtures considered are 100% austenite, 50% austenite – 50% bainite and 100% bainite.

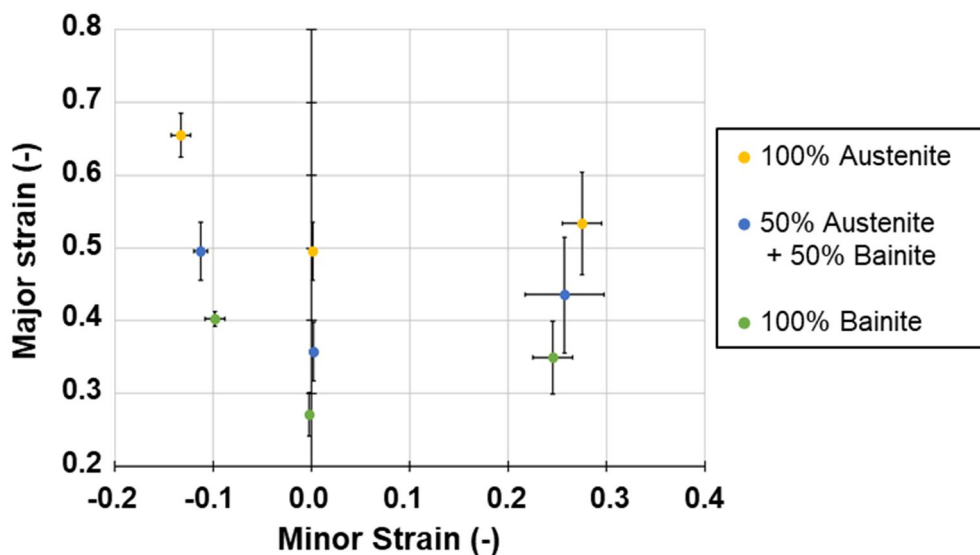


Figure 5.43: FLCs obtained at 600°C for different microstructure.

The higher formability is reached when the specimen is in pure austenite phase, as expected. The formability drops of about the 40% when the tests are performed in pure bainite phase. The curve in the middle, relative to the case 50% austenite and 50% bainite does not stand right in the middle between the others: this can be explained by the fact that during the deformation, the phase transformation continues, even accelerated by the applied strain/stress, and so the final percentage of the two phases cannot be maintained exactly balanced. This also affects the experimental error, as described by the error bands in the plot, which represent the standard deviation from the average value. The differences among the three curves stands also in the minor strain values, which is about the 30% lower in the case of pure bainite compared to the other tested conditions. This means that the piece is more likely to fail if the strain path which describes the deformation is too severe. Similar behaviour was seen comparing FLC at different temperatures, where the lower the testing temperature the lower the material formability due to the microstructural modifications [100].

Comparing the FLC shown in Figure 5.41 (a), obtained with the thermal cycle shown in figure 3.16 (a), with the FLC in pure austenite phase shown in Figure 5.43 and obtained with the thermal cycle in Figure 3.17 (a), it can be seen that the first one is lower than the other, meaning that a certain percentage of bainite is present in the specimen in the moment of fracture. As an example, considering the thermal cycle and the duration of the test of the 200 mm geometry at 600°C, it can be calculated that at rupture the percentage of bainite is about 20%, and it is not negligible.

## **5.5 Numerical simulations results**

### **5.5.1 CCT left-shift simulations**

The CCT left-shift is an important phenomenon to consider since it influences both the behaviour of the material and the design of the dies. For this reason, it is very important to reproduce the behaviour in the numerical simulations. LS-DYNA code allows the implementation of the CCT left- shift with MAT\_244\_UHS\_STEEL, thanks to the parameters LCEPS4 and LCEPS5 (§4.1). Figure 5.44 shows the numerical CCT curve obtained applying a 20% pre-

strain at 800°C with a strain rate of 0.1 s<sup>-1</sup>. Table 5.13 lists the values of LCEPSi implemented in the numerical simulations to obtain the shift in the curves.

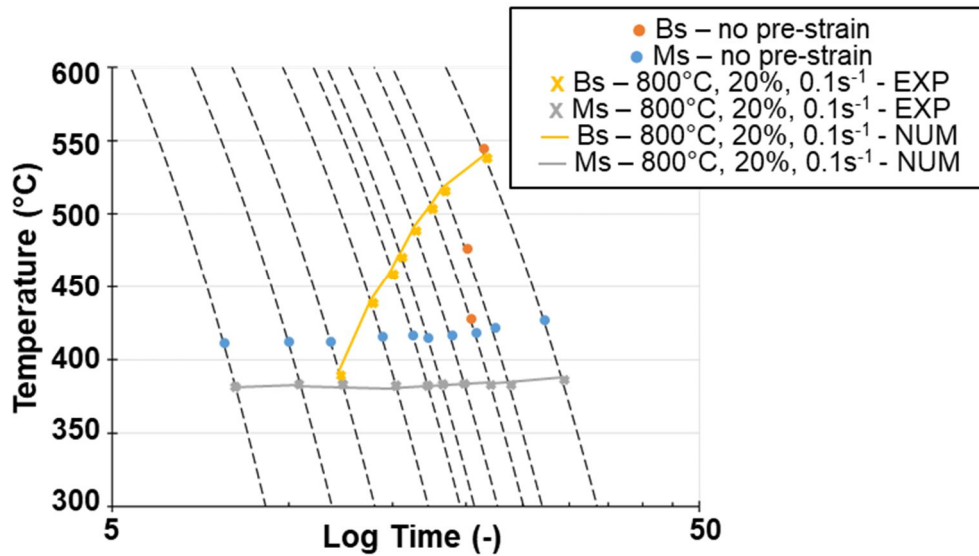


Figure 5.44: Comparison between experimental and numerical results CCT left-shift, 20% pre-strain applied at 800°C, with a strain rate of 0.1 s<sup>-1</sup>.

Table 5.13: LCEPSi values implemented in the numerical simulations.

Pre-strain (%)	700°C				800°C			
	LCEPS4		LCEPS5		LCEPS4		LCEPS5	
	0.1s <sup>-1</sup>	1s <sup>-1</sup>						
0	1	1	0	0	1	1	0	0
5	0.94	0.86	-22	-38	0.98	0.89	-18	-29
10	0.81	0.75	-29	-35	0.84	0.78	-28	-23
15	0.77	-	-37	-	0.79	-	-36	-
20	-	-	-	-	0.74	-	-42	-

### 5.5.2 Hot Nakajima tests simulations

The hot Nakajima tests describing the influence of the microstructure on the FLCs are simulated in order to confirm the experimental results. MAT\_244 does not allow the phase transformation in the condition of constant temperature, due to the implemented phase transformation kinetic law. For this reason, the percentage of austenite and bainite are inserted using the flags AUST and BAIN, which allows the implementation of a wanted percentage of the different phases.

Table 5.14 reports the values of AUST and BAIN used in the different simulations.

Table 5.14: Flags AUST and BAIN settings.

Test conditions	AUST	BAIN
100% austenite	1	0
50% austenite – 50% bainite	0.5	0.5
100% bainite	0	1

There is no damage criterion implemented in this set of simulations, so the FLC point is obtained comparing the experimental stroke at fracture and the calculated stroke. Figure 5.45 shows the comparison between the experimental and the numerical FLCs [102-103].

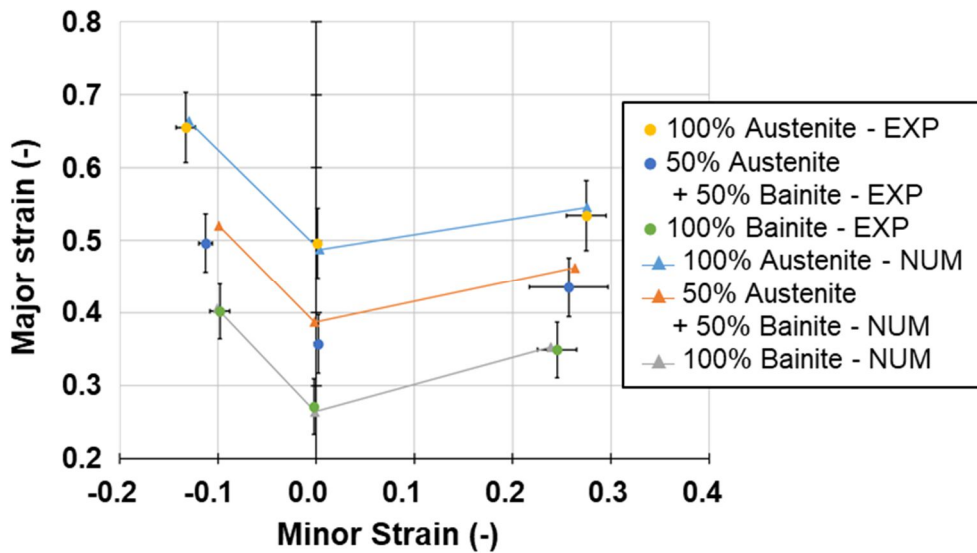


Figure 5.45: FLCs obtained at 600°C for different microstructure compared with the numerical simulations results.

The fitting for the cases in pure phase, both austenite and bainite, is good, while the fitting for the mixed phase FLC is less good. This is because the LS-Dyna material model 244 cannot simulate the phase transformation in condition of constant temperature, so the software cannot follow the evolution of the microstructure during the deformation of the specimen. Figure 5.46 shows the comparison between the measured reduction of thickness and the calculated reduction of thickness. It can be seen that the percentage of reduction is lower in

the case of pure bainite with respect to pure austenite. This means that the material can be stretched less during deformation, which may cause unwanted cracks in the most stretched areas of the blank.

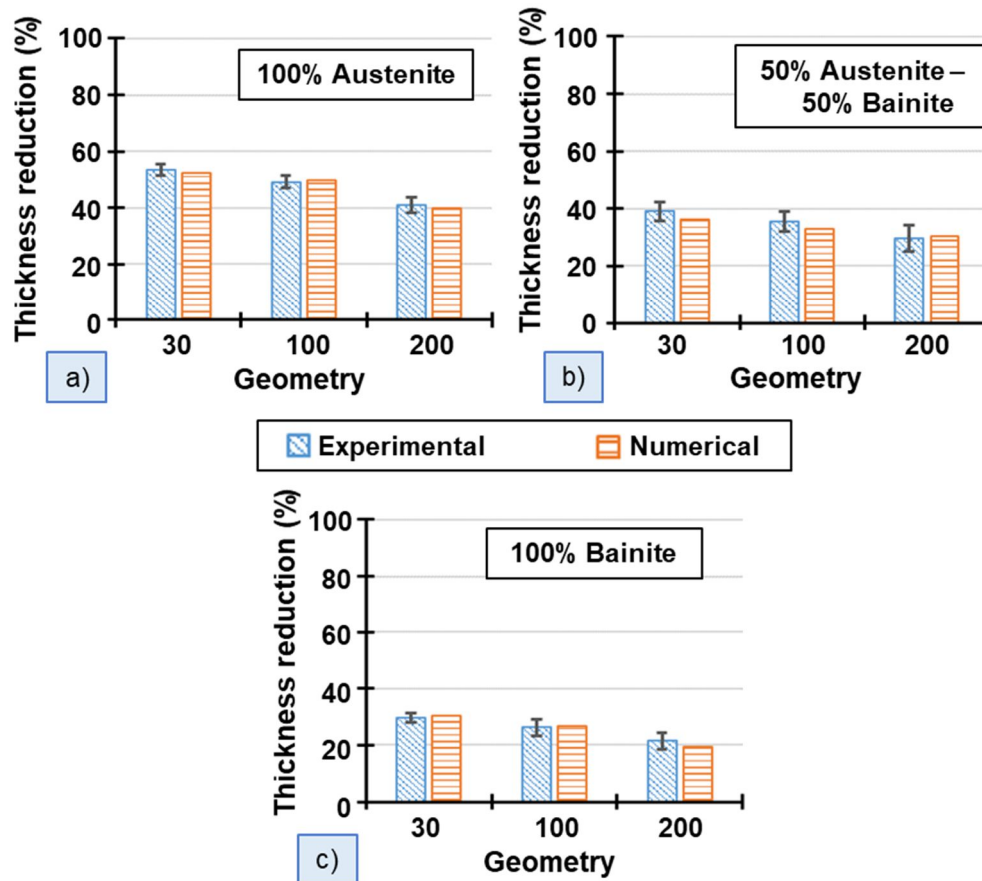


Figure 5.46: Experimental and numerical thickness reduction: a) 100% A; b) 50%A-50%B, c) 100% B.

Figure 5.47 shows a comparison between the experimental Aramis™ frame and the corresponding simulation frame of the 100mm geometry of the 100% bainite case. It can be seen that the distance of the fracture from the centre of the specimen is almost the same in the two cases, underlying the good accuracy of the numerical model. The numerical simulation cannot predict the localization in one specific region because there are no preferential areas with a concentration of defects, which causes the concentration of the strain and subsequent fracture.

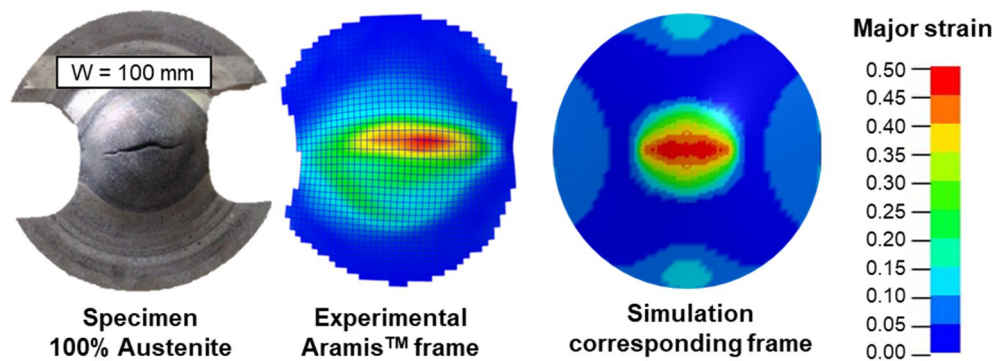


Figure 5.47: Experimental and numerical normalized major strain, 100% bainite case.

In order to highlight the difference between the material model 244, which allows phase transformations and the setting of a specific percentage of the different phases, and a material model which does not have these features, the material model *106\_ELASTIC\_VISCOPLASTIC\_THERMAL* was selected to run simulations and compare the results. The reference values for this comparison are the FLC points relative to the 200 mm geometry tested at 600°C with the thermal cycle shown in Figure 3.16 (a), both the average with the relative error bands and one of the repeatabilities. These points were compared with the numerical simulation results relative to the simulation run with material model 106 and material model 244, considering a bainite percentage of 20% and an austenite percentage of 80%. As reference, the 100% austenite and 50-50% austenite-bainite numerical simulations results (200 mm geometry, Figure 5.45) were also added. The results shown in Figure 5.48, highlight that the material model 106 is not able to validate the FLC point since it is far over the scatter band of the average point. On the other hand, the results of the simulation run with material model 244 is on the edge of the scatter bands, but close to the experimental point. This confirms that material model 244 is of crucial importance when a phase transformation is involved. Moreover, the simulation results confirm that a certain percentage, close to the 20% as estimated, of bainite is present in the specimen at the moment of fracture.

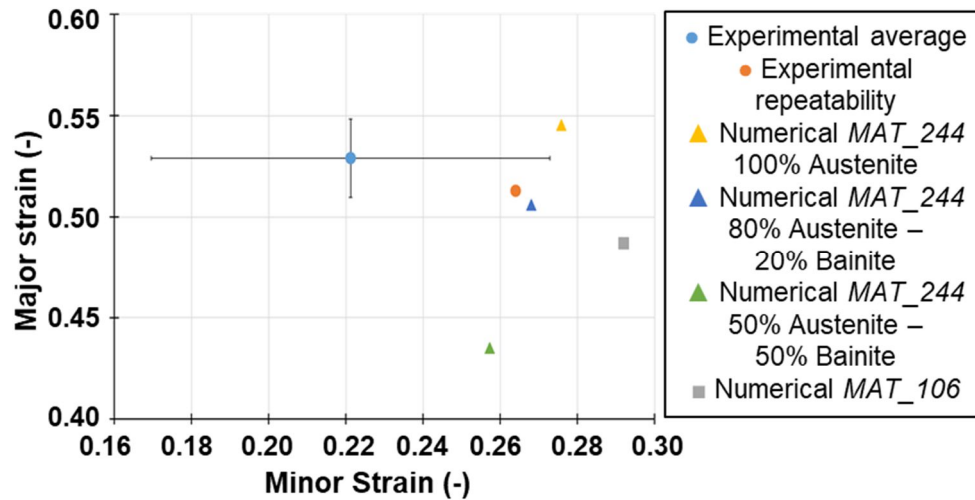


Figure 5.48: Comparison between simulations with MAT\_244 and MAT\_106.

## 5.6 GISSMO damage criterion

The numerical simulations regarding the GISSMO damage criterion were divided into three different sections: the first set of numerical simulations did not foresee failure and was meant to obtain the values of stress triaxiality, the second set of simulations was meant to reproduce the experimental tensile and Nakajima tests, and calibrate the GISSMO damage criterion, added thanks to the MAT\_000\_ADD\_EROSION card, and the third set of simulations was meant to validate such model, reproducing the Nakajima tests of the 100 mm geometry.

### 5.6.1 Determination of the stress triaxiality

The triaxiality values for all the tensile specimens, namely the smooth, notched and shear specimens, and for the 200 mm Nakajima specimen were obtained through numerical simulation without the implementation of the fracture criterion. Figure 5.49 reports the plots triaxiality vs effective plastic strain for the 6 geometries tested at the two selected testing temperatures, namely 700°C and 800°C, before necking.

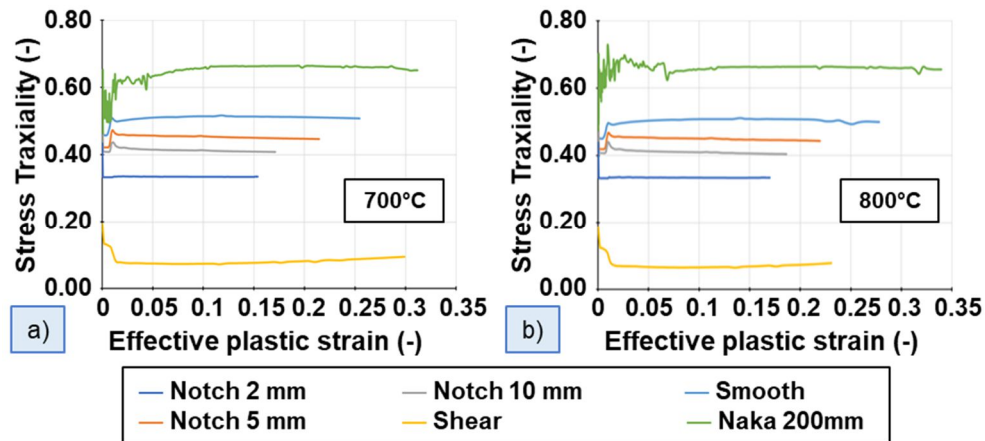


Figure 5.49: Stress triaxiality results from the numerical simulations.

The evolution of the triaxiality as a function of the plastic strain proves that there is no temperature effect on the stress triaxiality before necking occurrence. This means that the sample geometry plays a major role in determining the stress state. Therefore, the average values of the stress triaxiality were taken before necking, excluding the first portion of the curves. The same values were considered regardless of the testing temperature and sample orientation. Table 5.15 reports the mean values of the stress triaxiality.

Table 5.15: Mean values of stress triaxiality.

Specimen	Mean Stress Triaxiality (-)	Std. Dev. (-)
<b>Nakajima 200 mm</b>	0.664	0.008
<b>Notch 2 mm</b>	0.510	0.003
<b>Notch 5 mm</b>	0.452	0.003
<b>Notch 10 mm</b>	0.411	0.003
<b>Smooth</b>	0.333	0.003
<b>Shear</b>	0.084	0.004

The GISSMO model requires the coupling of the stress triaxiality with the values of the strain at fracture and of the instability strain. Figure 5.50 reports the plots of the strain values vs. the stress triaxiality. These curves were then implemented in the damage criterion in the numerical simulations. Tables 5.16 and 5.17 report the values of the strain at fracture and the instability strain obtained through experimental tests.

Table 5.16: Experimental fracture and instability strain values, tests at 700°C.

Specimen	$\epsilon_f$ (-)	Std. dev. (-)	$\epsilon_{inst}$ (-)	Std. dev. (-)
<b>Nakajima 200 mm</b>	0.436	0.06	0.318	0.07
<b>Notch 2 mm</b>	0.398	0.03	0.253	0.03
<b>Notch 5 mm</b>	0.334	0.02	0.205	0.02
<b>Notch 10 mm</b>	0.362	0.03	0.177	0.03
<b>Smooth</b>	0.527	0.02	0.153	0.02
<b>Shear</b>	0.744	0.04	-	-

Table 5.17: Experimental fracture and instability strain values, tests at 800°C.

Specimen	$\epsilon_f$ (-)	Std. dev. (-)	$\epsilon_{inst}$ (-)	Std. dev. (-)
<b>Nakajima 200 mm</b>	0.465	0.07	0.336	0.07
<b>Notch 2 mm</b>	0.416	0.04	0.276	0.04
<b>Notch 5 mm</b>	0.349	0.03	0.214	0.03
<b>Notch 10 mm</b>	0.371	0.03	0.185	0.03
<b>Smooth</b>	0.558	0.02	0.169	0.02
<b>Shear</b>	0.851	0.05	-	-

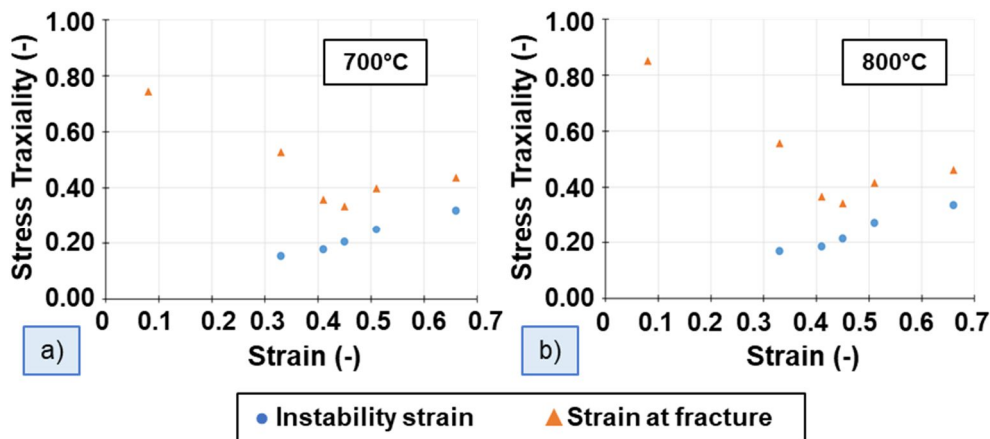


Figure 5.50: Curves fracture and instability strain vs triaxiality for the tests performed at (a) 700°C, (b) 800°C.

### 5.6.2 Damage model calibration

The comparison between the fracture characteristics predicted by the numerical models of the tests calibrated on the basis of the above described procedure and the experimental ones are shown in Figure 5.51 for the testing temperature of 700°C, and in Figure 5.52 for the testing temperature of 800°C, which are relevant to tests carried out at 700°C and 800°C. In the case of tensile

and shear tests, the comparison was carried out considering the shape of the fracture and the comparison between the experimental and the numerical values strain at fracture. In the case of Nakajima tests conducted on equi-biaxial specimens, the comparison was about the shape of the fracture and the comparison between the experimental and the numerical values of the major strain at fracture. Tables 5.18 and 5.19 reported reports the comparison between the experimental and the calculated values of the strain at fracture and the major strain at fracture for the testing temperature of 700°C and 800°C respectively.

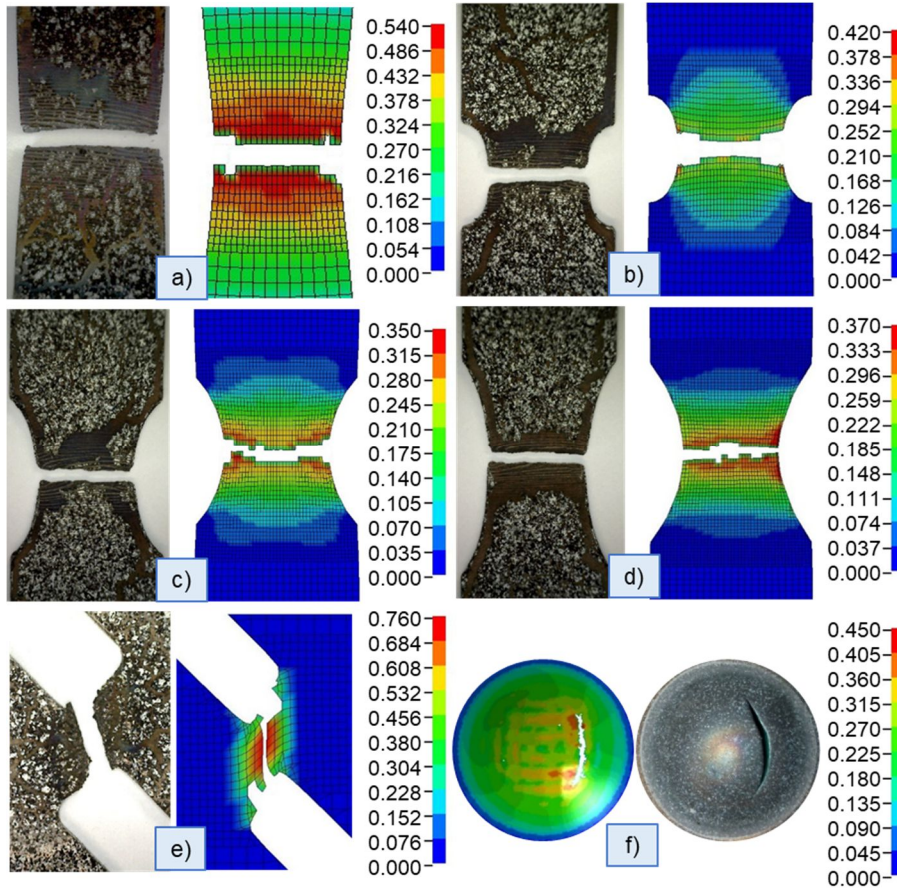


Figure 5.51: Comparison between effective strain of real specimens and simulation; temperature = 700°C, a) smooth, b) notch 2 mm, c) notch 5 mm, d) notch 10 mm, e) shear, f) Nakajima 200mm.

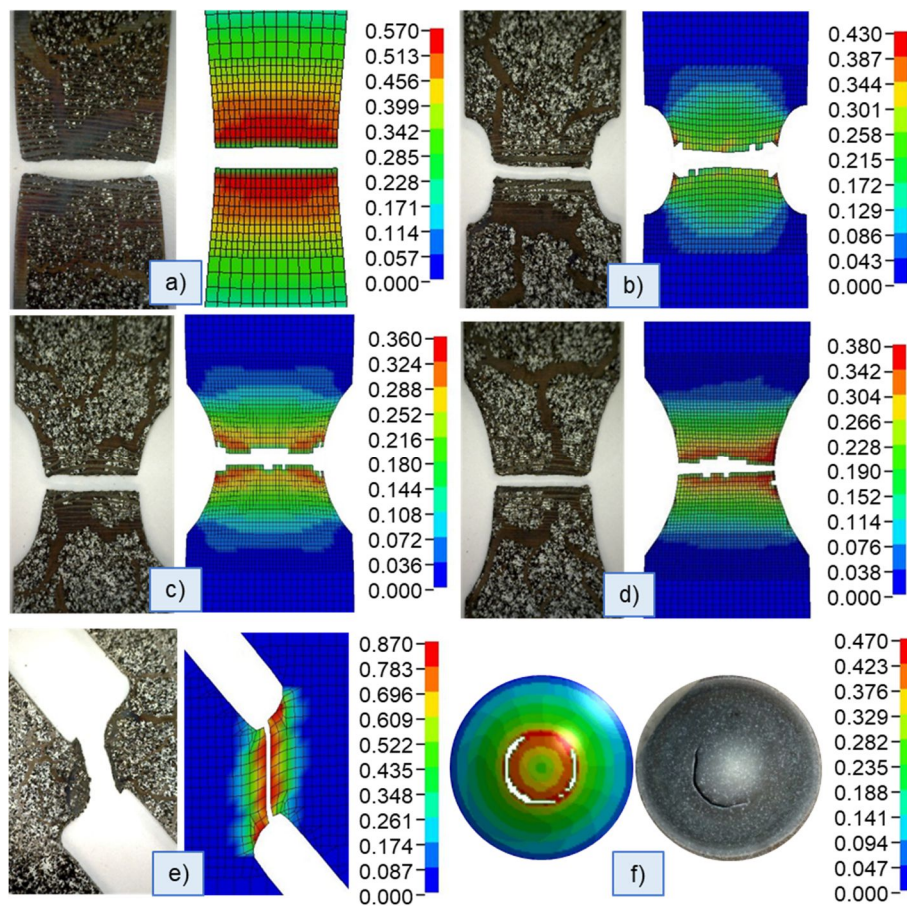


Figure 5.52: Comparison between effective strain of real specimens and simulation; temperature = 800°C, a) smooth, b) notch 2 mm, c) notch 5 mm, d) notch 10 mm, e) shear, f) Nakajima 200mm.

Table 5.18: Comparison between experimental and calculated strain at fracture  $T = 700^{\circ}\text{C}$ .

Specimen	Experimental		Numerical
	$\epsilon_f$ (-)	Std. dev. (-)	$\epsilon_f$ (-)
<b>Nakajima 200 mm</b>	0.436	0.06	0.417
<b>Notch 2 mm</b>	0.398	0.03	0.407
<b>Notch 5 mm</b>	0.334	0.02	0.341
<b>Notch 10 mm</b>	0.362	0.03	0.369
<b>Smooth</b>	0.527	0.02	0.519
<b>Shear</b>	0.744	0.04	0.752

Table 5.19: Comparison between experimental and calculated strain at fracture  
 $T = 800^{\circ}\text{C}$ .

Specimen	Experimental		Numerical
	$\epsilon_f$ (-)	Std. dev. (-)	$\epsilon_f$ (-)
<b>Nakajima 200 mm</b>	0.465	0.07	0.438
<b>Notch 2 mm</b>	0.416	0.04	0.428
<b>Notch 5 mm</b>	0.349	0.03	0.357
<b>Notch 10 mm</b>	0.371	0.03	0.364
<b>Smooth</b>	0.558	0.02	0.564
<b>Shear</b>	0.851	0.05	0.874

The comparison between the numerical and experimental shapes of the fractures shows a good agreement both in the shape and in the position, and the values of the calculated strain at fracture stands within the limits represented by the experimental error. Figures 5.53 and 5.54 reports the comparison between the experimental and the numerical stress-strain curves, which shows good fitting for both the temperatures tested.

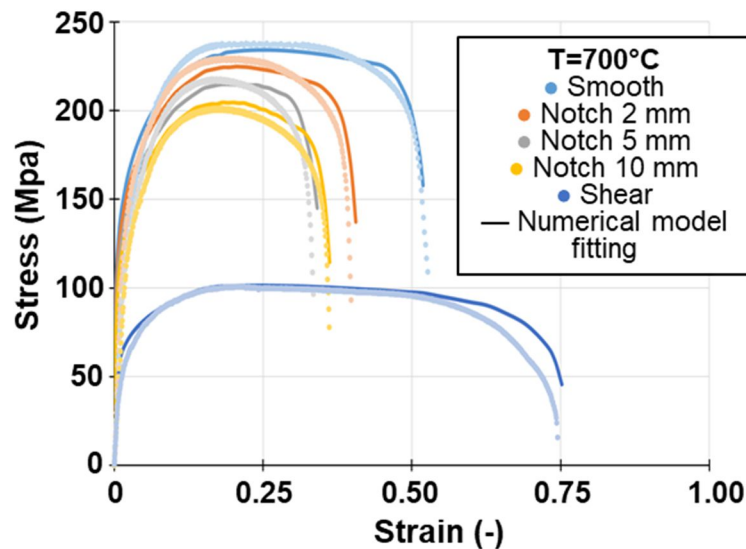


Figure 5.53: Comparison between experimental and calculated flow curve,  $T=700^{\circ}\text{C}$ .

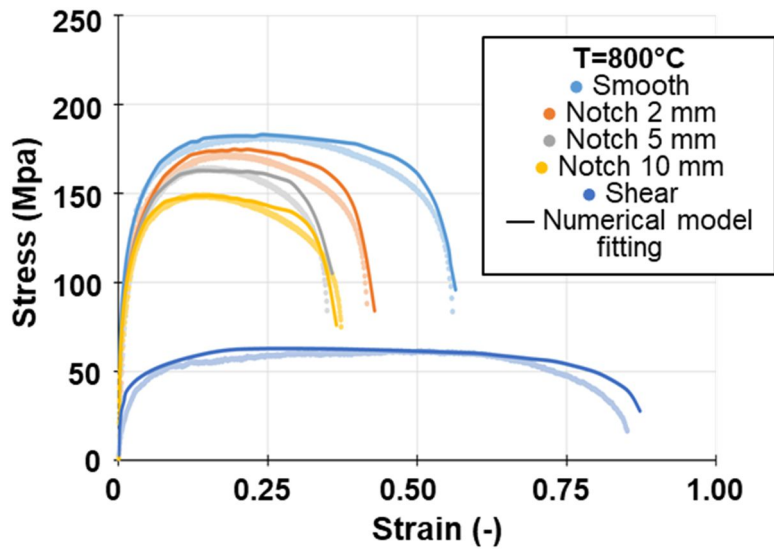


Figure 5.54: Comparison between experimental and calculated flow curve,  $T=800^{\circ}\text{C}$ .

### 5.6.3 Damage model validation

After the calibration of the GISSMO, the numerical simulation was applied to model the fracture of 100 mm Nakajima specimens tested at  $700^{\circ}\text{C}$  and  $800^{\circ}\text{C}$  deformed with a strain rate of  $1\text{ s}^{-1}$ . Figure 5.55 shows the comparison between the numerical and experimental shapes of the fractures. It was found that the position of the fracture can be correctly simulated by the model. In Table 5.20 the comparison between the experimental and the calculated major strain at fracture is reported, and it shows that the calculated strains stand in the error bands of the experimental strains.

Table 5.20: Comparison between experimental and calculated major strain at fracture, Nakajima 100 mm.

Temperature ( $^{\circ}\text{C}$ )	Experimental		Numerical
	$\epsilon_f$ (-)	Std. dev. (-)	$\epsilon_f$ (-)
700	0.405	0.04	0.389
800	0.429	0.05	0.415

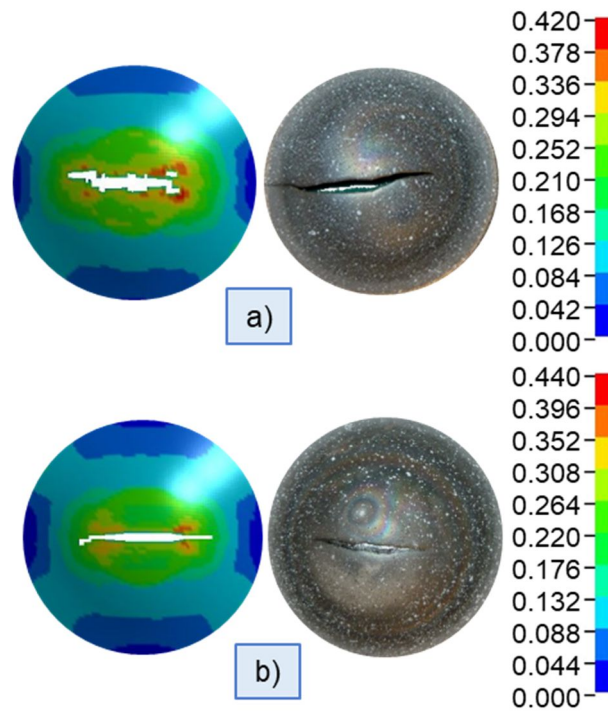


*Figure 5.55: Comparison between major strain of real Nakajima 100mm specimen and simulation; a) temperature = 700°C, b) temperature = 800°C.*

## **CHAPTER 6**

### **Conclusions**



This work is part of the framework of the research that regards the hot stamping process, which, nowadays, is the focus in the whole automotive sector. The cooperation with Ford GMBH helped the link between the experimental and the industrial problems, and this helped the understanding of the real process.

The work is divided into different research fields, all focused on the material 22MnB5, ArcelorMittal™ with the name of Usibor 1500P®, with AluSi® coating.

**Phase transformation kinetics:** the first field of research regarded the study of the kinetic of the different phase transformations that regards the material since this is the base to draw all the thermal cycles involved in this work. The CCT diagram obtained confirmed the first presence of bainite if a cooling rate of 27°C/s is followed and the transformation of austenite in bainite is complete if the blank is cooled to room temperature with a cooling rate of 10°C/s. The phenomenon of the CCT left-shift described in literature is confirmed, and a new and complete set of data is presented. Using LS-DYNA code, the parameters LCEPS4 and LCEPS5 of material model 244 UHS\_STEEL are calibrated, in order to reproduce the CCT left-shift also in the numerical model. This particular behaviour is of fundamental importance when the dies, and their cooling systems, are designed, since a more severe amount of heat has to be removed from the blank.

**Rheology:** the study of the rheology of the material has fundamental importance because the data are required in the numerical simulations. First, the thermal cycle applied in the real hot stamping process was used to perform the first, preliminary studies. It was demonstrated that the rise of the curves is due to the phase transformation of austenite into bainite, which rises the resistance of the material to the deformation. For this reason, that thermal cycle was not suitable for the study of the austenite rheology, since the tested phase was a mixture and not the pure phase, and the cooling rate was chosen equal to 80°C/s instead of 35°C/s. The data regarding the rheology of austenite, pearlite + ferrite, were all obtained through hot tensile tests in the MTS 322, but the bainite and the martensite phases, being the tougher phases tested, required an external heating system to create dog-bone specimens completely in pure bainite or martensite phase. Nevertheless, all the phases were tested through tensile tests, and this covers a lack in literature regarding the bainite and martensite phases, which were only tested via compression tests. Along with the experimental data, a modified

---

Johnson-Cook model was built in order to increase the goodness of the original model, which fails to reproduce the curves at high temperature. The new model halved the error between the experimental and the calculated flow curve, and this means that a set of more precise data can be implemented in the numerical simulations.

**Formability:** the influence on the FLC of the temperature and of the microstructural composition was studied. As expected, the obtained results showed that the temperature influenced both the major and minor strains: the higher the testing temperature the more formable the material, especially in terms of minor strain. Furthermore, the strain path changed with temperature, giving the plane strain state with different geometries, on the basis of the testing temperature. Also in this case, the thermal cycle applied was the same used in the real process and, considering the duration of the test and the testing temperature, it can be estimated that at the moment of fracture a percentage of about the 20% of bainite was present in the specimen, resulting in a FLC of a mixture of austenite and bainite. For this reason, the influence of the microstructure on the FLCs was studied considering three different mixtures: 100% austenite, 50% austenite + 50% bainite and 100% bainite. The formability when the specimen is in pure austenite phase is the highest among the three conditions tested, and this is in agreement with the literature. The formability when the specimen is in pure bainite phase is the lowest, in particular the major strain drops of about the 40% and the minor strain drops of about the 30% in respect with the pure austenite case. The case representing the 50% Austenite – 50% Bainite does not stand in the middle between the other two curves, because, when the fracture occurs, the phase mixture in the specimen is not exactly 50-50%. This is due to the fact that the microstructural evolution continues during the deformation of the piece. LS-DYNA code was used to reproduce the Nakajima tests regarding the influence of the microstructure on the final FLC. The fitting between the experimental data and the numerical data is good for the two cases in which the specimen is in pure phase but, since the material model 244 cannot simulate the phase transformation in isothermal condition, it cannot follow the evolution of the microstructure during the deformation, leading to a less refined fitting.

**GISSMO damage criterion:** the calibration of the GISSMO damage criterion started from the experimental tensile and Nakajima tests at 700°C and 800°C with a strain rate of  $1\text{s}^{-1}$  of a series of specimens in order to reproduce a

wide range of triaxiality conditions. The data of strain at fracture and instability strain were then implemented in LS-DYNA code using MAT\_ADD\_EROSION. After the calibration, where very good agreement between the experimental tests and the correspondent simulation was found, a series of simulations meant to validate the model were run. These series of simulations regarded the Nakajima test of the 100 mm geometry, tested at the same strain rate and temperature of the other specimens. The results show a very good agreement between the experimental test and the numerical model, both in terms of position and shape of fracture, and in terms of values of strain at fracture, since the calculated strain at fracture values stand in the error bands of the experimental values of the strain of fracture

All the obtained results give a wide and detailed description of the behaviour of 22MnB5 in the usual conditions of the hot stamping process. The experimental tests were always coupled with the numerical simulations, which are a necessity to predict the behaviour of the material or to calibrate the design of the dies. The data presented in this thesis can be applied in the simulations of a wide range of processes regarding 22MnB5 steel.



## REFERENCES

- [1] Unfccc, 1998, Kyoto Protocol To the United Nations Framework Kyoto Protocol To the United Nations Framework, Review of European Community and International Environmental Law, 7:214–217, DOI:10.1111/1467-9388.00150.
- [2] SMMT Driving the Motor Industry, 95 CO<sub>2</sub> g/km target.
- [3] K. Bachman, Hot-stamped parts in 2019 vehicles and the die steel, furnace technologies enabling it, Stamping Journal July/ August 2018, July 26, 2018.
- [4] Patent GB1490535, 1977. Manufacturing a hardened steel article, Norrbottens Jaernverk AB.
- [5] Berglund, G., 2008. The history of hardening of boron steel in northern Sweden. In: 1st International Conference on Hot Sheet Metal Forming of High-Performance Steel, Kassel, Germany, pp. 175–177.
- [6] Aspacher, J., 2008. Forming hardening concepts. In: 1st International Conference on Hot Sheet Metal Forming of High-Performance Steel, Kassel, Germany, pp.77–81.
- [7] G. Venturato, M. F. Novella, S. Bruschi, A. Ghiotti, R. Shivpuri, Effects of phase transformation in hot stamping of 22MnB5 high strength steel, Procedia Engineering, Volume 183, 2017, Pages 316-321.
- [8] N. N., 2009, Stahl-Informations-Zentrum. Stahl im Automobil, Leicht und sicher. [www.stahl-info.de](http://www.stahl-info.de).
- [9] Merklein, M., Lechler, J., 2008. Determination of material and process characteristics for hot stamping processes of quenchable ultra high strength steels with respect to a FE-based process design, SAE World Congress: Innovations in Steel and Applications of Advanced High Strength Steels for Automobile Structures, Paper No. 2008–0853.

- [10] D. Lorenz, K. Roll, Simulation of hot stamping and quenching of boron alloyed steel, in: Presented at Seventh Int. ESAFORM Conf. on Mat. Forming, Trondheim, Norway, 2004.
- [11] M. Geiger, M. Merklein, C. Hoff, Basic investigation on the hot stamping steel 22MnB5, in: Proceedings of the Sheet Metal 2005 Conf., 2005, pp. 795–802.
- [12] M. Suehiro, K. Kusumi, T. Miyakoshi, J. Maki, M. Ohogami, Properties of aluminium-coated steels for hot-forming, Nippon Steel Technical Report No. 88, July 2003.
- [13] J. Wilsius, P. Hein, and R. Kefferstein, Status and future trends of hot stamping of USIBOR 1500 P, presented at Erlangen Workshop 2006.
- [14] K. Mori, P.F. Bariani, B.-A. Behrens, A. Brosius, S. Bruschi, T. Maeno, M. Merklein, J. Yanagimoto, Hot stamping of ultra-high strength steel parts, CIRP Annals Volume 66, Issue 2, 2017, Pages 755-777.
- [15] M. Naderi, 2007. Hot stamping of ultra high strength steels. Doctoral Thesis, RWTH Aachen.
- [16] G. Aranda, L., Chastel, Y., Fernandez Pascual, J., Dal Negro, T., Experiments and simulation of hot stamping of quenchable steels. Advanced Technology of Plasticity 2, 1135–1140.
- [17] <https://automotive.arcelormittal.com/>
- [18] A. Turetta, Investigation of thermal, mechanical and microstructural properties of quenchable high strength steels in hot stamping operations, Doctoral Thesis, 2008.
- [19] Borsetto, F., Ghiotti, A., Bruschi, S., 2009. Investigation of the high strength steel Al–Si coating during hot stamping operations. Key Engineering Materials 410–411, 289–296.
- [20] H. Karbasian, A.E. Tekkaya, A review on hot stamping, Journal of Materials Processing Technology 210 (2010) 2103–2118.

- [21] H. Järvinen, M. Isakov, T. Nyysönen, M. Järvenpää, P. Peura, The effect of initial microstructure on the final properties of press hardened 22MnB5 steels, *Materials Science & Engineering A* 676(2016)109–120.
- [22] N. Li, J. Lin, D.S. Balint, T.A. Dean, Experimental characterisation of the effects of thermal conditions on austenite formation for hot stamping of boron steel, *Journal of Materials Processing Technology* 231 (2016) 254–264.
- [23] A. Grajcar, M. Opiela Influence of plastic deformation on CCT-diagrams of low carbon and medium carbon TRIP steels, *J. Achiev. Mater.* 29 (2008) 71–78.
- [24] M. Naderi, A. Saeed-Akbari, W. Bleck, The effects of non-isothermal deformation on martensitic transformation in 22MnB5 steel, *Mater. Sci. Eng. A* 487 (2008) 445–455.
- [25] M. Naderi, W. Bleck, K. Steinhoff, Hot Stamping of Ultra High Strength Steels, Institute of ferrous metallurgy, Aachen, PhD Thesis, 2007.
- [26] S.V. Sajadifar, M. Ketabchi, M.R. Nourani, Hot Deformation Characteristics of 34CrMo4 Steel *J. Iron Steel Res. Int.* 17 (12) (2010) 65–69.
- [27] H.J. Jun, J.S. Kanga, D.H. Seo, K.B. Kang, C.G. Park, *Mater. Sci. Eng. A* 422 (2006) 157–162.
- [28] C.H. Lee, H.K.D.H. Bhadeshia, H.C. Lee, *Mater. Sci. Eng. A* 360 (2003) 249–257.
- [29] W. Bing-xin, J. Ying-tian, X. Xu-dong, L. Xiang-hua, W. Guo-dongz, *J. Iron Steel Res. Int.* 14 (2007) 69–73.
- [30] R.H. Larn, J.R. Yang, *Mater. Sci. Eng. A* 278 (2000) 278–291.
- [31] X.J. Jin, N. Min, K.Y. Zheng, T.Y. Hsu, X. Zuyao, *Mater. Sci. Eng. A* 438–440 (2006) 170–172.
- [32] A. Barcellona, D. Palmeri, Effect of Plastic Hot Deformation on the Hardness and Continuous Cooling Transformations of 22MnB5 Microalloyed Boron Steel, *Metallurgical and Materials Transactions A*, May 2009, Volume 40, Issue 5, pp 1160–1174.

- [33] M. Nikraves, M. Naderi, G.H. Akbari, Influence of hot plastic deformation and cooling rate on martensite and bainite start temperatures in 22MnB5 steel, *Materials Science and Engineering A* 540 (2012) 24– 29.
- [34] M. Merklein, J. Lechler, M. Geiger, Characterisation of the Flow Properties of the Quenchenable Ultra High Strength Steel 22MnB5, *CIRP Annals Volume* 55, Issue 1, 2006, Pages 229-232.
- [35] M. Merklein, M. Wieland, M. Lechner, S. Bruschi, A. Ghiotti, Hot stamping of boron steel sheets with tailored properties: A review, *Journal of Materials Processing Technology* 228 (2016) 11–24.
- [36] M. Merklein, J. Lecher, V. Gödel, S. Bruschi, A. Ghiotti, A. Turetta, Mechanical properties and plastic anisotropy of the quenchenable high strength steel 22MnB5 at elevated temperatures, *Key Engineering Materials* Vol. 344 (2007) pp 79-86.
- [37] M. Merklein, J. Lechler, Investigation of the thermo-mechanical properties of hot stamping steels, *Journal of Materials Processing Technology* 177 (2006) 452–455.
- [38] N. Li, C. Sun, N. Guo, M. Mohamed, J. Lin, T. Matsumoto, C. Liu, Experimental investigation of boron steel at hot stamping conditions, *Journal of Materials Processing Technology* 228 (2016) 2–10.
- [39] M. Abspoel, B. M. Neelis, P. van Liempt, Constitutive behaviour under hot stamping conditions, *Journal of Materials Processing Technology* 228 (2016) 34–42.
- [40] H. Li, L. He, G. Zhao, L. Zhang, Constitutive relationships of hot stamping boron steel B1500HS based on the modified Arrhenius and Johnson–Cook model, *Materials Science & Engineering A* 580 (2013) 330–348.
- [41] M. F. Novella, G. Venturato, S. Bruschi, A. Ghiotti, Influence of phase transformation on 22MnB5 mechanical behaviour in hot stamping, *CHS2 2017 Proceedings*, PP 423-431, Editors M. Oldenburg et al.

- [42] L. Zhu, Z. Gu, H. Xu, Y. Lu, J. Chao, Modeling of microstructure evolution in 22MnB5 steel during Hot Stamping, *Journal of iron and steel research, International*, 21 (2), 197-201, 2014.
- [43] D. Pellegrini, Study on thermal and rheological parameters of high strength steels in hot forming conditions, PhD Thesis, University of Padua, 2008.
- [44] Z. Marciniak, K. Kuczynski, Limit strains in the process of stretch-forming sheet metal, *Int. Journal of Mech. Science* 9, 609-620.
- [45] K. Nakazima, T. Kikuma, K. Asaku, Study on the formability of steel sheet, *Yawata Technical Report* 264 (1968).
- [46] Standard ISO 12004-2-2008.
- [47] M. Geiger, M. Merklein, Determination of Forming Limit Diagrams—A New Analysis Method for Characterization of Materials' Formability, *Annals of the CIRP* 52(1) (2003), pp. 213–216.
- [48] <http://www.gom.com/metrology-systems/aramis.html>.
- [49] M. Merklein, A. Kuppert, M. Geiger, Time dependent determination of forming limit diagrams, *CIRP Annals – Manufacturing Technology* 59 (2010) 295–298.
- [50] B.L. Ma, X.D. Wu, X.J. Li, M. Wan, Z.Y. Cai, Investigation on the hot formability of TA15 titanium alloy sheet, *Materials and Design* 94 (2016) 9–16.
- [51] A. Turetta, S. Bruschi, A. Ghiotti, Investigation of 22MnB5 formability in hot stamping operations, *Journal of Materials Processing Technology* 177 (2006) 396–400.
- [52] J. Cui, G. Sun, J. Xu, X. Huang, G. Li, A method to evaluate the formability of high-strength steel in hot stamping, *Materials and Design* 77 (2015) 95–109.
- [53] P.F. Bariani, S. Bruschi, A. Ghiotti, A. Turetta, Testing formability in the hot stamping of HSS, *CIRP Annals – Manufacturing Technology* 57 (2008) 265–268.

- [54] K.C. Cho, D.J. Mun, J.Y. Kim, J.K. Park, J.A. Lee, Y.M. Koo, Effect of Boron Precipitation Behavior on the Hot Ductility of Boron Containing Steel, *Metallurgical and materials transactions A*, 41A, 2010 – 1421-1428.
- [55] K.C. Cho, D.J. Mun, Y.M. Koo, J.S. Lee, Effect of niobium and titanium addition on the hot ductility of boron containing steel, *Materials Science and Engineering A* 528 (2011) 3556–3560.
- [56] H. Güler, R. Ertan, R. Özcan, Characteristics of 30MnB5 boron steel at elevated temperatures, *Materials Science and Engineering A*, 578 (2013) 417–421.
- [57] H. Güler, R. Ertan, R. Özcan, Investigation of the hot ductility of a high-strength boron steel, *Materials Science Engineering A* 608 (2014) 90–94.
- [58] L.G.Aranda, P. Ravier, and Y. Chastel, Hot Stamping of Quenchable Steels: Material Data and process Simulations, *IDDRG 2003 Conf., Proc.* (2003), pp. 166-164, 2003.
- [59] P. Akerstrom and M. Oldenburg, Austenite Decomposition During Press hardening of a Boron Steel – Computer Simulation and Test, *Journal of Material processing technology*, 174 (2006), pp399-406..
- [60] D.Lorenz and K. Roll, Simulation of Hot Stamping and Quenching of Boron alloyed Steel, 7th Int. ESAFORM Conf. on Mat. Forming, Trondheim, Norway, 2004.
- [61] H. S. H. Kim, S. Kang, S. Park, Thermal-Mechanical coupled simulation of the forming of hot press formed part, presented at *Proceedings of the IDDRG 2006 Conference*.
- [62] P.Akerstrom, G. Bergman, and M. Oldenburg, Numerical implementation of a constitutive model for simulation of hot stamping, *Modelling and Simulation, Materials Science and Engineering*, vol. 15/2, pp. 105-119, 2007.
- [63] L.G.Aranda, P. Ravier, and Y. Chastel, Experimental, material data and numerical model for hot stamping of quenchable steels, 6th ESAFORM Conference on Material Forming, 2003.

- [64] F. Barlat, H.-H. Bok, J. W. Choi, D. W. Suh, M.-G. Lee, Thermo-mechanical-metallurgical modeling for hot-press forming in consideration of the prior austenite deformation effect, *International Journal of Plasticity* 58 (2014) 154–183.
- [65] P. Akerstrom, Modelling and simulation of hot stamping, Doctoral Thesis, 2006.
- [66] T. Olsson, An LS-DYNA Material Model for Simulations of Hot Stamping Processes of Ultra High Strength Steels, ERAB, April 2009.
- [67] S. Sjöström, The calculation of quench stresses in steel, Doctoral Thesis, 1982.
- [68] W. Müschenborn and H.M. Sonne, *Archiv Eisenhüttenwesen*, 46/9:597-602 (1975).
- [69] H.J. Kleemola and M.T. Pelkkikangas, Effect of pre-deformation and strain path on the forming limits of steel copper and brass, *Sheet Metal Ind.*, 63:591-599 (1977).
- [70] Y. Bergström and S. Ölund, *Mater. Sci. Eng.*, 56:47-61 (1982).
- [71] A. Graf and W.F. Hosford, Effect of Changing Strain Paths on Forming Limit Diagrams of Al 2008-T4, *Metall. Trans. A*, 24:2497-2501 (1993).
- [72] H. Yao and J. Cao, Prediction of forming limit curves using an anisotropic yield function with prestrain induced backstress, *Int. J. Plasticity*, 18/8:1013-1038 (2002).
- [73] T.B. Stoughton and X. Zhu, Review of theoretical models of the strain-based FLD and their relevance to the stress-based FLD, *Int. J. Plasticity*, 20/8-9:1463-1486 (2004).
- [74] P. Hora and L. Tong, Numerical Prediction of FLC Using the Enhanced Modified Maximum Force Criterion, in *Proceedings of FLC-Zurich 06*, edited by P. Hora, Zurich, 2006, pp. 31-36.

- [75] Wolfram Volk, Jounghsik Suh, Prediction of formability for non-linear deformation history using generalized forming limit concept (GFLC), AIP Conference Proceedings 1567, 556 (2013);
- [76] Andrade F., Feucht M., A comparison of damage and failure models for the failure prediction of dualphase steel, 11th European LS\_DYNA Conference 2017.
- [77] Gurson A. L., Continuum theory of ductile rupture by void nucleation and growth: Part I- Yield criteria and flow rules for porous ductile media, Journal of Engineering Materials and Technology 99 (1), pp 2-15, 1977.
- [78] Tvergaard V., Influence of voids on shear band instabilities under plane strain conditions, International Journal of Fracture 157, pp 55-69, 1981.
- [79] Tvergaard V., Needleman A., Effects of nonlocal damage in porous plastic solids, International Journal of Solids and Structures 32, No 8/9, pp 1063-1077, 1995.
- [80] Cockroft M. G., Latham D. J., Ductility and workability of metals, Journal of the institute of Metals 96, pp 33-39, 1968.
- [81] Neukamm F., et al., On closing the constitutive gap between forming and crash simulation, 10<sup>th</sup> International Journal of Fracture, 200:127, 2016
- [82] Andrade F. X. C. et al., An incremental stress state dependent damage model for ductile fracture prediction, International Journal of Fracture, 200: 127, 2016.
- [83] F. Andrade, T. Erhart, A. Haufe, Modeling of anisotropic damage with \*MAT\_ADD\_GENERALIZED\_DAMAGE, DynaMore, October 13th, 2016.
- [84] Golling S. et al., A comparative study of different failure modeling strategies on a laboratory scale test component, 6th International Conference Hot Sheet Metal Forming of High-Performance Steel CHS2: June 4-7 2017, Atlanta, Georgia, USA : proceedings / [ed] Mats Oldenburg, Braham Prakash, Kurt Steinhoff, Warrendale, PA: Association for Iron & Steel Technology, AIST , 2017, p. 37-46.

- [85] Wang Q. L., Ghiotti A., Bruschi S., “Anisotropy influence on the failure of Ti6Al4V sheets deformed at room and elevated temperature”, AIP Conference Proceedings 1960, 160030 (2018)
- [86] Wang Q. L., Ghiotti A., Bruschi S., Mu Y., “Modelling of fracture occurrence in Ti6Al4V sheets at elevated temperature accounting for anisotropic behaviour”, International Journal of Mechanical Sciences 150 (2019) 471–483.
- [87] [https://www.salzgitter-flachstahl.de/fileadmin/mediadb/szfg/informationsmaterial/produktinformationen/warmgewalzte\\_produkte/eng/22mnb5.pdf](https://www.salzgitter-flachstahl.de/fileadmin/mediadb/szfg/informationsmaterial/produktinformationen/warmgewalzte_produkte/eng/22mnb5.pdf)
- [88] <https://www.totalmateria.com/page.aspx?ID=CheckArticle&site=kts&NM=214>
- [89] <https://automotive.arcelormittal.com/europe/products/EN>
- [90] Baumeister, Avallone, Baumeister. "6". Marks' Standard Handbook for Mechanical Engineers, 8th ed. McGraw Hill. pp. 17, 18.
- [91] Davis, J.R. (1996). ASM Handbook on Carbon and Alloy Steels. ASM International.
- [92] Q. Yin, B. Zillmann, S. Suttner, G. Gerstein, M. Biasutti, A. E. Tekkaya, M. F.-X. Wagner, M. Merklein, M. Schaper, T. Halle and A. Brosius, An experimental and numerical investigation of different shear test configurations for sheet metal characterization, Int. J. Solids. Struct. 51, 1066-1074 (2014).
- [93] LS-DYNA®, Keyword user’s manual, Volume II, LS-DYNA R10.0 10/16/17.
- [94] Whye-Teong Ang, Elastic crack problems, fracture mechanics, equations of elasticity and finite-part integrals, Hypersingular Integral Equations in Fracture Analysis 2013, Pages 1-24.
- [95] M.V Li, D.V Niebuhr, L.L Meekisho and D.G Atteridge, A Computational model for the prediction of steel hardenability, Metallurgical and materials transactions B, 29B, 661-672, 1998.

- [96] A.S. Oddy, J.M.J. McDill and L. Karlsson, Microstructural predictions including arbitrary thermal histories, re-austenitization and carbon segregation effects (1996).
- [97] Stander N , Roux WJ , Goel T , Eggleston T , Craig KJ . LS\_OPT version 4.1 user's manual. Livermore Software Technology Corporation; 2010
- [98] Stander N, Craig KJ. On the robustness of a simple domain reduction scheme for simulation-based optimization. Eng. Comput. 2002; 19:431–50.
- [99] <https://www.instron.us/en-us/our-company/library/glossary/u/upper-yield-strength>
- [100] G. R. Johnson, W. H. Cook, (1983), A constitutive model and data for metals subjected to large strains, high strain rates and high, Proceedings of the 7th International Symposium on Ballistics: 541–547, retrieved 2009-05-13.
- [101] G. Venturato, A. Ghiotti and S. Bruschi, Influence Of Temperature And Friction On The 22MnB5 Formability Under Hot Stamping Conditions, AIP Conference Proceedings 1960, 150014-1/6 (2018).
- [102] G. Venturato, S. Bruschi, A. Ghiotti, X. Chen, Numerical modelling of the 22MnB5 formability at high temperature, 18th International Conference on Sheet Metal, Procedia Manufacturing Volume 29, 2019, Pages 428-434.
- [103] G. Venturato, E. Simonetto, S. Bruschi, A. Ghiotti, X. Chen, Modelling of 22MnB5 hot stamping process coupling microstructural evolution, Numiform 2019, 13th International Conference on Numerical Methods in Industrial Forming Processes.